NORTHWESTERN UNIVERSITY

Modeling of Structural Plasticity and Synchronization in the Rodent Olfactory Bulb

A DISSERTATION

SUBMITTED TO THE GRADUATE SCHOOL
IN PARTIAL FULFILLMENT OF THE REQUIREMENTS

for the degree

DOCTOR OF PHILOSOPHY

Field of Applied Mathematics

By

John Hongyu Meng

EVANSTON, ILLINOIS

March 2020

ABSTRACT

Modeling of Structural Plasticity and Synchronization in the Rodent Olfactory Bulb

John Hongyu Meng

To survive, animals, including human beings, have developed an amazing ability to learn the constantly changing environment. Specifically, detecting specific odorants in a noisy, variable background is crucial for finding food and water, mating, and avoiding potential dangers. For this purpose, rodents have developed an olfactory system that is powerful enough to detect even small relative changes in a specific odor in a complex mixture by learning. Recent experiments have shown that part of this learning occurs in the olfactory bulb, which is the first region to receive odor information in the brain. As a result of the learning, the neuronal activity patterns that represent odors in the output of the bulb are more decorrelated than the corresponding patterns in the input.

In this dissertation, we try to understand the mechanism behind this discriminability from different aspects. The olfactory bulb is one of the few regions that

show prominent structural plasticity even when the animal has fully matured. The reciprocal dendro-dendritic connection between mitral and granule cells, which are the major principal cells and interneurons within the bulb, show around 20% rewiring at a 2-day interval. In addition, this modification of the network depends on the activity of mitral and granule cells. Chapter 1 of this dissertation discusses how a Hebbian-type rule of structural plasticity can explain the learning behavior observed in the olfactory bulb. We further argue that basic memory function is observed in the olfactory bulb and learning of similar but not dissimilar odor pairs leads to the loss of previously learned odors due to interference. We also discuss the impacts of varying the major parameters of the model.

The olfactory bulb is also a brain area that displays extensive rhythmic activity, particularly in the beta- (13 to 30 Hz) and gamma-band (30 to 100 Hz). It has also been observed in experiments that the power of gamma-oscillations increases more when a rodent tries to distinguish more similar odorants after learning. During the study of structural plasticity, we observed that as a result of the learning the network of the olfactory bulb model develops a subnetwork structure reflecting the learned odors. This observation makes us wonder under what condition the rhythms in subnetworks can be synchronized. In chapter 2, during the study of this question, we discover and explain an interesting counter-intuitive phenomenon, which

is how independent noise can synchronize population rhythms arising in interconnected subnetworks. We show that by including noise, a negative feedback control loop stabilizes synchronization between different rhythms. Further, the results on synchronization by noise are likely to be relevant beyond the olfactory bulb, since γ-rhythms are arise in many brain areas and can exhibit task-dependent coherence. Finally, we demonstrate the generality of this type of synchronization in different classes of oscillators and network connectivities.

Altogether, this dissertation describes two topics that are both motivated by observations in the olfactory system.

Acknowledgements

Completing a Ph.D. degree would be impossible without the help from many. Here, I would like to take this opportunity to thank those who have helped me through this journey.

First, I must thank my graduate advisor, Dr. Hermann Riecke, for all his detailed guidance with utmost patience. From the first day I sat into his class till editing advice on this very thesis, instead of directly telling me what is better, he always guides and inspires me to think what better practice can be. More importantly, he has challenged my bold assumptions and hypotheses from every possible aspect to make me think twice before jumping into detail simulations. Furthermore, he treats me as a collaborator not just a student, even the time when I have naïve or silly ideas. He is not only an advisor for research but also a mentor for my academic career. I am grateful that he took me as his student, and I will keep his advice as a guiding light in my future career.

Second, I would also like to thank the members of my thesis committee: Dr. William Kath and Daniel Abrams. Your support and encouragement helped me through the difficult times, and your valuable feedback alerted me potential problems

from a broader area. Additionally, thank you to Dr. Alvin Bayliss, for trusting me to be the lead of TAs for EA4 and helped me through this unique teaching experience. Also, thanks to Dr. Niall Mangan and Madhav Mani, your suggestions on my presentations helped me explain my works clearly and thoroughly.

Third, I would like to thank collaborators in Pierre-Marie Lledo's lab, Dr. Kurt Sailor and Soham Saha. Discussion with you is always fruitful and insightful. Only by cooperating with your group, I realized on the one hand, the limitation of my understanding of the field, and on another hand, the prediction power of my work. These valuable experiences helped me understand the limitation and potential of myself. Furthermore, I would like to thank my colleagues, Xize Xu, Avinash Karamchandani, Eugene Park and Dr. Lae Un Kim for sharing the happiness and worry, fulfillment and anxiety all along this journey with me. It is your company that make all this means.

Last and utmost, I want to thank my family. To my wife, Beth Yanjin Mi: Thank you so much for your love and support for the past four years. It is your unconditional belief in me that help me through the hardest days. We have experienced so many wonders in these years, and we will witness the greatness of this era together. To my son, Theodore Jiajia Meng: Thank you for all the laughter you bring us, and for presenting the amazing learning ability of such tiny neuron network. To my parents:

Thank you for the huge support to me all these years, which offers gives me the courage and initial momentum to start this journey.

Table of Contents

List of Tables

List of Figures

between mitral and granule cells. (C) An effective self-inhibited network of mitral cells that are calculated from (B). The numbers beside the connections represent the effective inhibition strength. For example, the 1st and 3rd mitral cells both connect to the 1st and 3rd granule cells, thus the effective inhibition strength between the 1st and 3rd mitral cells is 2. (D) The mitral cell activity before training. (G) The mitral cell activity after training. (E, H) The connectivity between mitral cells and granule cells before and after training, respectively. Each white dot represents a connection between the corresponding mitral and granule cell. (E) is a homogeneous random network in which each granule cell has the same number of connections. (F, I) The effective connectivity of the self-inhibited network. The color represents the number of granule cells that pair of mitral cells is connected to. As a result, the color also indicates the effective coupling coefficients between mitral cell pairs. 45

1.5 Memory effect of the model. (A) Training protocol to show the memory effect. We first train our model with the same pair of odors as in Figure 1.4A. Then we train with new odor pair 2. (B, D) The stimuli of odor pair 2 and pair 1 are dissimilar and similar,

(D) Effective network structure $W^{(mm)}$ at end of training phases by training with dissimilar stimuli. The network remembers the previously trained structure. (E) Same as (D) but for training with similar stimuli. The network forgets most of the previously trained structure. (F) Fisher discriminant of odor pair 1 as a function of training time when training with the dissimilar odor pair during phase 2. The value remains high after initial training, which indicates that the memory is not forgotten. (G) Same as (F) but for using the similar odor for phase 2. The Fisher-discriminant of pair 1 decreases during phase 2, indicating that interference introduces forgetting. After re-training with odor pair 1 in phase 3, the Fisher discriminant returns to the original value, which indicates the learning ability is intact. Note that the re-training speed is faster than the training. 60

1.11 Alternating training does not impair learning ability. (A) Expanding the training protocol as in 1.10A to 10 phases. (B) The fisher discriminant of odor pair 1 (top) and pair 2 (bottom). Notice that the learning speed (of increasing of Fisher discriminant for one pair) and forgetting speed (of decreasing of Fisher discriminant for

called activated. (D) is mitral cell activity after training, which is comparable with Figure 1.4 H. (E) is connectivity $W^{(mg)}$, which is comparable with Figure 1.4 I. (F) is effective connectivity $W^{(mm)}$, which is comparable with Figure 1.4 J, except the background is brighter. However, noticing the mitral cell at the background is almost 0, even though the background connection is indeed denser, it does not contribute much to the overall inhibition. 64

1.14 The overall inhibition of the model does not depend on the inhibitory strength γ. The results are organized in figure 1.13 except varying the rescaled inhibitory strength γ instead of number of granule cells. To allow a direct comparison, $N_{gc}^{(new)}$ and $W^{(mm)}$ have been rescaled in (C) and (F) by $\frac{\gamma^{(new)}}{\gamma}$. (F) is comparable with Figure 1.4 J, except the background is brighter. However, as stated in Figure 1.13, the overall inhibition is not impacted. 65

1.15 Increasing $G^{(1)}$ impairs the ability to form connections between activated mitral cells and granule cells. The results here are generated by training with easy stimuli in Figure 1.4A with a random initial network as in Figure 1.4 E. (A, B) The maximal and mean mitral cell activity after training as a function of $G^{(1)}$, respectively. The grey line indicates the theoretical maximum by

removing all the inhibition as is the case when $\gamma = 0$. (C to E) Model results by training with $G^{(1)} = 0.5$. (C) Mitral cell activity after training. (D) Connectivity between mitral and granule cells $W^{(mg)}$. (E) Effective connectivity matrix $W^{(mm)}$. (F to H) are as (C to E) except with $G^{(1)} = 5$. By increasing $G^{(1)}$, the activated mitral cell receive fewer connections with granule cells after training as shown in (A, B), which are reflected by the sparser density in $W^{(mg)}$ (D, G) and the cooler color in $W^{(mm)}$ (E, H). As a result, the mitral cell activity is higher (C, F). In (H), when $G^{(1)} = 5$, most of the granule cells cannot reach this high threshold. As a result, the synapses that connect to the activated mitral cells are removed faster than the background. Thus, the effective connectivity among the activated mitral cells is lower than the background. 67

1.16 Learning ability is not influenced by different $G^{(0)}$. The results here are generated by training with the easy stimuli in Figure 1.4A with a random initial network as in Figure 1.4E. The results here are organized as Figure 1.15. (C to E) Model results by training with $G^{(0)} = 0$. (F to H) Model results by training with $G^{(0)} = 2$. The forgetting effect is changed though by having different $G^{(0)}$, which we will discuss in the next figure, Figure 1.17. 68

1.17 Increasing $G^{(0)}$ leads to less forgetting when trained with an interfering protocol. The results are generated by first training the model with one pair of hard stimuli (odor pair 1, blue curves in (A)), then by training with another pair of hard stimuli (odor pair 2, green curves in (A)), which is the same as the two pairs in Figure 1.10A before the switch 2. (A) Training stimuli. The model is first trained with odor pair 1, indicated by the two blue curves, which is the same as in Figure 1.10B, then the model is trained with odor pair 2, indicated by two green curves in, which is the same as in Figure 1.10C right figure. (B) The discriminability of odor pair 1 before and after the training with the interfering odor pair 2 (1.10C right figure) as a function of $G^{(0)}$. (C, D) Results for $G^{(0)} = 0$ after training with the odor pair 2. For $G^{(0)} = 0$, the model does not have the ability to remember: the connections between the mitral cells that are active by the odors in pair 1 have been removed (cool color in the center of $W^{(mm)}$) (C). (E, F) Results for $G^{(0)} = G^{(1)} = 2$ after training with a similar odor pair. For $G^{(0)} = G^{(1)}$, the model does not include an activity-dependent removal mechanism. In this case, previously learned network

vanishing noise, $\sigma = 0$ (A1). Partial, oscillatory synchronization for $\sigma = 0.025$ (A2). Almost complete synchronization for $\sigma = 0.07$ (A3). B) Lower panel: temporal mean and standard deviation of the global order parameter r_{global} showing a discontinuous transition to an ordered regime as the uncorrelated noise is increased. Upper panel: mean local order parameter $\bar{r}_{local}$ decreases with noise. 122

CHAPTER 1

Hebbian type model of structural plasticity

1.1. Introduction

Reorganization of connectivity between neurons through activity-dependent functional modification has shown potential in explaining the mechanisms behind learning and memory. In motor cortex, the synaptic connections *in vivo* can show an increased turn-over rate within hours when trained with a novel motor skill [2]. In addition, The specific stabilization of newly formed spines, which constitute the postsynaptic portion of excitatory synapses, correlates with memory function [2, 3]. Furthermore, specifically removal of these newly formed spines deteriorates the performance of the animals [4]. These results suggest a close correlation between cognitive functions and structural plasticity in the motor cortex.

The olfactory bulb, which is the first brain region to receive odor information, also shows significant structural plasticity even in mature animals [5], while most brain areas have remarkably stable dendritic spines in adult life [6, 7, 8]. Over a 2-day interval, newly formed spines between mitral and granule cells, which are the principal cells and interneurons in the olfactory bulb, respectively, can count for 20%

of total spines in the adult olfactory bulb of mice [9]. However, the functional role of this structural plasticity is not clear.

As proposed a century ago by Ramón y Cajal, the pioneer of the field, the dynamism of connections underlies learning in an experience-dependent manner [10]. Indeed, mice can show extraordinary ability in learning odors on a timescale similar to that of structural plasticity [11], which suggests that the structural plasticity may be related to the learning process. This learning can be reflected by the extent of pattern separation in mitral cells, which is not observed in the input to the bulb [12]. Complicatedly, the mitral cells can show different behavior depending on the difficulty of the tasks [11]. The mechanisms behind these rich dynamics are still unclear.

Besides structural plasticity, neurogenesis and synaptic weight plasticity can also contribute to the learning of the bulb. In the rodent, new granule cells keep integrating into the existing network throughout life. Without adult-born neurons, mice show deteriorated ability in fine discrimination [13]. However, this malfunction is not shown in discriminating very different odorants [13]. Further, the neurogenesis in the adult olfactory bulb is a species-specific behavior and it is absent beyond age 2 in humans [14], which limits the generality of the functional role of neurogenesis. Synaptic weight plasticity has been studied by experiments and models for decades. Though synaptic plasticity between the mitral and granule cells has been observed in

the bulb, most of the common experimental protocols that trigger a consistent change of synaptic weight in other brain regions lead to potentiation in some of the synapses and depression in others in the olfactory bulb, and these weight changes are limited within 20% of the initial value [15]. Based on these results, synaptic weight plasticity in the olfactory bulb seems less likely to be connected with learning-dependent behaviors.

In contrast to synaptic weight plasticity, structural plasticity in the olfactory bulb clearly shows activity dependence. In the olfactory bulb, the dendrites of the granule cells form and remove filopodia, which have been observed as to be precursors of dendritic spines, on a timescale around 10 minutes [16]. Filopodia are also formed on the spine heads. Lifetime and orientation of these spine head filopodia indicates the subsequent amplitude and direction of spine displacement on the granule cells in the olfactory bulb, respectively [17]. Further, directional motions of filopodia respond to mitral cell stimulation [17]. In addition, the formation of filopodia depends on N-methyl-D-aspartate (NMDA) receptor activation on the granule cell dendrites [16]. Further, in general, the activation of NMDAR depends on the voltage of the dendrite [18], which implies the formation of the filopodia depends on the granule cell activity. Taken together, structural plasticity in the olfactory bulb likely follows a Hebbian-type rule.

Here we show how a Hebbian-type model of structural plasticity can explain the dynamics of mitral cells in the olfactory bulb at both the ensemble and individual levels. Further, we predict mice should perform worse when switching between similar tasks. At the same time, we suggest the emerging of self-organized subnetworks, which may serve as functional units in the neuron network. Last, we discuss the impact of varying the major parameters in our model. Overall, our biologically feasible parsimonious model reveals how the local self-organizing mechanism of structural plasticity can contribute to olfactory learning and memory.

1.2. Model

1.2.1. Mitral cells and granule cells

We now describe the specifics of our model. The neuronal networks in the olfactory bulb can be simplified into two layers of neurons with inputs from glomeruli in the syperficial layer (Figure 1.1A, also seen in [19]). As in [9, 20], mitral and granule cells are described by firing-rate models governed by the ordinary differential equations:

$$\frac{d\boldsymbol{M}}{dt} = -\boldsymbol{M} + F_M(\boldsymbol{S} - \gamma \boldsymbol{W}^{(mg)}\,\boldsymbol{G}), \tag{1.1}$$

$$\tau_G \frac{d\boldsymbol{G}}{dt} = -\boldsymbol{G} + F_G(\left(\boldsymbol{W}^{(mg)}\right)^T \boldsymbol{M} - g_{thr}). \tag{1.2}$$

Here $\boldsymbol{M}$ and $\boldsymbol{G}$ are vectors of size N_{MC} and N_{GC}, respectively, representing the firing rates of N_{MC} mitral cells and N_{GC} granule cells. The mitral cells receive sensory

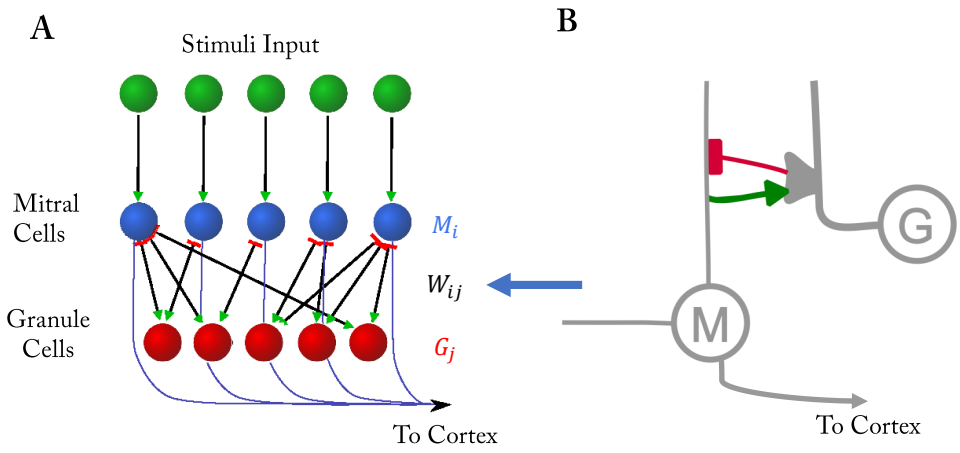

Figure 1.1. Cartoon of our model. (A) We simplify the neuronal network in the olfactory bulb into stimuli input, mitral cells, and granule cells. Mitral cells are excitatory cells and granule cells are inhibitory cells. Connections between mitral cells and granule cells are reciprocal. Mitral cells are the output cells of the bulb which innervate piriform cortex. (B) A sketch of the reciprocal dendro-dendritic connection between mitral and granule cells. Spines are on the dendrite of granule cells. Mitral cells generate feed-forward excitation to cortex.

inputs $\boldsymbol{S}$ and inhibitory input from granule cells, with γ denoting the inhibitory strength. The granule cells receive excitation from mitral cells, with $g_{thr} > 0$ setting a non-zero firing threshold for the granule cells. The non-decreasing non-negative activation functions for $\boldsymbol{M}, \boldsymbol{G}$ are $F_{M,G}$, respectively.

Since our model does not have recurrent excitation, for steady input and fixed connectivity $\boldsymbol{W}^{(mg)}$, the neuronal activities always converge to a global steady state [21]. Further, the chosen timescale doesn't impact the steady state of the system.

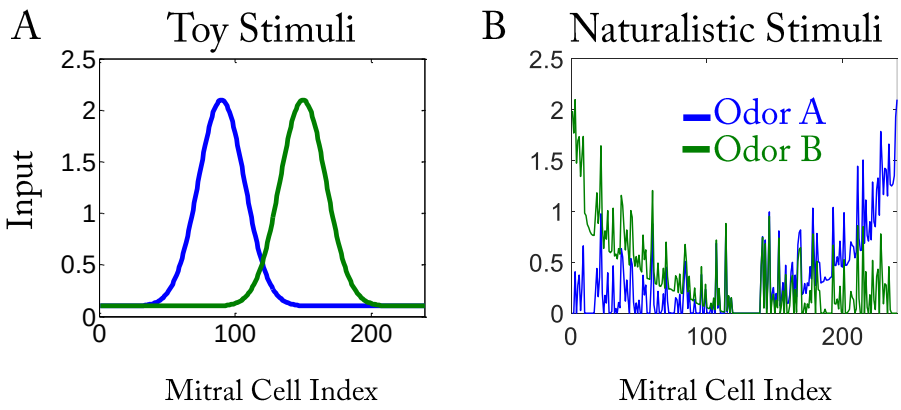

Figure 1.2. Examples of different stimuli in our model. (A) Toy guassian stimuli (B) Naturalistic stimuli.

For simplicity, in our simulation, the timescale for granule cells is $\tau_G = 0$. As a result, the granule cells activity is always at the fixed point in 1.2. In the following, neuronal activities $\boldsymbol{M}, \boldsymbol{G}$ always refer to the firing rates in this steady state. We solve the equations via ODE45 in Matlab.

1.2.2. Sensory Inputs

For the sensory inputs $\boldsymbol{S}$, we use toy stimuli for illustrating the mechanism and use naturalistic stimuli to compare with the experimental data (Figure 1.2). The toy stimuli are gaussian distributions over different mitral cells with constant spontaneous activity added. The naturalistic stimuli are generated from experimental data as follows:

The original glomeruli data comes from Leon's lab [1], which contains 2-d imaging z-scores of the glomeruli responses for a variety of odorants.

The odorants we used in our simulations are carvone, citronellol (pre-training), ethylbenzene, heptanal (training, pure and mixture). In the original data, not all pixel values were available for all odorants. We only keep the common set of them. The total number of data points remaining is 2074. We further downsample the data to 240 sample points $\boldsymbol{S}^{(orig)}$.

The original z-score $\boldsymbol{S}^{(orig)}$ does not include the baseline activity of the glomeruli. A z-core of 0 means the activity equals the average activity across the whole population, but does not mean the activity is not changed when an odor is presented. To obtain a rough calibration of the mean activity we use the observation that around 60% of mitral cells are activated by any given strong stimuli [22]. Since no other information seems available, we use this as a guide to re-calibrate the 40% percentile z-score $S^{(40\%)}$ as 0. Then, we normalize the data by their maximum. As a result, we have the modified value $\tilde{\boldsymbol{S}} = \frac{\boldsymbol{S}^{(orig)} - S^{(40\%)}}{\max(\boldsymbol{S}^{(orig)} - S^{(40\%)})}$. Further, mitral cells are activated by the air flow even without any odorants and odor representations change mostly linearly with the concentration of odorants [23]. Based on that observation, for any given mixture with concentration p of odor A and $(1-p)$ of odor B, we take as the mixture stimulus

$$S = [p\,\tilde{S}^{(A)} + (1-p)\,\tilde{S}^{(B)} + \tilde{S}^{(0)}]_+$$

with $\tilde{S}^{(0)} = 0.1$ is an air stimulus and $[\cdot]_+$ is the rectifier: $[x]_+ = \max(x, 0)$.

For pure odorants, we just set $p = 0$ or $p = 1$ for the corresponding odor.

In the experiments [11], when the mice are trained to distinguish a pair of odor S+/S-, only S+ or S- is presented in a trial with equal probability. In the comparison with these experiments, in each trial of our simulation, the stimulus S is randomly chosen as A or B from a given pair of odors A and B.

1.2.3. Activation function

The neuronal network within the olfactory bulb is an excitatory-inhibitory network. To guarantee the firing rate is positive, the activation function is required to be positive. Further, mitral cells within the olfactory bulb experience saturation behavior. In [23], the authors recorded responses of mitral cells when the concentration of odorant changes within 10-fold. Among the recorded cells, 38% of mitral cells respond linearly to stimuli and 29% of the mitral cells experience saturation behavior. This saturation may be a result of saturated stimuli input or the saturation behavior of mitral cells. In this study, we are interested in the mixture of odors and the concentration of an odorant changes linearly. Based on the experiments from [24], the olfactory sensory neurons saturate on a log scale of odor concentration that changes 1000-fold. Therefore a change in the concentration by a factor of 10 will probably not lead to significant saturation. Thus, we assume the activation function of mitral cells

saturates and it saturates on a linear scale. Taken together, the activation functions in our model are:

$$F_M(I_M) = [\tanh(I_M)]_+, \tag{1.3}$$

$$F_G(I_G) = [(I_G)]_+, \tag{1.4}$$

1.2.4. Connectivity

We record the presence or absence of a reciprocal dendrodendritic synapse between a mitral and a granule cell in a connectivity matrix $\boldsymbol{W}^{(mg)}$. Since in the experiment, learning-dependent structural plasticity is observed [16, 17] and the origin of the synaptic weight plasticity is still unclear [15], we assume that the birth of synapses happens at a faster timescale and the weight of matured synapses is a constant. As a result, only synapses with weight zero or a fixed value should be observed. For simplicity, in our model, the synapses in our model are binary, which means the entries in $\boldsymbol{W}^{(mg)}$ are 1 and 0. It is possible to include synaptic weight values other than 0 to 1 to represent synaptic weight plasticity. However, since it is not the focus of this study, we will not include it in the current model.

Since it is suggested that the lateral inhibition in the olfactory bulb is only weakly spatial specific [25, 26], we do not include any spatial limitations of the connections

in this model. Thus, the ordering of the mitral cells is arbitrary. In our model, as an initial condition, each granule cell randomly connects to the same number N_{conn} of mitral cells, which means each column of $\boldsymbol{W}^{(mg)}$ has N_{conn} non-zero entries. The number of synapses on each granule cell is able to be modified by activity-dependent plasticity, which is explained below.

1.2.5. Activity-dependent structural plasticity

The focus of this model is the structural plasticity of the synapses, and recent studies [16, 17] support an activity-dependent evolution of $\boldsymbol{W}^{(mg)}$. In experiments, the lifetime and orientation of filopodia, which have been observed as to be precursors of spine heads, shows correlation with amplitude and direction of spine heads movement, respectively [17]. In addition, these dynamics are triggered by pre-synaptic glutamate release [17]. At the same time, the frequency of birth and death events of filopodia shows correlation with N-methyl-D-aspartate receptor activation. In general, the NMDAR activation triggers a rise in $[Ca^{2+}]$ and has a bidirectional control to either grow or shrink the spine head [27, 28]. For convenience, the direction of a reciprocal synapse in this dissertation is defined by the excitation, which means mitral cells are pre-synaptic and granule cells are post-synaptic. Thus, in our model, the formation and removal of a synapse is assumed to depend on the firing rates of

the pre-synaptic mitral cell i and of the post-synaptic granule cell j that are connected by that synapse. Inspired by the BCM model [29], we express the formation and removal rates in terms of a single rate function,

$$R_{ij}(M_i, G_j) = M_i\, \phi(G_j) \tag{1.5}$$

Here M_i, G_j are the ith and jth mitral and granule cell steady activity, respectively. The activation function $\phi(G_j)$ changes sign at a threshold $G^{(1)}$ (figure 1.1B), which means the structural plasticity has a bidirectional dependence on the granule cell activity

$$\phi(G_j) = [G_j - G^{(0)}]_+ \,(G_j - G^{(1)}), \tag{1.6}$$

Here $G^{(0)}$ is a threshold below which the structural change is negligible and $G^{(1)}$ is a threshold that controls whether a synapse is formed or an existing synapse gets removed.

Specifically, in each trial with length Δt, which is one step in our simulation, the probability of the formation of a new synapse is

$$\mathcal{P}_{ij}^{+} = 1 - \exp\left(-\frac{[R_{ij}]_+\ \Delta t}{\tau_f}\right), \qquad \text{if } W_{ij}^{(mg)} = 0. \tag{1.7}$$

Conversely, the probability of removal of an existing synapse is

$$\mathcal{P}_{ij}^{-} = 1 - \exp\left(-\frac{[-R_{ij}]_+\ \Delta t}{\tau_r}\right), \qquad \text{if } W_{ij}^{(mg)} = 1\,. \tag{1.8}$$

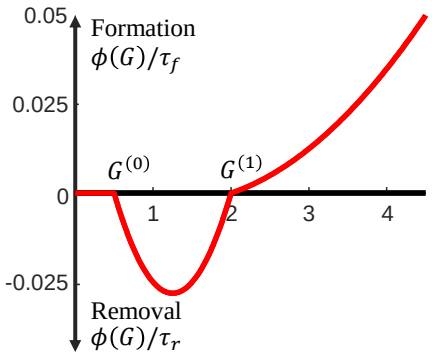

Figure 1.3. Plotted is ϕ/τ_f for $\phi > 0$ and ϕ/τ_r for $\phi < 0$ (cf. Eq. 1.7 and 1.8)

Here τ_f, τ_r are the formation and removal timescale, respectively. The effect of activity of a granule cell on the formation/removal of synapses on the same granule cell is shown in Figure 1.3.

Further, since in experiments the change in the total number of synapses appears to be limited [30, 31], we hypothesize that there exist some stability mechanisms to keep the total number of synapses on the same granule cell within a reasonable range, which is a common requirement for Hebbian plasticity models [32]. For simplicity, we introduce top-k competition as a normalization mechanism as follows. If there are more than k synapses, where $k = \kappa N_{conn}$ with a factor $\kappa > 1$, that are on the same granule cell, only the top k synapses with largest R_{ij} would survive to the next step. As a result, the number of synapses on each granule cell is limited below

N_{MC}	240	N_{GC}	1000
N_{conn}	60	κ	1.1
τ_G	0	Δt	1
g_{thr}	4.4	γ	5e−4
$G^{(0)}$	1	$G^{(1)}$	4
$1/\tau_f$	0.005	$1/\tau_r$	0.05

Table 1.1. Table of parameters. The parameters for the model unless stated otherwise.

$k = \kappa N_{conn}$ while the initial number of synapses is N_{conn}. This top-k competition can be realized by a resource-pool competition with additional assumptions, as discussed later. However, since other mechanisms like scaling [33] or the ABS (Artola, Bröcher and Singer) rule [34] may alternatively restrict the total number of synapses one granule cell can have, and the stability mechanism is not the focus of this project, we will keep the top-k competition without directly stating which specific biologically feasible mechanism causes it.

1.2.6. Summary of the model

Here is a summary of our algorithm. In each step with size Δt in the simulation, we first calculate the steady state of the firing rate of mitral $\boldsymbol{M}$ and granule cells $\boldsymbol{G}$ by given a random odor $\boldsymbol{S}$ from the learning odor pairs. Then, we calculate the formation/removal rate R_{ij} of all the pairs between mitral cells and granule cells. At last, we evolve our connecting matrix based on R_{ij} by following two steps: first, if there are more than k synapses on any granule cells, only the top k synapses

with largest R_{ij} remain. We will refer to this as a normalization step. Second, evolve the connectivity based on Hebbian learning rules 1.7, 1.8, which is refered to a learning step. The learning step is always preceded by the normalization step to avoid potential artificial oscillations. We simulate the model long enough till the connectivity reaches a statistically steady state based on the discriminability (defined later).

The parameters of our model are listed in table 1.1 unless specified otherwise.

1.3. Results

1.3.1. Hebbian-learning rule explains the gain-control mechanism in the case of pure odorants

Previous experiments showed that both perceptual learning [35] and passive learning [22] can elevate the inhibitory drive on mitral cells. We first test whether this is also the case in our model.

We first use a pair of pure Gaussian odorants as input (Figure 1.4A) for our model. We start the simulation with a homogenous random network as the initial homogenous network (Figure 1.4E). The mitral cell activity when using odor A, B and air as input is shown by different color in Figure 1.4D, G. After training, denser connections with activated mitral cells emerge (Figure 1.4H). Accordingly, responsive mitral cells receive more inhibition (Figure 1.4G, comparing to Figure

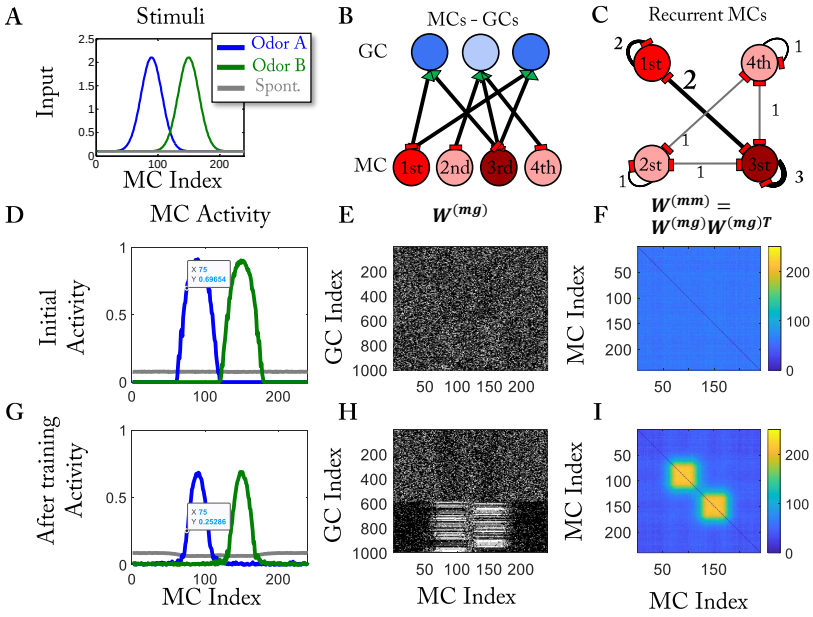

Figure 1.4. Training with pure odorants by using toy stimuli. (A) Training toy stimuli. Noticing different mitral cells respond to the same odor differently. (B) A simplified example for the reciprocal connection between mitral and granule cells. (C) An effective self-inhibited network of mitral cells that are calculated from (B). The numbers beside the connections represent the effective inhibition strength. For example, the 1st and 3rd mitral cells both connect to the 1st and 3rd granule cells, thus the effective inhibition strength between the 1st and 3rd mitral cells is 2. (D) The mitral cell activity before training. (G) The mitral cell activity after training. (E, H) The connectivity between mitral cells and granule cells before and after training, respectively. Each white dot represents a connection between the corresponding mitral and granule cell. (E) is a homogeneous random network in which each granule cell has the same number of connections. (F, I) The effective connectivity of the self-inhibited network. The color represents the number of granule cells that pair of mitral cells is connected to. As a result, the color also indicates the effective coupling coefficients between mitral cell pairs.

1.4D). To better illustrate the impact on mitral cells, we introduce the effective connectivity matrix $W^{(mm)} = W^{(mg)}W^{(mg)T}$ based on the connectivity matrix $W^{(mg)}$ (Figure 1.4B, C), where the entries in $W_{ij}^{(mm)}$ represent the number of granule cells through which the mitral cells i and j inhibit each other disynaptically. The effective connectivity matrix shows a clear organized structure after it has been evolved using Hebbian learning (Figure 1.4F, I).

"Cells that fire together, wire together" is the key element in any Hebbian model ([36], p.70). Our Hebbian model is no exception. If a granule cell responds to the stimulus by integrating excitatory inputs from the connected mitral cells, the other, not yet connected activated mitral cells also have a high chance to form a connection with that granule cell. As a result, if a pair of mitral cells both respond to the same stimulus, the number of granule cells they both connect to increases if the model is trained by the stimulus, which is reflected by the two square components along the diagonal of the effective connectivity matrix (indicated by the hotter color in Figure 1.4I).

1.3.2. Memory effects could be captured by Hebbian-learning

The Hebbian type model is capable of sustaining long-term memory. To test whether our model has a memory or not, we sequentially train our model with two odor pairs (Figure 1.5A). Depending on the similarity of the two training pairs, our model

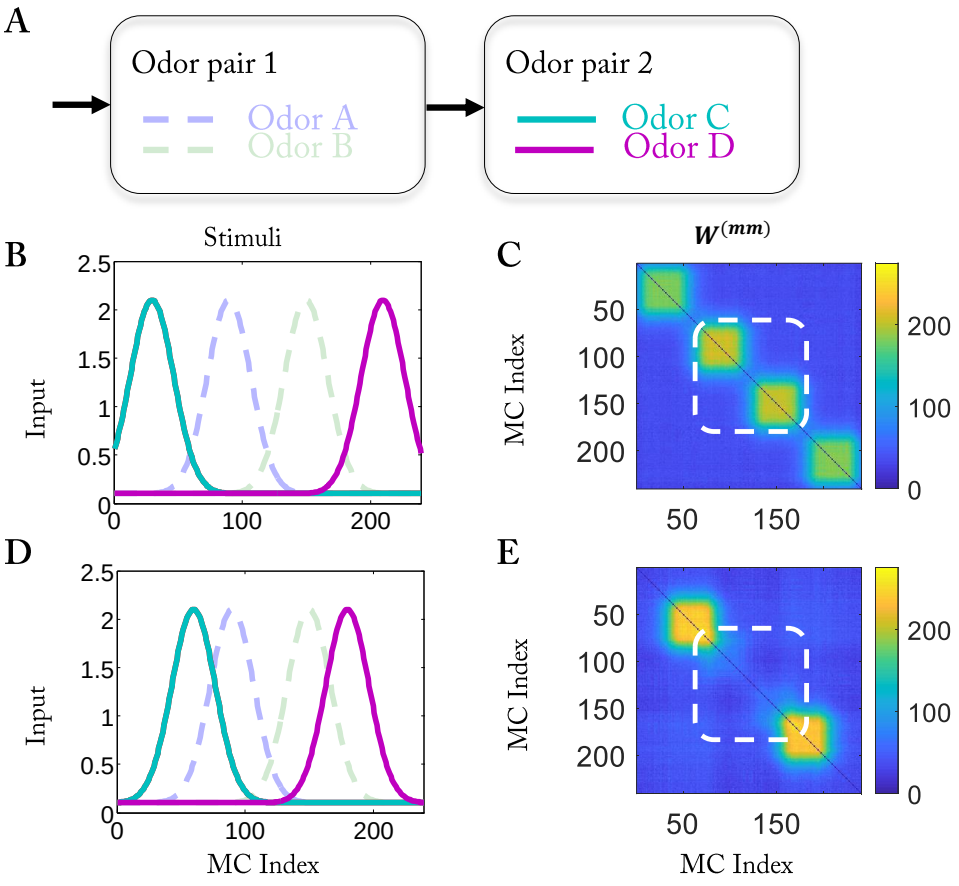

Figure 1.5. Memory effect of the model. (A) Training protocol to show the memory effect. We first train our model with the same pair of odors as in Figure 1.4A. Then we train with new odor pair 2. (B, D) The stimuli of odor pair 2 and pair 1 are dissimilar and similar, respectively. (C, E) The effective connectivity matrix $W^{(mm)}$ when two pairs are dissimilar and similar, respectively. Previously trained network as in Figure 1.4H is circled by white dashed box. (C) If the two pairs are dissimilar, the eventually trained network remembers the previously trained structure; (E) otherwise, the previously trained structure is forgotten.

shows different behavior. If the second training pair is sufficiently different from the first training pair (Figure 1.5B), the eventual connectivity clearly reflects both odor pairs (Figure 1.5C); if the second training pair is similar to the first training pair (Figure 1.5D), the connectivity only reflects the latter odor pair but not the first odor pair (Figure 1.5E). The behavior here means that if the sequential training stimuli interfere with each other, the learning of the new task may be at the expense of forgetting of the previously learned task.

Since our model can "remember" the learned odors by changing its connectivity matrix $W^{(mg)}$, using a homogeneous random network as initial connectivity is somewhat arbitrary since animals in real life always have odor-related memory. The mice used in the experiments have at least smelled food, water, urine and so on in their cages before they were trained to do specific odor discrimination tasks. If a model does not have memory, which means the final output has no correlation with the initial condition, then it can be safely assigned an arbitrary initial condition. However, our Hebbian model does remember previously learned structure, which means we need to discuss the effect of previously learned memory on the current training task.

To test the effect of memory on the learning ability, we test our model based on the experiments [11]. Before we train our model with the pair of pure odorants (Figure 1.4A), we first pre-train our model with another pair of pure odorants (Figure 1.6B).

The initial activity of mitral cells is influenced by the pre-training network (Figure 1.7A). However, at the end of the training, the activity of the mitral cells in response to the stimuli pair is almost the same as in the case without pre-training (Figure 1.7 B). In this case, the learning ability of the model is independent of previous memory. Moreover, due to the similarity between the pre-training and training pairs, the resulting connectivity reflects only the training pair, which is similar to the situation in Figure 1.5E.

1.3.3. Hebbian-learning rule explains the increasing of discriminability during the course of training in the mixture odorants case

The same experiment [11] also shows that the learning-induced change in the activity of mitral cells depends on the difficulty of the training tasks. To specify the effect, the authors of [11] classified the mitral cells as responsive cells, which means the activity of the mitral cell in response to either of the odor is larger than some significance level, and divergent cells, which means the activity difference between the responses to two different odors is larger than another significance level. After pre-training with an easy odor pair, if the mice are trained with an easy task, the number of divergent cells goes down during the course of training as does the number of responsive cells. This behavior can be explained by non-selective increasing of inhibition on every mitral cell, which can be achieved via up-regulating the strength of inhibition in an

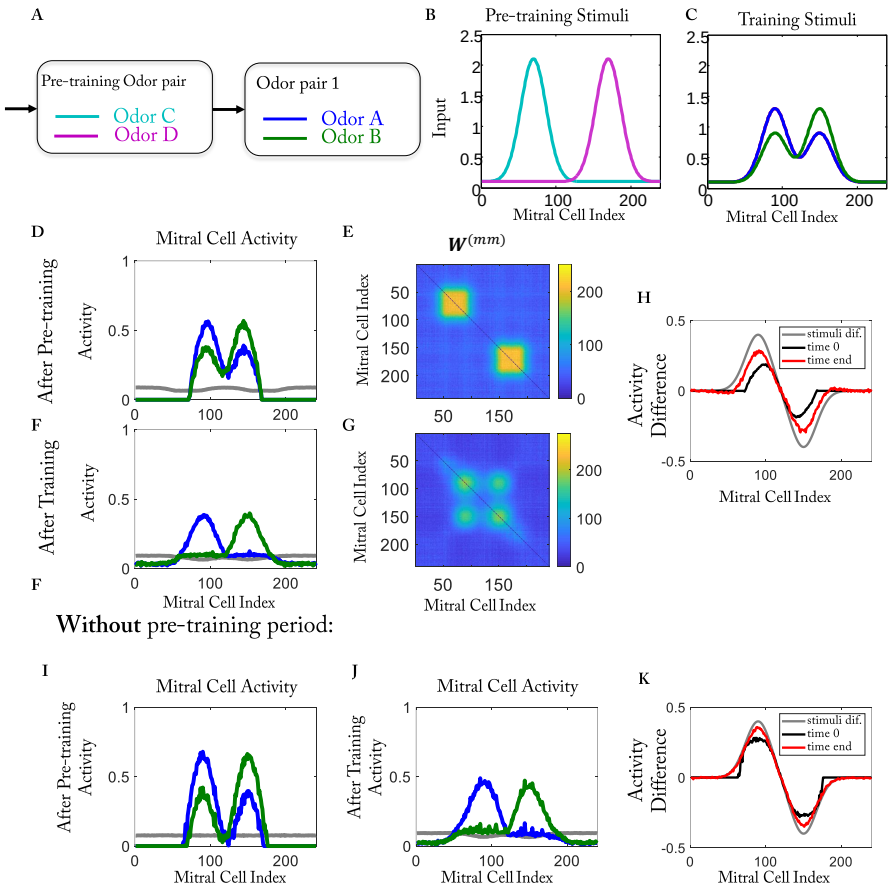

Figure 1.6. Training with mixture odors by toy stimuli. (A) Training protocol to mimic the experiment. (B) Pre-training easy stimuli. (C) Training mixture stimuli. Two mixture odors are represented by different linear combinations of two Gaussian activation curves ($0.6 : 0.4$ vs. $0.4 : 0.6$). (D, F) Mitral cell activity before training (after pre-training) and after training, respectively. See text for details. (E, G) Effective connectivity matrix before and after training, respectively. (H) Activity difference before and after training, represented by the black and red lines, respectively. The grey line is the difference of stimuli input. (I, J, K) Training results like (F, G, H) without a pre-training phase. (I, J) Mitral cell activity before and after training. (K) Activity difference before and after training.

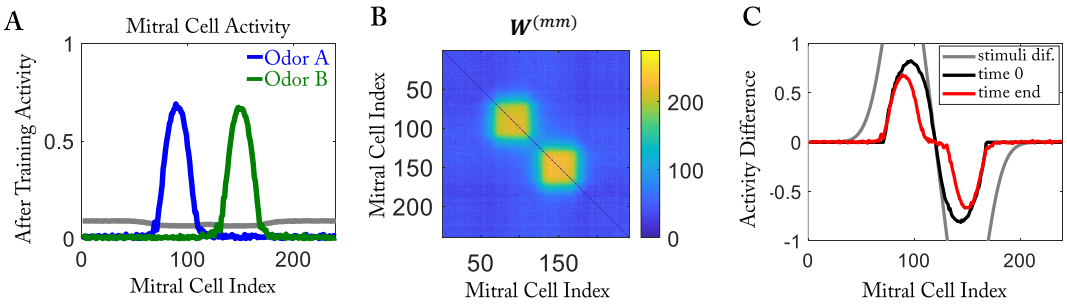

Figure 1.7. Training of an easy task to discriminate pure stimuli with a pre-training phase. The training protocol is the same as in Figure 1.6A. The pre-training stimuli are as in Figure 1.6B. The training stimuli are as in 1.4A . (A to C) are organized as Figure 1.6F to H.

all-to-all network. However, if the mice are trained with a difficult task, which is to discriminate mixtures of two odorants but with different weights, the number of divergent cells does not go down, it may even increase, while the number of responsive cells goes down. This phenomenon cannot be explained by non-selective inhibition. In the following subsection, we discuss how it can be explained by our Hebbian model.

We first describe the definitions of responsive cells and divergent cells in our model, which are adapted from [11]. To start with, we define the response of the mitral cell as the change in activity when given a stimulus in addition to air, which is the background odor in the experiment. Specifically, if a mitral cell has activity $\boldsymbol{M}^{(A,B)}$ in response to stimuli $\boldsymbol{S}^{(A,B)}$, and it has activity $\boldsymbol{M}^{(0)}$ when presenting air as stimulus $\boldsymbol{S}^{(0)}$, then we define the response to odor A, B as $dM_i^{(A,B)} = M_i^{(A,B)} - M_i^0$.

Further, for a given threshold θ, if the response to one odor in an odor pair is bigger than that threshold, $\max(dM_i^{(A)}, dM_i^{(B)}) > \theta$, then the cell is classified as a responsive cell. Further, if the response difference is bigger than the same threshold, $|dM_i^{(A} - dM_i^{(B}| > \theta$, the cell is classified as a divergent cell. Here, we use the same threshold θ to detect responsive cells and divergent cells.

In the training with an easy pair, or in the easy task, most cells that respond to one of the odors in the pair do not respond to the other odor too much. This means the response amplitude to this odor is almost the same as the response difference within the pair. When the new reciprocal synapses are formed between the activated mitral cells and the granule cells, the response amplitude and the response difference both decrease. Using one specific mitral cell as an example (marked dots in Figure 1.4D, G), the response to the pair and the difference both drop from 0.7 to 0.27. As a result, most cells show a decreasing response amplitude and difference. With pre-training, this is also the case. The activity difference goes down with the amplitude of response (Figure 1.7 C). The fraction of responsive and divergent as a function of time shows a similar trend as observed in the experiment (Figure 1.12C).

Consider now training the model with a mixture odorant pair, or hard odor pair (Figure 1.6A, B, C). The mitral cell firing rates are influenced (Figure 1.6D) by the pre-trained network (Figure 1.6E) as expected. After training, the response amplitude decreases as in the previous case of two pure odorants (Figure 1.6F),

which is a result of the reorganized network connection (Figure 1.6G). However, in this case, the response difference is not decreased along with the maximum response amplitude. In fact, there is a large fraction of mitral cells experiencing an increase in the response difference (Figure 1.6H).

The major difference in the mixture case compared to the case of two pure odorants is that the overlapping of the receptive fields of stimuli is much larger. Just as we discussed in the case of two pure odorants, the mitral cells that are co-activated form more effective inhibitory connections. Because of the overlapping of the receptive fields, the effective connectivity matrix has off-diagonal components in addition to the diagonal components (Figure 1.6G). These off-diagonal components have a similar function as lateral-inhibition, which inhibits the lesser activated mitral cells and further increases the discriminability between the pair of stimuli. As a result, the response difference is maintained or even increased while the maximum response amplitude decreases.

We further show that the results is qualitatively similar even without pre-training. To do that, we directly train the model with the homogeneous random network as initial connectivity matrix, as we did in the previous session. At the starting point of the training, the response patterns of the mitral cells in the two cases are different, which reflects that the initial connectivity matrix is different (Figure 1.6D, I). However, after the training, the response patterns are similar to each other (Figure

1.6F, J). Even though quantitative differences remain, in both cases a fraction of mitral cells experience an increase in the activity difference during the course of training (Figure 1.6H, K).

1.3.4. Comparison by naturalistic stimuli: no artificial correlation

So far, we have used toy stimuli to explain the mechanism behind our Hebbian type model. However, the toy stimuli we use introduce an artificial correlation between the response amplitude and response difference of a pair of stimuli (Figure 1.8D, black dots). To avoid this, we use naturalistic stimuli (Figure 1.8C) which were directly adapted from published data from Leon's lab [1]. The naturalistic stimuli do not have the same degree of correlation anymore (Figure 1.8D, red dots).

In this part, our model is pre-trained by a naturalistic pair of two pure odorants and then trained by a naturalistic pure (easy) or mixture (hard) odorant pair (Figure 1.8A). The key difference between the stimuli of the pair is significantly smaller in the hard case than in the easy case. By using these stimuli, our parsimonious model successfully reproduces several experimental observations.

In the easy case, the number of divergent cells decreases along with the number of responsive cells (Figure 1.8E); while in the hard case, the number of divergent cells increases by a small amount though the number of responsive cells still decreases (Figure 1.8F).

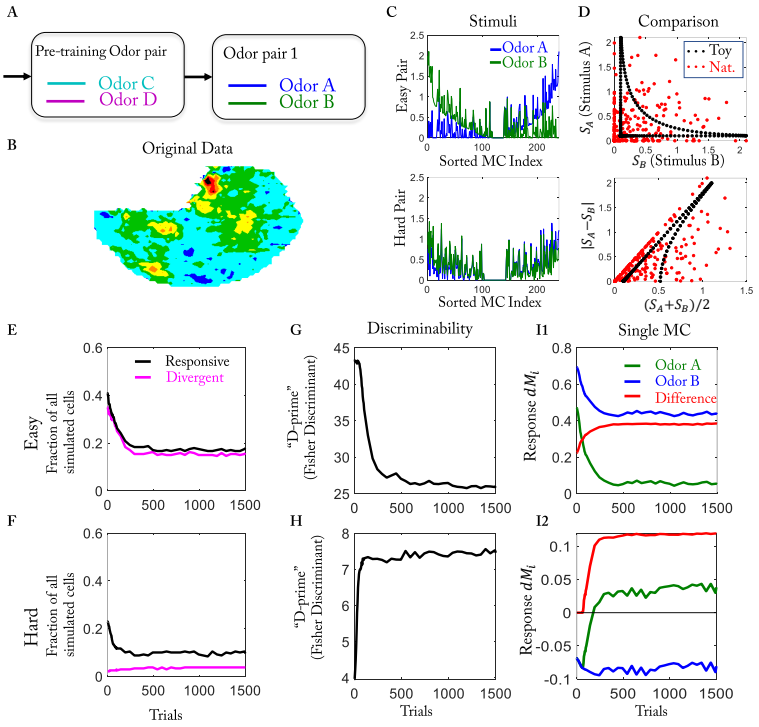

Figure 1.8. Modeling results of training with naturalistic stimuli and comparison with experimental results with $\gamma = 1.7\text{e}{-4}$. (A) The training protocol. (B) Color-coded contour chart illustrating patterns of glomerular evoked by an odorant, which is used as inputs to mitral cells in our model. The figure is regenerated from [1]. (C) Stimuli of the model as the easy pair and hard pair. (D) Naturalistic stimuli show less correlation between the mean response amplitude and the response difference. Top, activation of stimulus S_A over stimulus S_B for each mitral cell. Bottom, $|S_A - S_B|$ over $(S_A + S_B)/2$ for each mitral cell. (E, F) Temporal evolution of the number of responsive mitral cells and divergent mitral cells by training of easy task and hard task, respectively. (G, H) Fisher Discriminant as a measurement to compare with D-prime in the experiment. Plotted is the temporal evolution of Fisher Discriminant of the easy task and the hard task, respectively. (I) Two cases for different individual mitral cell behaviors. (I1) Mitral cell changes from excited by both odors to excited by only one of the odors. (I2) Mitral cell changes from being inhibited by both odors to being inhibited by only one of the odors.

In the experiment [11] , to measure the dissimilarity of two responding patterns, they define D-prime of each divergent neuron as follows

$$d_i' = \frac{|\mu_i^{(1)} - \mu_i^{(2)}|}{pooled\ standard\ deviation}$$

Here $\mu_i^{(1,2)}$ represents the average trace of the GC activities. The pooled standard deviations include temporal variance and noise in the experiment. Then the D-prime for the task is the average of the D-prime of the individual neurons.

$$\text{D-prime} = \text{mean}(d_i')$$

They observed that D-prime decreased in the easy task while increased in the hard task. They argued this reflected a balance between efficiency and robustness [11].

In our simulation, we use the Fisher-discriminant to measure the same dissimilarity. The original definition of Fisher-discriminant between the representations of two stimuli from N channels, which are the mitral cells in our case, is as follows

$$F = \frac{(\boldsymbol{w} \cdot (\boldsymbol{\mu}^{(1)} - \boldsymbol{\mu}^{(2)}))^2}{\boldsymbol{w}^T(\boldsymbol{\Sigma}^{(1)} + \boldsymbol{\Sigma}^{(2)})\boldsymbol{w}}$$

where $\boldsymbol{\mu}^{(1,2)}$ is a vector with entries $\mu_i^{(1,2)}$ which represent the average activity from mitral cell i of the 1st, 2nd representation, respectively; $\boldsymbol{\Sigma}^{(1,2)}$ is the covariance from

the 1st and 2nd representation, respectively; $\boldsymbol{w}$ is a weight vector. To achieve the optimal F, we use the optimal weight $\boldsymbol{w}$ defined by $\boldsymbol{w} = (\boldsymbol{\Sigma}^{(1)} + \boldsymbol{\Sigma}^{(2)})^{-1}(\boldsymbol{\mu}^{(1)} - \boldsymbol{\mu}^{(2)})$.

As discussed in [37], assuming the firing events follow an independent Poisson process for different mitral cells, we have $\boldsymbol{\Sigma}_{ii}^{(1,2)} = \text{mean}(\mu_i^{(1,2)})$ and $\boldsymbol{\Sigma}_{ij} = 0, i \neq j$. Further, we replace $\mu_i^{(1,2)}$ by $M_i^{(1,2)}$.

As a result, the Fisher discriminant is simplified into the expression

$$F = \sum_{i=1}^{N_{MC}} \frac{(M_i^{(1)} - M_i^{(2)})^2}{M_i^{(1)} + M_i^{(2)}}$$

with $M_i^{(1)}, M_i^{(2)}$ are the steady firing rates of mitral cell i of the 1st, 2nd representation, respectively.

The relationship between Fisher-discriminant and D-prime is as follows

$$F \sim \sum_{i=1}^{N_{MC}} (d_i')^2$$

As expected, the Fisher-discriminant successfully reproduces the trend observed in the D-prime (Figure 1.8G, H).

Furthermore, our model reproduces the observation of individual mitral cells. In the experiment, some mitral cells show significant excitation for both odors on day 1 but only for one of the odors on day 7, which we refer to as asymmetric inhibition. Some other mitral cells show significant inhibition for both odors on day 1 but only for one of the odors on day 7, which we refer to as asymmetric disinhibition. In

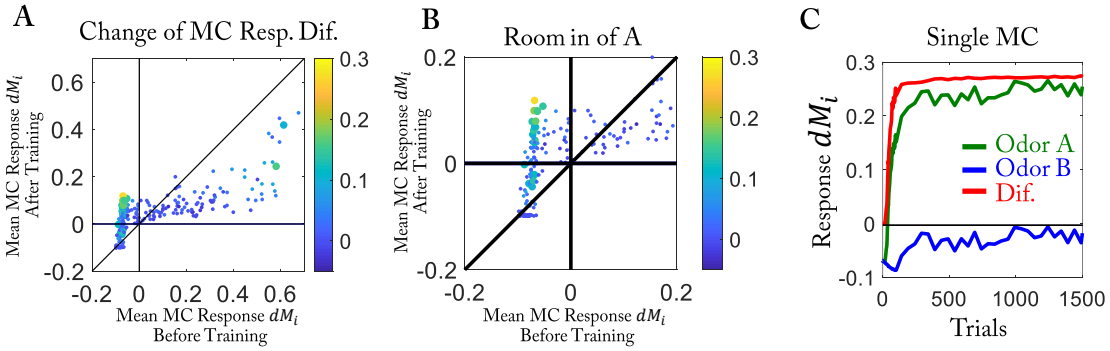

Figure 1.9. Mitral cells with asymmetric activity. (A) Changing of mitral cell response over mean mitral cell activity before and after training. Each dot comes from one mitral cell. The X-axis is the mean mitral cell response before training and the Y-axis is the mean mitral cell response after training. The color means the change in response differences. Bigger dots denote the mitral cells of which activity is at least 0.1 bigger after training than before training. The activity of mitral cells is closer to 0 after training, which represents the re-organization of the network. The cases in Figure 1.8 I1 and I2 are in 1st and 3rd quadrant, respectively. (B) The activity of a mitral cell that falls in the 2nd quarter of (A).

the model, the mitral cell response is defined as the change in activity when given a stimulus in addition to the air. It therefore can be positive, if the odor induces excitation of the mitral cells, and also negative, if the odor induces inhibition of the mitral cells. Both asymmetric inhibition and disinhibition are captured in our model (Figure 1.8I). Further, we find that only a small population of mitral cells shows a significant increase in activity difference (Figure 1.9), which is consistent with the insignificant increase in the number of divergent cells.

1.3.5. Prediction of forgetting when the trained animal is switched back and forth between similar tasks

After successfully capturing the observation of the experiments, our model predicts that just by having structural plasticity, the olfactory bulb can store memory by connectivity. Furthermore, a typical memory effect like forgetting triggered by interference is also predicted to be observable in the bulb. The hypothesis is that when the system is exposed to interfering information, the discriminability between the learned pair should be impaired, or, the system "forgets" the learned task.

To directly show this, we train our model with sequential tasks in three phases (Figure 1.10A). We first train the model with the 1st hard odor pair (phase 1), then switch to train with the 2nd hard odor pair (phase 2). To further show the learning ability is intact and make a connection with real experiment, the model is further trained with the 1st pair again (phase 3, re-training phase).

Indeed, depending on the similarity of the two pairs (Figure 1.10B, C), we observe different behavior from the model. When the two odor pairs are dissimilar, the network structure remembers the previously learned structure (Figure 1.10D), and the Fisher-discriminant of pair 1 remains at a high level after the initial learning (Figure 1.10F). However, if the training odors are similar, interference is observed. In this case, the previously learned structure is forgotten during the training with the interfering odor pair in phase 2. The previously learned structure is re-learned

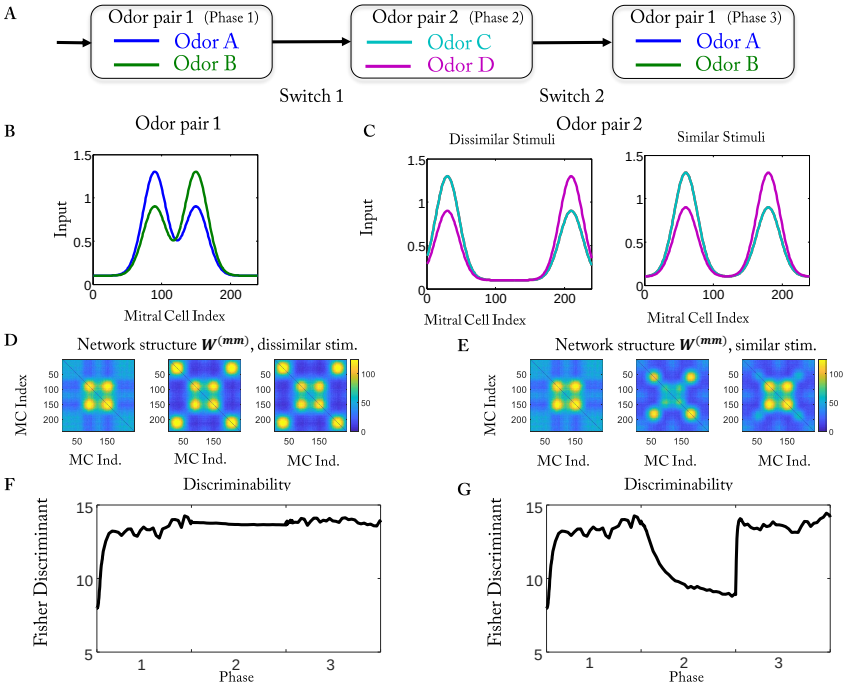

Figure 1.10. Interference should lead to forgetting. (A) Training protocol. The model is trained on odor pair 1 first, then switched to odor pair 2, then switched back to odor pair 1. (B) Stimuli of odor pair 1. (C) Stimuli of odor pair 2 as interference. Left, weak interference: an odor pair with little overlap with odor pair 1. Right, strong interference: an odor pair with large overlap with odor pair 1. (D) Effective network structure $W^{(mm)}$ at end of training phases by training with dissimilar stimuli. The network remembers the previously trained structure. (E) Same as (D) but for training with similar stimuli. The network forgets most of the previously trained structure. (F) Fisher discriminant of odor pair 1 as a function of training time when training with the dissimilar odor pair during phase 2. The value remains high after initial training, which indicates that the memory is not forgotten. (G) Same as (F) but for using the similar odor for phase 2. The Fisher-discriminant of pair 1 decreases during phase 2, indicating that interference introduces forgetting. After re-training with odor pair 1 in phase 3, the Fisher discriminant returns to the original value, which indicates the learning ability is intact. Note that the re-training speed is faster than the training.

by re-training with odor pair 1, which reflects that the learning ability is intact (Figure 1.10E). This result is directly implied by the Hebbian learning rule in our model. For the Fisher-discriminant of pair 1, the value decreases during phase 2. The value increases to the previous value after re-training (Figure 1.10G). Both re-learned connectivity and the re-gained Fisher-discriminant of pair 1 shows the learning ability of the model is intact.

The results for the Fisher-discriminant of pair 1 predict that the mice in a biological experiment should experience deteriorated performance if they are trained with interfering information. Assuming mice are trained under the same experimental protocol (Figure 1.10A), the behavior of the mice at the second switch (Figure 1.10 F, G) should depend on the similarity of the training pairs. If the training pairs are dissimilar, the Fisher-discriminant of pair 1 is comparable at the end of phase 1 and the beginning of phase 3, which predict the similar success rate of the animal at the corresponding time points. However, if the training pairs are similar, or interfering with each other, the Fisher-discriminant of pair 1 shows a significantly decreased value at the later time point, which predicts the mice should have worse performance after training with an interfering odor. In addition, the re-learning speed is faster than the initial learning in our model. At last, we showed that alternating training does not impair the learning ability (Figure 1.11).

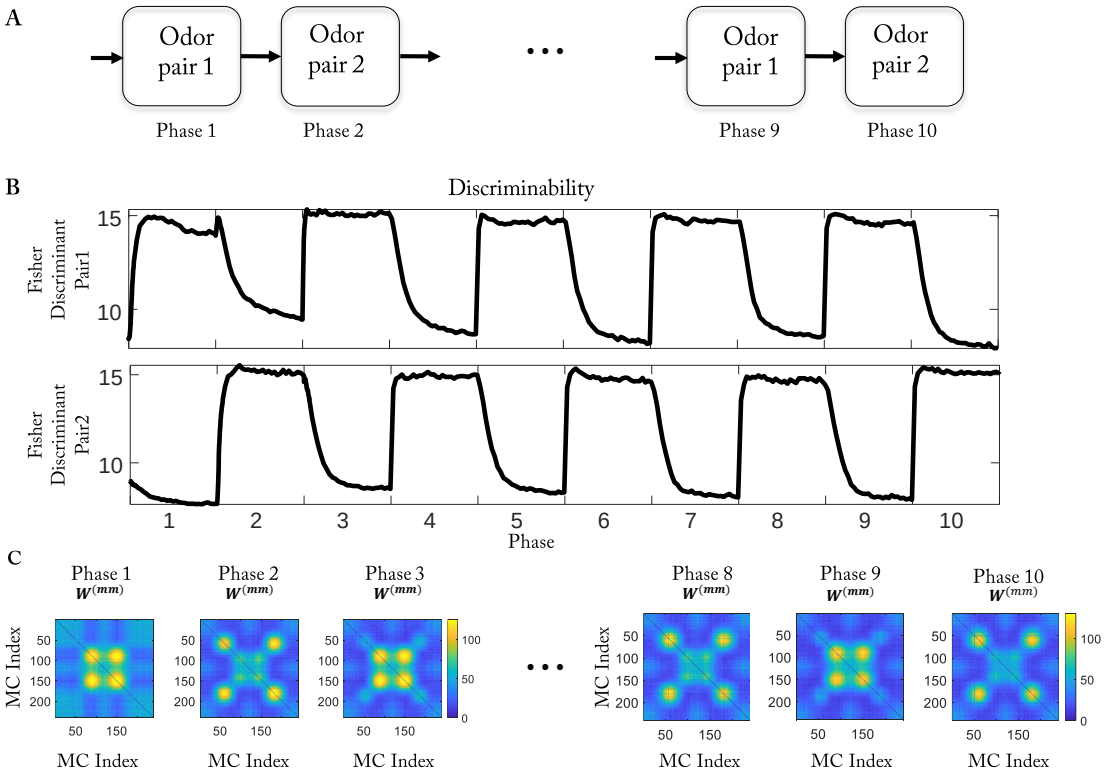

Figure 1.11. Alternating training does not impair learning ability. (A) Expanding the training protocol as in 1.10A to 10 phases. (B) The fisher discriminant of odor pair 1 (top) and pair 2 (bottom). Notice that the learning speed (of increasing of Fisher discriminant for one pair) and forgetting speed (of decreasing of Fisher discriminant for the other pair) are not the same. (C) Effective connectivity $W^{(mm)}$ oscillates as expected.

1.3.6. Impact of major parameters of the model

To test the robustness of our model, we vary the major parameters of the model and see the impact of such modification.

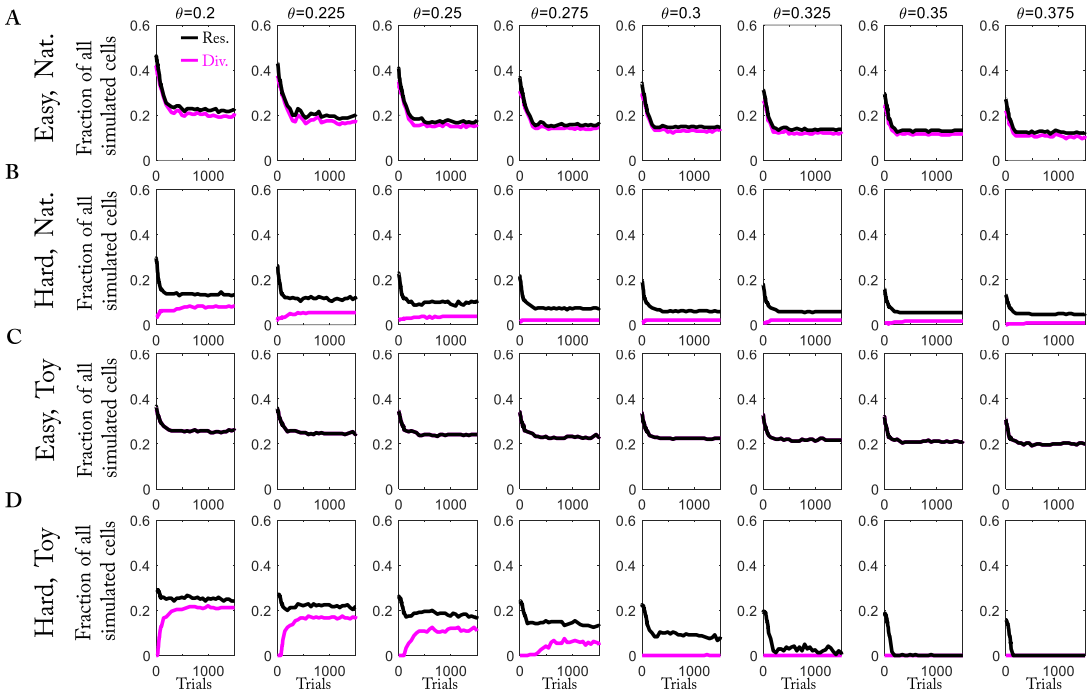

Figure 1.12. Qualitative results of fraction of simulated cells do not depend on the threshold θ for the responsive and divergent cells. (A, B) Results of analyzing naturalistic stimuli by using different threshold θ to classify responsive cells or divergent cells. The results in Figure 1.8 D, E are based on $\theta = 0.25$. (C, D) As (A, B) but of analyzing toy stimuli. As shown here, within some reasonable range, the choice of threshold θ does not qualitatively change our results.

First, we test the threshold θ for detecting responsive cells and divergent cells (Figure 1.12). We also showed that, even for the toy stimuli, the fraction of responsive and divergent cells follows the same trend as observed in the experiments [11] before and after training (Figure 1.12D).

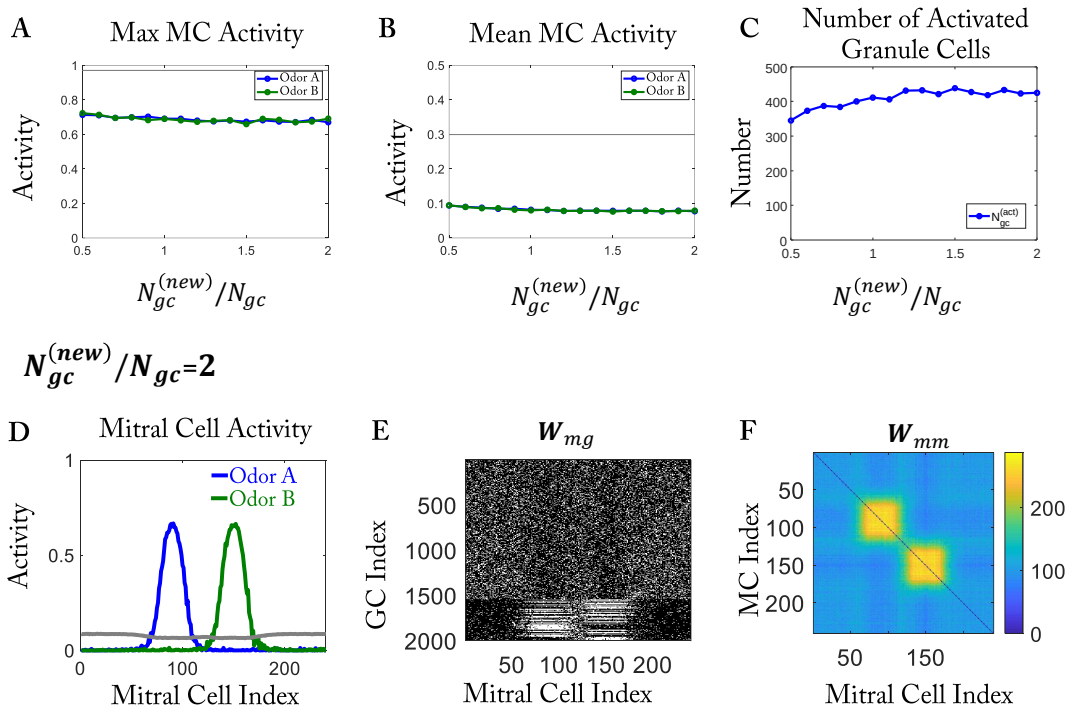

Figure 1.13. The overall inhibition of the model does not depend on the number of granule cells. The results here are generated by training the toy easy stimuli in Figure 1.4A with a random initial network as in Figure 1.4E. (A, B) The maximum and mean mitral cell activity after training as a function of the ratio of the number of granule cells. (C) Number of activated granule cells as a function of the ratio of the number of granule cells. If a granule cell has activity bigger than $G^{(1)}$, it is classified as activated. (D to F) Results by doubling the granule cell number. (C) The number of activated granule cells $N_{gc}^{(act)}$ does not depend on the number of granule cells. If one granule cell has more synapses than N_{conn}, it is called activated. (D) is mitral cell activity after training, which is comparable with Figure 1.4 H. (E) is connectivity $W^{(mg)}$, which is comparable with Figure 1.4 I. (F) is effective connectivity $W^{(mm)}$, which is comparable with Figure 1.4 J, except the background is brighter. However, noticing the mitral cell at the background is almost 0, even though the background connection is indeed denser, it does not contribute much to the overall inhibition.

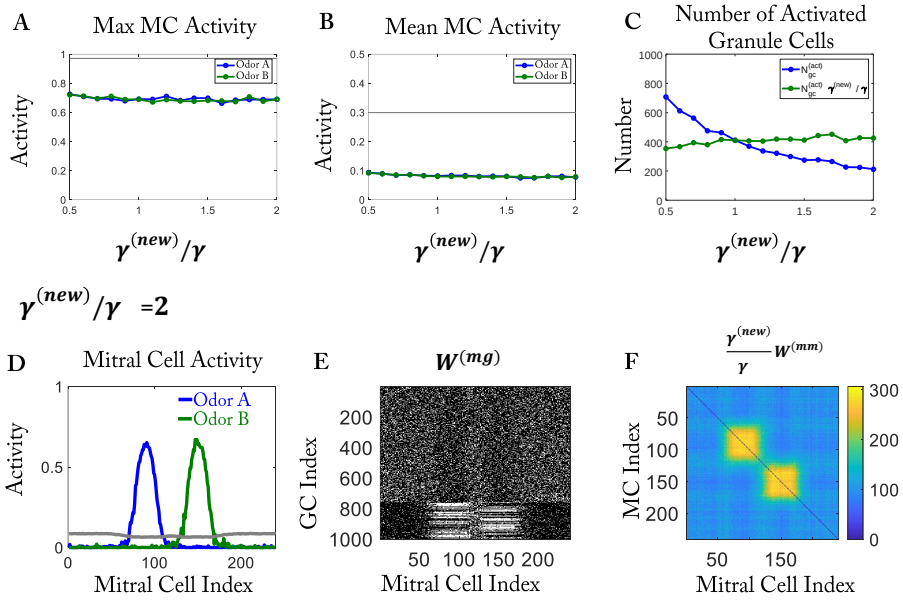

Figure 1.14. The overall inhibition of the model does not depend on the inhibitory strength γ. The results are organized in figure 1.13 except varying the rescaled inhibitory strength γ instead of number of granule cells. To allow a direct comparison, $N_{gc}^{(new)}$ and $W^{(mm)}$ have been rescaled in (C) and (F) by $\frac{\gamma^{(new)}}{\gamma}$. (F) is comparable with Figure 1.4 J, except the background is brighter. However, as stated in Figure 1.13, the overall inhibition is not impacted.

Second, we test whether the inhibition is impacted by the number of granule cells or the inhibitory strength γ. The influence of such modification is minimal even when either value is doubled (Figure 1.13A, B, 1.14A, B). The effective inhibition remains almost the same. Because of the reciprocal character of the connections, the formation of new connections means the mitral cells receive more inhibition, which means the total excitation to the granule cell decreases, which in turn inhibits the

formation of new connections. This stopping point does not depend on the number of granule cells, or inhibitory strength.

Third, we test whether the turning point $G^{(1)}$ in the activation function $\phi(G)$ influences the formation of synapses. The turning point $G^{(1)}$ indicates the unstable fixpoint in the dynamics of the activity of the granule cells. Only granule cells with activity larger than $G^{(1)}$ form more synapses that in turn generate more selective inhibition. By having more synapses, these cells in turn have higher activity. This positive feedback loop stops when the number of synapses reaches k, the upper limit of the number of synapses a granule cell can have. As a result (Figure 1.15A, B), larger $G^{(1)}$ means fewer granule cells have initial activity larger enough, which in turn reduces the selective inhibition.

Fourth, we test whether changing the value of $G^{(0)}$ will influence the selective inhibition. As shown in Figure 1.16, the value of $G^{(0)}$ does not influence the mitral cell activity after training when presenting the learned odor, which is a result from the definition of the model: $G^{(0)}$ affects the removal but not the formation of synapses. However, when $G^{(0)}$ is smaller, the granule cells that primarily connect to the inactive mitral cells would remove the connections with the active mitral cells more easily. To discuss this removal effect in detail, we test the model with a second task that interferes with the previously learned one (Figure 1.17). $G^{(0)}$ controls the threshold to maintain a memory. If $G^{(0)} = 0$, any weak activity ($0 < G < G^{(1)}$) would lead

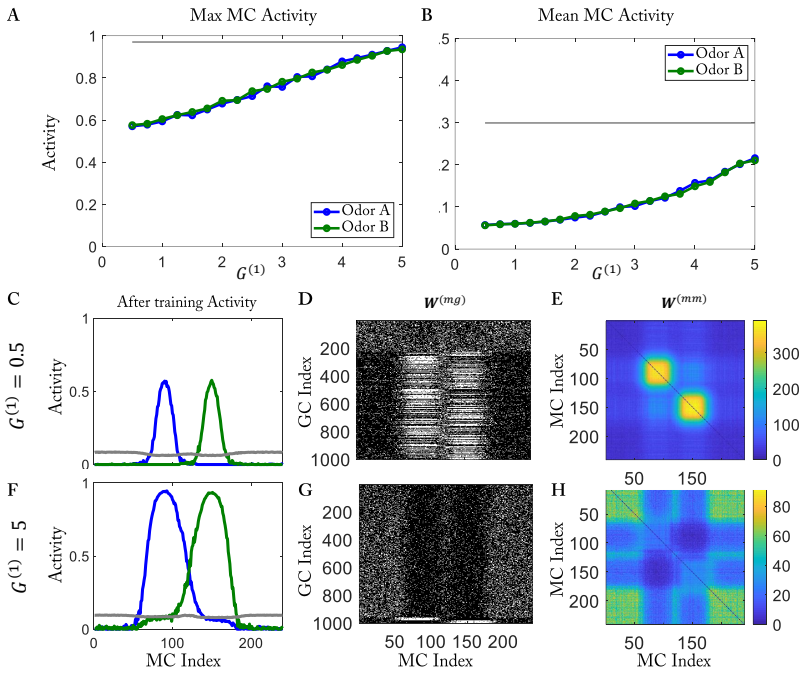

Figure 1.15. Increasing $G^{(1)}$ impairs the ability to form connections between activated mitral cells and granule cells. The results here are generated by training with easy stimuli in Figure 1.4A with a random initial network as in Figure 1.4 E. (A, B) The maximal and mean mitral cell activity after training as a function of $G^{(1)}$, respectively. The grey line indicates the theoretical maximum by removing all the inhibition as is the case when $\gamma = 0$. (C to E) Model results by training with $G^{(1)} = 0.5$. (C) Mitral cell activity after training. (D) Connectivity between mitral and granule cells $W^{(mg)}$. (E) Effective connectivity matrix $W^{(mm)}$. (F to H) are as (C to E) except with $G^{(1)} = 5$. By increasing $G^{(1)}$, the activated mitral cell receive fewer connections with granule cells after training as shown in (A, B), which are reflected by the sparser density in $W^{(mg)}$ (D, G) and the cooler color in $W^{(mm)}$ (E, H). As a result, the mitral cell activity is higher (C, F). In (H), when $G^{(1)} = 5$, most of the granule cells cannot reach this high threshold. As a result, the synapses that connect to the activated mitral cells are removed faster than the background. Thus, the effective connectivity among the activated mitral cells is lower than the background.

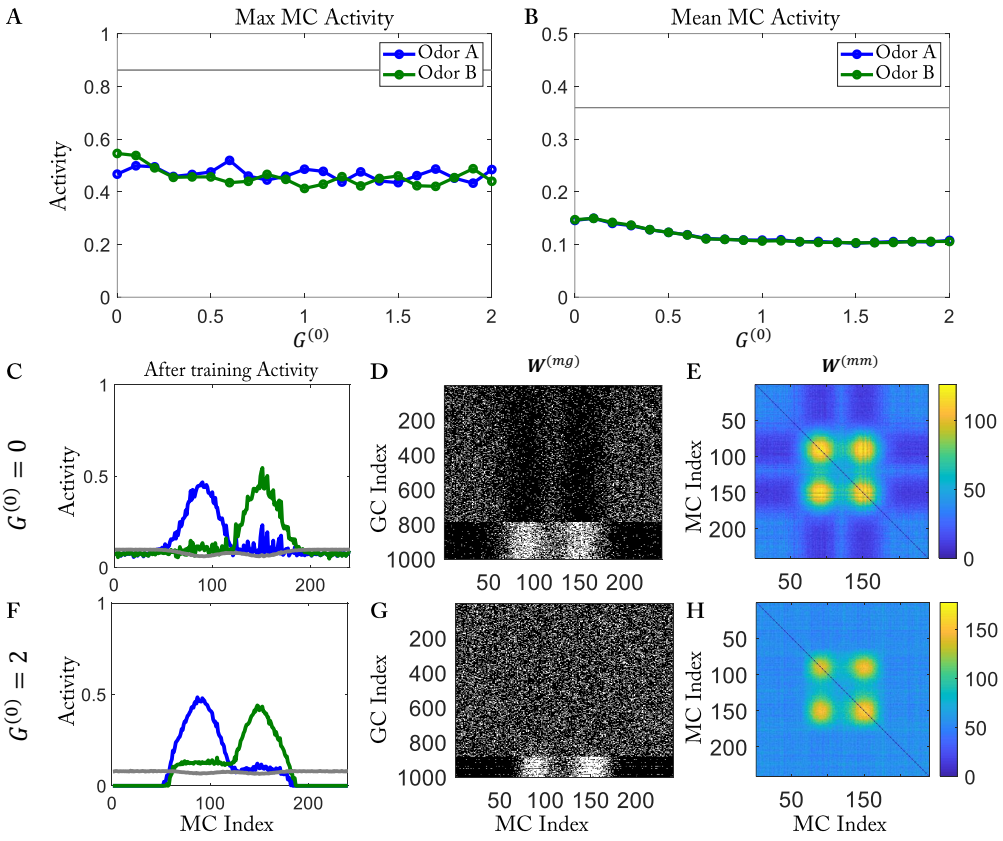

Figure 1.16. Learning ability is not influenced by different $G^{(0)}$. The results here are generated by training with the easy stimuli in Figure 1.4A with a random initial network as in Figure 1.4E. The results here are organized as Figure 1.15. (C to E) Model results by training with $G^{(0)} = 0$. (F to H) Model results by training with $G^{(0)} = 2$. The forgetting effect is changed though by having different $G^{(0)}$, which we will discuss in the next figure, Figure 1.17.

to the removal of spines. Thus, even weak interference leads to the forgetting of all previously learned structure. However, if $G^{(0)}$ is large, then previously learned structure is maintained.

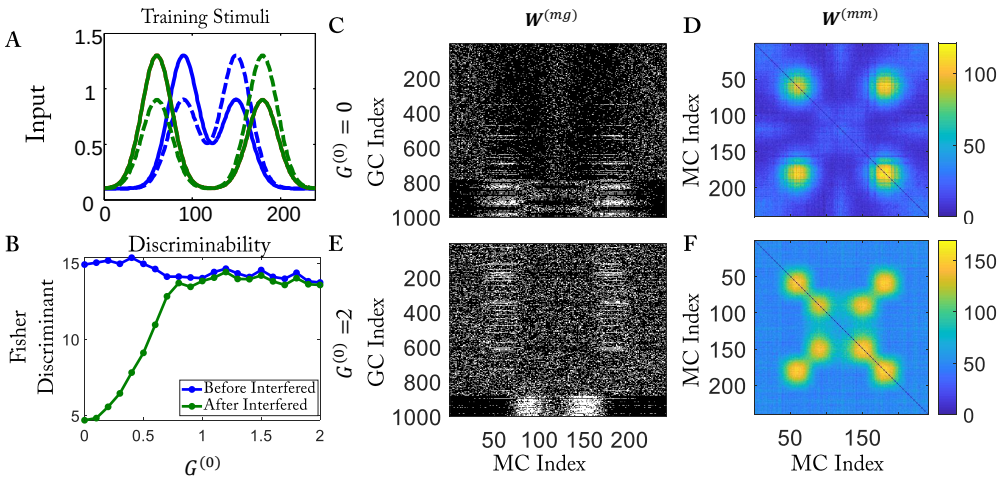

Figure 1.17. Increasing $G^{(0)}$ leads to less forgetting when trained with an interfering protocol. The results are generated by first training the model with one pair of hard stimuli (odor pair 1, blue curves in (A)), then by training with another pair of hard stimuli (odor pair 2, green curves in (A)), which is the same as the two pairs in Figure 1.10A before the switch 2. (A) Training stimuli. The model is first trained with odor pair 1, indicated by the two blue curves, which is the same as in Figure 1.10B, then the model is trained with odor pair 2, indicated by two green curves in, which is the same as in Figure 1.10C right figure. (B) The discriminability of odor pair 1 before and after the training with the interfering odor pair 2 (1.10C right figure) as a function of $G^{(0)}$. (C, D) Results for $G^{(0)} = 0$ after training with the odor pair 2. For $G^{(0)} = 0$, the model does not have the ability to remember: the connections between the mitral cells that are active by the odors in pair 1 have been removed (cool color in the center of $W^{(mm)}$) (C). (E, F) Results for $G^{(0)} = G^{(1)} = 2$ after training with a similar odor pair. For $G^{(0)} = G^{(1)}$, the model does not include an activity-dependent removal mechanism. In this case, previously learned network structure is intact, and the discriminability is not impaired (as in B). See discussion for more details.

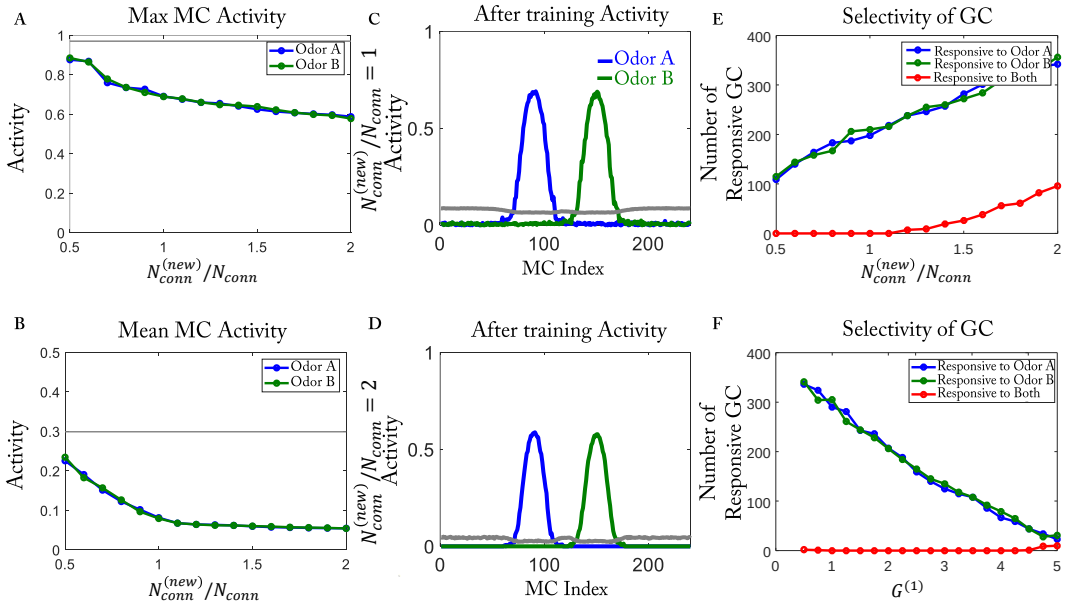

Figure 1.18. Selectivity of granule cells is influenced by the number of connections for each granule cell. The results here are generated by training with the easy stimuli in Figure 1.4A with a random initial network as in Figure 1.4E. (A, B) The maximal and mean mitral cell activity after training, respectively. (C, D) Mitral cell activity after training with $N_{conn}^{(new)}/N_{conn} = 1, 2$, respectively. (E) The selectivity of the granule cells is impaired by increasing the number of connection. A population of cells that respond to both odors emerges (indicated by the red line) when the number of connections is large. (F) Decreasing $G^{(1)}$ does not impair selectivity. The data is the same as in Figure 1.15.

Fifth, we test the effect of the number of connections for each granule cell. In this case, mitral cell activity is decreasing with increasing the number of connections on each granule cell (Figure 1.18 A, B). This is expected because more connections means each granule cell receives input from more mitral cells and it becomes easier

for its activity to surpass the threshold $G^{(1)}$. More activated granule cells with more synapses on each cell lead to an increase in inhibition. However, the increasing in the number of connections impairs the selectivity. Here, if the activity of a granule cell after training is bigger than $G^{(1)}$ for odor A or B, then the cell is called responsive to odor A or B. When the number of connections is large, a fraction of granule cells that responds to both odors emerges (Figure 1.18 E, red line), which is due to the lack of competition. This effect is not observed when varying $G^{(1)}$ (Figure 1.18F)

1.3.7. Realization of competition through a resource-dependent mechanism

To keep a Hebbian model stable, different compensatory processes can be imposed in addition to the homeosynaptic learning [32]. In our model, we use top-k competition because of its simplicity without identifying a specific biologically feasible mechanism. In this subsection, we discuss one possibility to realize this competition.

The idea behind the competition is that within a single neuron, resources used for the formation of synapses is limited. In a hippocampal CA1 neuron, stimulating neighboring spines leads to the shrinkage of the unstimulated spine [38]. An intuitive explanation of this phenomenon is that some resource is not plentiful enough within a cell. This idea has been discussed in the literature of synaptic plasticity [39]. Following this idea, we assume the activation function $\phi(G)$ now depends on the

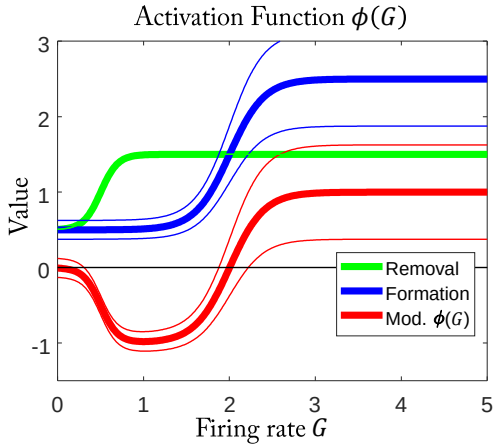

Figure 1.19. Diagram for the modified activation function $\phi(G)$. The modified activation function (red line) is the difference between the formation function (blue line) and the removal function (green curve). The black line is the original activation function. The thicker line indicates the situation when $P = P_0$. Here P_0 is the equilibrium point of the resource pool size. The thin lines indicates the changing of the activation function when $P \neq P_0$.

current resource pool size P. Further, we assume the activation function $\phi(G)$ (Figure 1.19, red curve) has an activity-dependent formation term ϕ_{form} (Figure 1.19, blue curve) and a removal term ϕ_{remove} (Figure 1.19, green curve):

$$\phi(\boldsymbol{r}_G, P) = \phi_{form}(\boldsymbol{r}_G, P) - \phi_{remove}(\boldsymbol{r}_G). \tag{1.9}$$

And the formation term depends on both activity of granule cell and the current size of the resource pool,

$$\phi_{form}(\boldsymbol{G}, P) = (\tanh(\kappa_{form}\ (\boldsymbol{G} - r_{form})) + 1 + R_0)\frac{P}{P_0}, \tag{1.10}$$

$$\phi_{rem}(\boldsymbol{G}) = (\tanh(\kappa_{rem}\ (\boldsymbol{G} - r_{rem})) + 1 + R_0) \tag{1.11}$$

where P_0 is the equilibrium resource pool size and the current resource pool depends on the number of synapses n as $P = P^{(all)} - n$ where $P^{(all)}$ is the total amount of the resource in the cell, which is assumed to have the same constant value for all the granule cells. For the initial condition, we have $P_0 = P^{(all)} - N_{conn}$. Similar to the original model, we can define $\tilde{G^{(0)}}, \tilde{G^{(1)}}, \tilde{G^{(0)}} < \tilde{G^{(1)}}$ as the intersection points of activation function and the X-axis.

In the experiments [11], mice are exposed to the odors only when they are on the training stage. When they are back in the cage, the training odors are absent and the activities of granule cells are supposed to be low. At the same time, the activation function $\phi(G)$ in the original model is kept as 0 when $G < G^{(0)}$, which means synapses are not formed or removed. Thus, according to the original model, the network does not evolve when the mice stay in the cage. However, in the modified model, the activation function $\phi(G)$ is not always 0. As a result, it is necessary to include trials during which only spontaneous activity is presented. Thus, in the current training protocol, we insert after every four training trials a rest trial during which the model

is only given spontaneous activity as input. During the rest trial, the synapses are spontaneously formed or removed depending on the size of the respective resource pool.

Now we discuss the changing of the activation function ϕ when the resource pool size is different. First, we consider the intersection of $\phi(G, P)$ and Y-axis. This point represents the dynamics of a granule cell when the activity of the granule cell is $G = 0$. When the resource pool is at the equilibrium point $P = P_0$, then $\phi(0, P) = 0$ and nothing changes; if the resource pool P is less than P_0, then $\phi(0, P) < 0$ and the synapses on the cell are randomly removed, which increases the resource pool and returns it back to the equilibrium point P_0,; if the pool is larger than P_0, then $\phi(0, P) > 0$ and new synapses are formed to randomly chosen mitral cells and also returns it to the equilibrium point P_0, (Figure 1.19). Thus, if the activity of a granule cell is 0, the size of the resource pool always goes to P_0 eventually. It also means that the number of the synapses on the granule cell goes to the initial value $n = N_{conn}$ eventually.

Second, we consider the impact on the turning point $\tilde{G^{(1)}}$ of the activation function. If the resource pool is depleted, then $\tilde{G^{(1)}}$ slides to the right and makes the corresponding granule cell harder to form new synapses, which indicates the competition between synapses on the cell is stronger; if the resource is plentiful, then $\tilde{G^{(1)}}$ moves to the left and make it easier to form new synapses (Figure 1.19), which

means the competition is weaker. This is a reminiscent of the sliding threshold in BCM model which studies synaptic weight plasticity [29]. However, the sliding here is caused by the changing of a limited resource instead of temporal average of the previous history.

Third, the change in threshold $\tilde{G^{(0)}}$ is accompanied by an opposite change in the turning point $\tilde{G^{(1)}}$ when the resource pool size changes, which may offer an explanation of why large $G^{(0)}$ may not be biologically feasible in the original model. In the modified model, when a granule cell makes a lot of connections, the resource pool is depleted and $\tilde{G^{(0)}}$ slides to the left, which is opposite to that $\tilde{G^{(1)}}$ slides to the right. As a result, the difference $|\tilde{G^{(1)}} - \tilde{G^{(0)}}|$ gets larger. This indicates the competition mechanism and the difference $|\tilde{G^{(1)}} - \tilde{G^{(0)}}|$ is correlated in the modified model. In the original model, the top-k competition means very strong competition when the number of connection reaches k: a new formed synapse is at the cost of removal of an existing synapse. In the modified model, a strong competition means the resource pool is depleted and the difference $|\tilde{G^{(1)}} - \tilde{G^{(0)}}|$ gets larger. When $\tilde{G^{(1)}}$ is fixed, this leads to a small $\tilde{G^{(0)}}$, which contradicts to a large $\tilde{G^{(0)}}$ in the original model.

Indeed, our modified model shows qualitatively similar results as we observed in our original model (Figure 1.20). The additional parameters we use in this section are listed in Table 1.2.

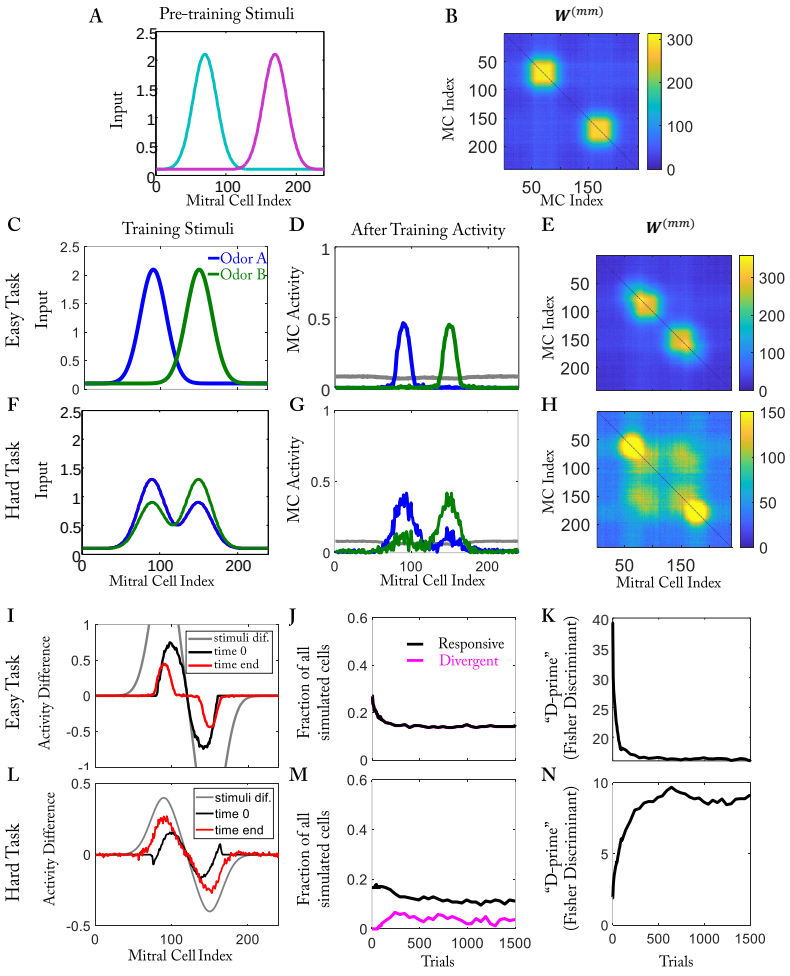

Figure 1.20. Realization of competition by a common resource pool. The results here are generated from the modified model by training with a hard or an easy task after pretraining with an easy task, which is the same protocol as in Figure 1.6 and in Figure 1.7. (A) The pretraining stimuli. (B) Effective connectivity $W^{(mm)}$ after pretraining. (C to E, I to K) Result of training with an easy task. (C) Training stimuli. (D) Mitral cell activity after training. (E) Effective connectivity $W^{(mm)}$ after training. (I) Activity difference of mitral cells before and after training. (J) fraction of responsive and divergent cells as a function of trials. (K) Fisher discriminant as a function of trials. (F to H, L to N) Result of training with a hard task. Figures are organized as (C to E, I to K). All the results are comparable with the original model.

κ_{form}	2.5	κ_{rem}	5
r_{form}	2	r_{rem}	1
R_0	0.8	P_0	20
Δt	1	γ	1.7e−3
τ_f	1	τ_f	1

Table 1.2. Table of parameters that used in resource-pool dependent competition.

1.4. Discussion

In the olfactory bulb, structural plasticity happens at a comparable timescale with learning, which raises the question what role structural plasticity plays in the learning process. In this study, we proposed a parsimonious Hebbian type model of structural plasticity. Our model offers a biologically plausible explanation of how a self-evolving reciprocal network within the olfactory bulb endows the animal with an enhanced power to discriminate odors and with a memory of the odors involved.

Even though our model is focused on the specific reciprocal connection between mitral and granule cells, which is not common in other brain areas, it suggests the advantages of structural plasticity in general. First, our model shows the potential to use a Hebbian-learning mechanism, which only requires local pre- and post-synaptic activity but not global optimization function, to train a system to acquire a specific function: decorrelating representations of similar input in our case, which helps to shed light on the link between local biophysical mechanisms and global cognitive functions. Second, after training with this Hebbian-type rule, the number of

synapses on each mitral cell and the response of each mitral cell have a positive correlation (Figure 1.4G, I), and the trained granule cells are selective to only one of the odor pairs. This result is reminiscent of the argument that this kind of connectivity can optimize inference from the neurons in the latter layer, which are selectively responsive to one of the contexts after training [40]. Third, our model shows how a structural plasticity model can maintain previously learned memory without an explicit history-dependent term. In another study focusing on the memory capacity of a network [41], they show that learning by activity-dependent structural plasticity, but not synaptic weight plasticity, avoids catastropic forgetting without the aid of history, while many artificial neural network models require an explicit history-dependent term [42].

In the adult rodent olfactory bulb, new granule cells keep integrating into the original network. The adult-born granule cells generated through neurogenesis have different features compared to early-born granule cells [43, 44]. It is shown that the adult-born cells are required for mice to learn the subtle differences between similar odors [13], and to detect the difference of perceptually close odorants after passive exposure to these odors in a complex environment [35, 43]. However, neurogenesis is absent in humans while humans do improve their ability to discriminate odors with experience [45], which raises the question of the necessity of neurogenesis for learning across different species. One of the features of adult-born granule cells is that they

are more plastic in structure than early-born granule cells [46]. This feature offers leverage for the adult-born granule cell population even though the total number is relatively small compared to the early-born granule cells. Another feature is that the network size increases overtime by having adult-born granule cells [47]. This growth of the network happens at a timescale of months, which is longer than the timescale considered in our study. Thus, we assume the size of network during learning is fixed. Still, the size of the network is different for different ages of the same animal in the experiment [47], and a network which is larger may has a stronger learning ability. In this study, we assumed adult-born granule cells and early-born granule cells all having the same level of structural plasticity while the total number of granule cells is fixed. We show that the structural plasticity is sufficient for the learning process and the results are robust over a wide range of the number of granule cells (Figure 1.13). As a result, our model underlines the importance of strong structural plasticity of adult-born neurons during learning, and also implies the irrelevance in the number of total inhibitory neurons. However, further research is needed to illustrate the effects of neurogenesis on rodents during learning.

In our model, we use a binary synaptic weight for the synapses instead of a continuous value. While non-binary changes in the weights of the reciprocal synapses have been observed, it is not yet understood what determines whether they are potentiated or depressed [15]. However, whether some learning rules for synaptic

weight plasticity can explain the same experimental observation [11] remains to be determined. To fully understand the learning related behavior in the olfactory bulb, further experimental and modeling studies are still required.

Our model also suggests the subnetwork structure (Figure 1.10D, E) is closely related to the memory function. In our model, the formed reciprocal connection increases the discriminability between the responses of similar stimuli. Forgetting the corresponding subnetwork structure also leads to the deterioration of the discriminability. Thus, our model suggests that the subnetwork structure may serve as a functional unit in the neuron network. Indeed, a modeling study also suggests that the formation of clusters that are functionally specialized for different cognitive processes can optimize the performance of the whole neuron network [48].

Another important question is that γ-rhythms can be generated from excitatory-inhibitory neuronal networks, of the type arising in our model by pyramidal interneuron gamma (PING) mechanism. γ-rhythms may play an important role in the communication between brain areas [49, 50], and it is observed in the olfactory bulb [51]. Further, the power of the γ-oscillation in the olfactory bulb is enhanced with task demand after learning [52], which implies that the learning process may impact the rhythms in the bulb. In this study, we show that by having structural plasticity, the resulting connectivity is different due to different training stimuli. It is unclear whether different configurations of connectivity would lead to the different levels of

power of γ-oscillation and to what extent. This will be an interesting question for the future.

Last, even though we recover our major results by replacing our top-k competition with a more biologically plausible resource-dependent competition, we want to point out that different brain areas may have different normalization mechanisms, which limits the generality of resource-dependent competition. Further, resource-dependent competition may be a very local mechanism, which cannot be detected from a few μm away as observed in hippocampal CA1 Neurons [38]. Thus, it is not likely that there is direct competition across different dendrites, even less likely across the whole neuron. In addition, heterosynaptic plasticity may be signal dependent rather than resource-dependent [38]. For these reasons, we leave open the question how to implement the normalization mechanism.

1.5. Conclusion

We have developed a Hebbian-type structural model which successfully explains the experimentally observed temporal evolution of the number of responsive and divergent cells as well as individual asymmetric mitral cell behavior. Further, the model explains why learning improves discriminability of difficult odors but deteriorates that of simple odors. We predict that the recalling of the previously learned task of the mice would be compromised if the animal was trained subsequently with similar odors. At last, we have pointed out potential questions for the future.

CHAPTER 2

Synchronization by uncorrelated noise: interacting rhythms in interconnected oscillator networks

2.1. Introduction

In the previous chapter, in our model, the subnetwork structure emerges after learning by activity-dependent plasticity in the olfactory bulb. We expect that γ-rhythms can be generated from the excitatory-inhibitory neuron network via the pyramidal interneuron gamma (PING) mechanism. How these γ-rhythms from different subnetworks interact is an interesting question. In this chapter, we study the synchronization conditions of the rhythms from interconnected subnetworks that generalized from the olfactory bulb.

Substantial progress has been made in the understanding the collective dynamics of oscillators that are coupled in a network; particularly the conditions for their synchronization are quite well understood [53, 54]. Synchronization is important in many technologically relevant systems (e.g. [55, 56, 57, 58]). It plays also a a central functional role in many biological systems like the heart [59] and the suprachiasmatic nucleus of the brain, which controls the circadian rhythm [60]. In the brain, coherent

activity of large ensembles of neurons manifests itself in macroscopically observable rhythms, which have been found in many brain regions [61]. Among them the widely observed γ-rhythm (30-100 Hz), which may play an important role in the communication between brain areas [62, 63, 64, 65, 66, 49, 50], has been studied particularly extensively [67, 68, 69, 70, 71, 72].

In synchronous regimes the collective oscillations constitute a rhythmic population activity of a whole network of oscillators and can be thought of as the dynamics of a single oscillator. Using a mean-field approach, this allows a first step towards the description of the interaction between multiple, interconnected such networks, which has, for instance, been used in ecological studies to capture the spatial interaction between different population oscillations [73]. Since such interconnected or modular networks are quite common [74, 75], the interaction between multiple networks, each supporting its own rhythm or collective oscillation, is of great interest.

For interconnected networks the stability of a globally synchronous state and its dependence on the connectivity within and between the networks has been studied using the master stability function [76, 77]. In the limit of weak coupling, which allows a phase description of the oscillators in terms of variants of the Kuramoto model, interconnected networks have been investigated for weak heterogeneity and weak noise [78, 79, 80, 81]. A feature shared by both these approaches is that the

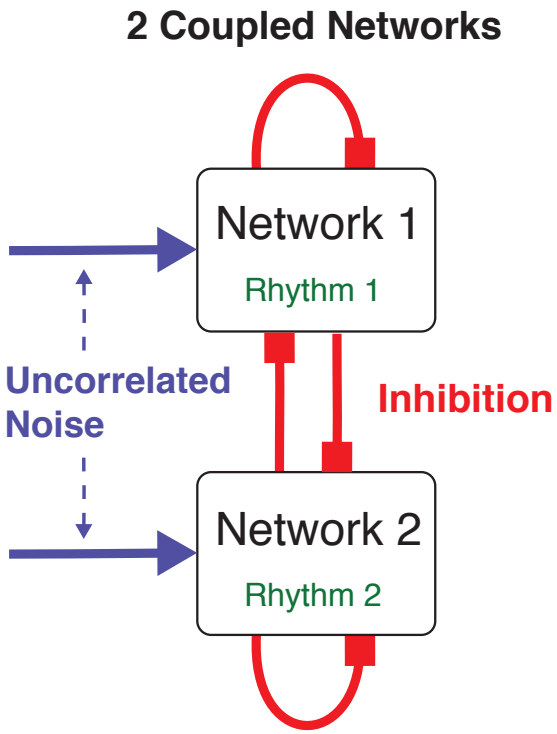

Figure 2.1. Interacting rhythms in two coupled oscillator networks. Each oscillator receives inhibition from the oscillators in its own network and from the oscillators in the other networks. In addition, each oscillator receives uncorrelated noisy input.

dynamics of the oscillators within each of the interconnected networks are quite homogeneous; in particular, all their oscillation amplitudes are very similar.

However, there are important, strong population rhythms in which the individual oscillation amplitudes fluctuate substantially and not all oscillators participate in each cycle of the collective oscillations. Neuronal γ-rhythms are a characteristic

example [67]. This raises the question whether the interaction between interconnected networks can couple sufficiently strongly to the internal degrees of freedom of the individual networks to modify the internal workings of the collective oscillations. Can this induce qualitative changes in the ability of the collective oscillations of the different networks to synchronize with each other or to an external pacemaker? In investigating these questions we are particularly motivated by the ubiquitous γ-rhythms [72] and their behavior-dependent coherence across different brain areas [65] as well as the simultaneous observation of multiple, different γ-rhythms in a single brain area that is presumably modularly organized [82, 83, 84, 9, 85].

Our key finding is that in interconnected networks (Fig.2.1) noise can synchronize the collective oscillations (population rhythms) that are generated by each of the oscillator networks. Importantly, the noise induces this synchronization even though it is uncorrelated between different oscillators and networks. This is in sharp contrast to the well-studied stochastic synchronization where the synchronization of different oscillators is due to the correlations in their input [86, 87, 88]. In that case the synchronization essentially reflects the transfer of correlations from the input to the output [89, 90, 91].

We identify the mechanism that drives the synchronization of the different rhythms as a network mechanism; it arises from the noise-driven phase heterogeneity of the oscillators within each network, which allows the inter-network coupling to suppress

the activity of a variable fraction of oscillators in a given cycle of the rhythm. Thus, desynchronization within each network enhances the mutual synchronizability of the networks.

This type of synchronization arises quite generally. We demonstrate it for networks comprised of various types of synaptically pulse-coupled neuronal oscillators (integrate-fire neurons, Morris-Lecar neurons of Type 1 and of Type 2) as well as for interconnected networks of relaxation oscillators that are coupled by rapid diffusion. Moreover, we find this synchronization in networks with all-to-all connectivity and in random networks.

2.2. Model

To illustrate the generality of our results we use three different types of oscillators as the nodes of the networks. Motivated by the relevance of the interaction of population rhythms for the communication between different brain areas [63, 61, 65, 50], we consider two different neuronal models: the single-component, discontinuous integrate-fire model and the continuous two-component Morris-Lecar model (type 1 and type 2). In both cases the interaction between the neurons is through synapses that provide pulse-like inhibition with a stereotypical wave form that is triggered when the presynaptic neuron surpasses a threshold. In the third model we go beyond the neuronal context and use relaxation oscillators that are

continuously coupled. They can be thought of as individual cells that interact via a rapidly diffusing substance, similar to quorum sensing [92, 93, 94].

2.2.1. Integrate-Fire Neurons

Each neuron i in network α is characterized by the depolarization $V_i(t)$, $i = 1 \dots N$, which satisfies

$$\tau \dot{V}_i = V_{rest} - V_i + R\, I_i^{(syn)}(t) + R\, I_i^{(ext)}(t). \tag{2.1}$$

To avoid cluttering the equations, we do not indicate the network α for each neuron in this section. Here $I_i^{(ext)}(t)$ denotes a noisy external excitatory input and $I_i^{(syn)}(t)$ the total synaptic current the neurons receives, which provides the coupling between the neurons within network α and across networks. The parameters τ and R are the membrane time constant and the membrane resistance, respectively. When $V_i(t)$ reaches the firing threshold V_θ, a spike is triggered and the voltage is reset to the reset voltage V_r. In integrate-fire neurons the oscillation frequency increases continuously from 0 when the spiking threshold is surpassed [95].

The synaptic currents are modeled as the difference of two exponentials, triggered by spikes of presynaptic neurons j at times $t_j^{(k)}$,

$$I_i^{(syn)} = \frac{g_{syn}}{R} \left(A_i^{(2)} - A_i^{(1)} \right) (V_{rev} - V_i)\,, \tag{2.2}$$

with

$$\dot{A}_i^{(1,2)} = -\frac{A_i^{(1,2)}}{\tau_{1,2}} + \sum_{j=1}^{N} \sum_k W_{ij}\, \delta\left(t - t_j^{(k)} - \tau_d\right). \tag{2.3}$$

Here g_{syn} denotes the dimensionless synaptic strength and τ_d the synaptic delay. Being conductance-based, the synaptic current depends on the post-synaptic voltage V_i relative to the reversal potential V_{rev}, which is strongly negative for the inhibitory synapses considered here. The connectivity matrix is denoted by $\mathbf{W}$ with its non-zero elements given by $W_{ij} = 1$ if neuron i and j belong to the same network, while $W_{ij} = \gamma_0 < 1$ if they belong to different networks.

The external input of each neuron i is modeled as an independent Poisson-train of δ-spikes at times $t_{ik}^{(ext)}$,

$$I_i^{(ext)}(t) = \frac{V_\theta - V_r}{R} \Delta v_i \; \tau \sum_k \delta(t - t_{ik}^{(ext)}). \tag{2.4}$$

Thus, the noisy external inputs to different neurons are uncorrelated. The dimensionless input strengths Δv_i are scaled such that for $\Delta v_i = 1$ a single pre-synaptic input spike is sufficient to trigger a spike in the post-synaptic neuron. The input strengths are equal for all neurons within a network, but differ between networks: $\Delta v_i = \Delta v^{(\alpha)}$ for neurons in network α. The input ratio $\rho^{(\alpha)} \equiv \Delta v^{(\alpha)}/\Delta v^{(1)}$ determines the frequency ratio of the rhythms of the uncoupled networks.

Instead of the spike rates $\lambda^{(\alpha)}$ of the Poisson trains and the strengths $\Delta v^{(\alpha)}$ we use the mean input $\mu^{(\alpha)} = \lambda^{(\alpha)}\Delta v^{(\alpha)}$ and its variance $\sigma^2 = \lambda^{(\alpha)}(\Delta v^{(\alpha)})^2$ as independent parameters. Thus, the noise strength characterized by σ^2 is the same for all neurons in all networks. The spike rates used in this paper are of the order $\mathcal{O}(10,000\ \mathrm{s}^{-1})$, which corresponds to each neuron in the network receiving external input from $\mathcal{O}(200)$ neurons, each firing at a rate of $\mathcal{O}(50\ \mathrm{s}^{-1})$.

2.2.2. Morris-Lecar Neurons

For weak coupling the synchronization between individual neuronal oscillators depends strongly on their phase-response curve, i.e. on the change in their oscillation phase in response to a small δ-spike input. To go beyond integrate-fire neurons, which have a type-1 phase-response curve, we also investigate synchronization in Morris-Lecar neurons, which are of type 1 or type 2 depending on the parameter values. They are described by a voltage V and a gating variable n for the potassium conductance,

$$\begin{aligned} C_m\dot{V}_i &= -g_l\,(V_i - V_{leak}) - g_{Ca}\,m_\infty(V_i)\;(V_i - V_{Ca}) \\ &\quad -g_K\,n(V_i)\,(V_i - V_K) \\ &\quad +\sum_j W_{ij} I_{ij}^{(syn)} + I_i^{(ext)}, \qquad (2.5) \\ \tau_n(V_i)\,\dot{n}_i &= n_\infty(V_i) - n_i. \qquad (2.6) \end{aligned}$$

Here

$$m_\infty(V) = \frac{1}{2}(1 + \tanh \frac{V - V_{\theta_m}}{V_{s_m}}), \tag{2.7}$$

$$n_\infty(V) = \frac{1}{2}(1 + \tanh \frac{V - V_{\theta_n}}{V_{s_n}}), \tag{2.8}$$

$$\tau_n(V) = \frac{1}{\phi \cosh \frac{V - V_{\theta_n}}{2V_{s_n}}}. \tag{2.9}$$

As for the IF-neurons, the external current $I_i^{(ext)}$ consists of Poisson spike trains with mean μ and variance σ^2 (cf. equation (2.4)) and the synaptic currents are given by equation (2.2).

We use here $C_m = 20\mu\text{F/cm}^2$, $g_{Ca} = 4\text{ms/cm}^2$,$g_K = 8\text{ms/cm}^2$, $g_L = 2\text{ms/cm}^2$, $\phi = 1/15\text{s}^{-1}$, $V_{Ca} = 120\text{mV}$, $V_K = -80mV$, $V_L = -60\text{mV}$, $V_{\theta_m} = -1.2\text{mV}$, $V_{s_m} = 18\text{mV}$, $V_{s_n} = 17.4\text{mV}$. For $V_{\theta_n} = 12\text{mV}$ these equations describe then a type-1 neuron, while for $V_{\theta_n} = 2\text{mV}$ one obtains a type-2 neuron [96]. The synaptic parameters are $\gamma_{syn} = 0.0084$, $\tau_1 = 4\text{ms}$, $\tau_2 = 5\text{ms}$.

2.2.3. Relaxation Oscillators

To go beyond the coupling by stereotypical pulses that is characteristic for neuronal systems, we consider a minimal model of relaxation oscillators that communicate through a rapidly diffusing substance S, reminiscent of the quorum sensing used in

models for the synchronization of genetic, cellular oscillators [93, 94]. Each oscillator i in network α is described by

$$\dot{x}_i = x_i - x_i^3 - y_i\left(x_i - x_0^{(1)}\right) + \xi_{xi}, \tag{2.10}$$

$$\dot{y}_i = \epsilon\left(-y_i + \beta x_i + \gamma_i + \mu S_i\right) + \xi_{yi}, \tag{2.11}$$

$$\dot{S}_i = -\lambda S_i + \nu\left(x_i - x_0^{(2)}\right) \tag{2.12}$$

$$-\kappa_{local}\left(S_i - S_{local}\right) - \kappa_{global}\left(S_i - S_{global}\right) + \xi_{Si}.$$

Here x, y, and S can be thought of as deviations in the concentrations of the respective substances from a mean value. S_{local} is the average of S_i within network α and S_{global} is the average of S_i across the oscillators of all networks. The strength of the coupling within each network is given by κ_{local}, whereas the global interaction among all oscillators is given by κ_{global}. Thus, within and across the networks the interaction of the oscillators is all-to-all. Each component of each oscillator is driven by Gaussian white noise $\xi_{x,y,z}$ with the same variance σ^2; the noise is δ-correlated in time and uncorrelated across components and oscillators.

The dynamics of this model are shown in Fig.2.2 for an individual oscillator. The reactant S responsible for the interaction is produced for $x_i > x_0^{(2)}$. Thus, its amount depends on the waveform of the oscillation, particularly on its amplitude.

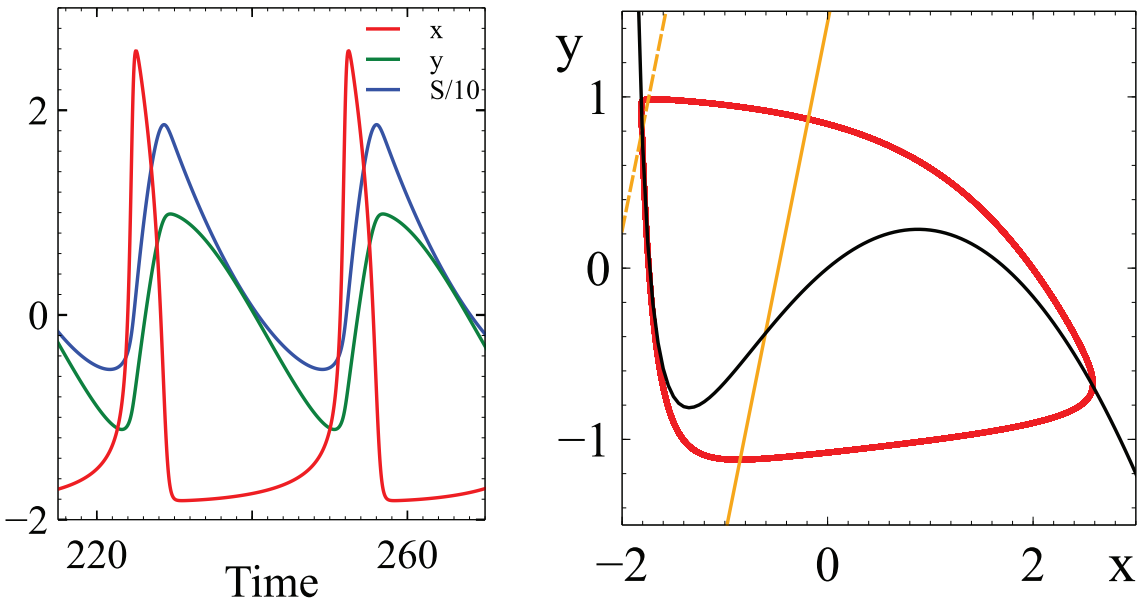

Figure 2.2. In the relaxation oscillator (equations (2.10,2.11,2.12)) the coupling field S reflects the oscillation wave form and affects the stability of the fixed point. a) Temporal evolution of x, y, and S for the relaxation oscillator and b) corresponding projection onto the (x, y)-phase plane. Black: x-nullcline, gold: y-nullclines corresponding to the minimal (solid) and the maximal (dashed) value of S along the limit cycle. Parameters: $\epsilon = 0.05$, $\beta = 3$, $\mu = 0.2$, $\lambda = 0.05$, $\nu = 2$, $\kappa_{local} = 5$, $\kappa_{global} = 0.15$, $x_0^{(1)} = -2$, $x_0^{(2)} = -1.2$, $\gamma = 2.5$, $\sigma = 0$.

An increase in S shifts the y-nullcline to the left, shifting the fixed point and reducing the oscillation frequency. For sufficiently large S the fixed point becomes stable.

2.2.4. Order Parameters

In the IF-model the voltage trace $V(t)$ does not include the action potential (spike) itself. When taking the mean across the network to obtain $\bar{V}^{(\alpha)}$, we therefore add

a spike of size $V_{spike} = 45\text{mV}$ to the voltage in the time step when V reaches the threshold V_θ. This enhances the diagnostics in terms of the order parameter. To characterize the degree to which the different LFPs $\bar{V}^{(\alpha)}$ are synchronized we use the temporal average of the order parameter r_{global} defined as

$$r_{global}(t)\, e^{i\psi_{global}(t)} = \frac{1}{\mathcal{N}} \sum_{\alpha=1}^{\mathcal{N}} e^{i\phi^{(\alpha)}(t)}. \tag{2.13}$$

Here the phase $\phi^{(\alpha)}$ is the argument of the analytic signal of $\bar{V}^{(\alpha)}$, which is obtained via a Hilbert transform. Analogously, the local order parameter

$$r^{(\alpha)}_{local}(t)\, e^{i\psi^{(\alpha)}_{local}(t)} = \frac{1}{N_\alpha} \sum_{k=1}^{N_\alpha} e^{i\phi^{(\alpha)}_k(t)} \tag{2.14}$$

measures the synchronization within network α. Here $\phi^{(\alpha)}_k(t)$ is the argument of the analytic signal of oscillator k in network α.

For the networks of relaxation oscillators we use an overall order parameter that is based on the argument $\phi^{(\alpha)}$ of the analytic signal of the averages $\bar{x}^{(\alpha)}(t) \equiv \frac{1}{N_\alpha} \sum_{k=1}^{N_\alpha} x^{(\alpha)}_k(t)$ within each network α. The distribution function $\mathcal{P}(\phi^{(\alpha)})$, when sampled uniformly in time, turns out to be strongly non-uniform. This reflects the fact that in these relaxation oscillations the oscillators - and also the collective oscillations - spend much more time in specific parts of phase space and $\phi^{(\alpha)}$ evolves quite nonlinearly in time. Because of this bias in $\mathcal{P}(\phi^{(\alpha)})$ the unweighted average $\mathcal{N}^{-1} \sum_{\alpha=1}^{\mathcal{N}} e^{i\phi^{(\alpha)}(t)}$ across the $\mathcal{N}$ interconnected networks does not vanish even if the

averages $\bar{x}^{(\alpha)}(t)$ of all of the networks are completely uncorrelated and $\mathcal{N}$ is large. We therefore define the order parameter via the weighted average

$$r_{global}(t)\, e^{i\psi_{global}(t)} = \frac{1}{\mathcal{N}} \sum_{\alpha=1}^{\mathcal{N}} \frac{1}{\mathcal{P}\left(\phi^{(\alpha)}(t)\right)}\, e^{i\phi^{(\alpha)}(t)}.$$

We approximate $\mathcal{P}(\phi^{(\alpha)}(t))$ using a 6^{th}-order polynomial fit to the histogram of $\phi^{(\alpha)}$. With this correction the order parameter is appropriately very small when the collective oscillations are uncorrelated. In principle, the same correction should be used for the order parameters $r_{local}^{(\alpha)}$ of the individual networks. However, for the strong order found within the individual networks introducing the weights has only little impact. We therefore forgo this slight improvement, which requires substantial computational effort, and use the unweighted local order parameter $r_{local}^{(\alpha)}$ as defined in equation (2.14) based on the analytic signal of $x_k^{(\alpha)}(t)$.

2.3. Results

We investigate the interaction of population rhythms in interconnected networks of synaptically coupled integrate-fire (IF) neurons, of synaptically coupled Morris-Lecar neurons, and of diffusively coupled relaxation oscillators. The network connectivities are taken to be either all-to-all or random, with an effective coupling strength that is stronger within each network than across networks. In all of the cases the individual oscillators (neurons) receive noisy inputs whose means are the same within

each network, but differ across networks. Importantly, the noisy inputs to different neurons belonging to the same or to different networks are uncorrelated.

2.3.1. Noise-Induced Synchronization of IF-Networks

To illustrate the synchronization of populations by uncorrelated noise we first show results for a large number ($\mathcal{N} = 100$) of interconnected networks of integrate-fire neurons. While for brain rhythms the interaction of only a few rhythms is expected to be particularly relevant, key elements of the synchronization can be visualized and characterized better using many networks, because they allow not only the definition of an order parameter r_{local} for the within-network synchrony, but also of a global order parameter r_{global} for the synchrony across networks (cf. Eqs.(2.13,2.14)).

Thus, each row in Fig.2.3A1,2 shows the collective oscillation of one of the networks. The input to each neuron consists of an independent Poisson spike train. The mean spike rate of these spike trains and with it the natural frequency of each neuron is equal for all neurons in a network but decreases with increasing index α of the network (for clarity only 25 networks are shown). We characterize the noise in each spike train by the variance σ^2 of its spike rate. Each neuron in network α receives strong inhibition from all $N_\alpha = 100$ neurons in the same network and weaker inhibition from all neurons in the other networks. Due to the strong within-network

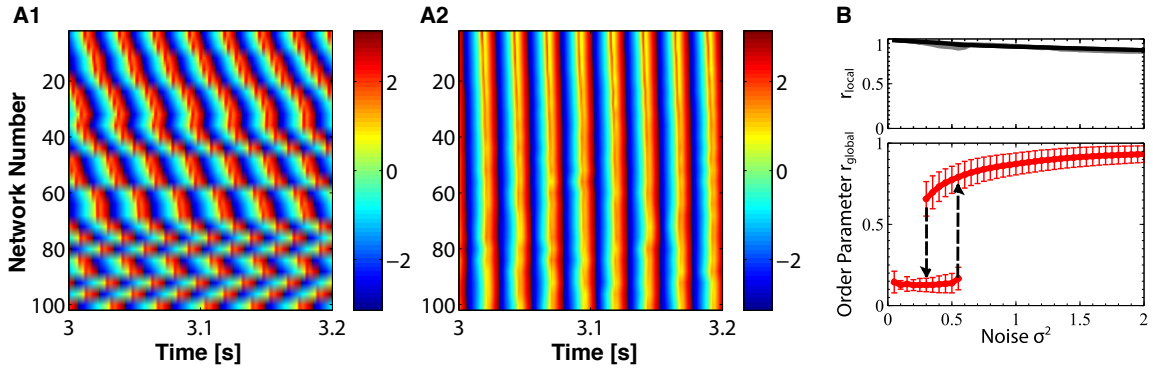

Figure 2.3. Increasing the uncorrelated noise in the inputs to the individual neurons synchronizes the population rhythms of interconnected networks of IF-neurons. A: Temporal evolution of the phases $\phi^{(\alpha)}(t)$ of the population rhythms $\bar{V}^{(\alpha)}(t)$ of the $\mathcal{N} = 100$ networks. A1: For weak noise ($\sigma^2 = 0.04\text{s}^{-1}$) the rhythms are not synchronized; shown is $\phi^{(\alpha)}(t)$ for $\alpha = 4, 8, 12, \ldots 100$. A2: Strong noise ($\sigma^2 = 2\text{s}^{-1}$) synchronizes the rhythms. B: The time-averaged order parameter r_{global} of the interconnected networks (lower panel) increases hysteretically with increasing strength of the uncorrelated noise (error bars denote standard deviation). The order parameters $r^{(\alpha)}$ of the individual networks (upper panel) decrease with noise, time-averaged $r^{(1)}$ and $r^{(100)}$ are shown. Parameters: $\gamma_0 = 0.0065$, $g_{syn} = 0.021$, $\mu = 200\text{s}^{-1}$, $\tau = 20\text{ms}$, $\tau_1 = 4ms$, $\tau_2 = 5\text{ms}$, $\tau_d = 2\text{ms}$, $V_{rest} = -55\text{mV}$, $V_\theta = -45\text{mV}$, $V_r = -65\text{mV}$, $V_{rev} = -85\text{mV}$, $\rho^{(\alpha)} = 1 - 0.25\,\frac{\alpha}{\mathcal{N}}$. The parameters γ_0 and g_{syn} have been scaled so that the overall conductances of the connections within and across the networks correspond to those in the 2-network case discussed below (Fig.2.5).

inhibition the neurons within each network synchronize, resulting in a collective oscillation (population rhythm) that corresponds to an interneuronal network γ-rhythm (ING) [97, 98, 71, 99]. We characterize the rhythm in network α via the mean $\bar{V}^{(\alpha)}$ of the voltage V_i across all neurons i of network α, using it as a proxy for the local

field potential (LFP) of network α that would typically be measured experimentally. To characterize the degree to which the different LFPs $\bar{V}^{(\alpha)}$ are synchronized we use the temporal average of the order parameter $r_{global}(t)$, which is based on the analytic signal of $\bar{V}^{(\alpha)}$ (cf. Eqs. (2.2.4)). Analogously, we use a local order parameter $r^{(\alpha)}_{local}(t)$ to quantify the synchronization within network α, which is based on the analytic signal of the individual oscillators in network α (Eqs.(2.13,2.14)).

Without or with very weak noise σ^2 the LFPs $\bar{V}^{(\alpha)}$ of the different networks do not synchronize (Fig.2.3A1); instead they oscillate at different frequencies reflecting the different mean inputs $\rho^{(\alpha)}$ that the neurons in the different networks receive, $\rho^{(\alpha)} = \rho_{max} - \frac{\alpha}{N}(\rho_{max} - \rho_{min})$ with $\rho_{max} = 1$ and $\rho_{min} = 0.75$. Correspondingly, the global order parameter r_{global} is small (Fig.2.3B). However, as the noise is increased above a critical value $\sigma^2_{c+} = 0.44\text{s}^{-1}$ the system undergoes a discontinuous transition reflected in a large jump of the order parameter r_{global}. The LFPs of most networks are now synchronized (Fig.2.3A2). If the noise amplitude is now reduced adiabatically, synchronization across the networks persists up to a lower value $\sigma^2_{c-} = 0.24\text{s}^{-1}$, revealing hysteresis. Why does this network of oscillator networks become more coherent when it is exposed to stronger uncorrelated noise?

A characteristic feature of the synchronization mechanism is that noise allows the slower network to speed up, but it does not slow down the faster network (cf. Fig. 2.5). This is also seen in the spectra of the large interconnected network of Fig.2.3.

For low noise the spectrum of each network is broad (Fig.2.4 top panels). However, in the ordered regime at larger noise, the frequencies of most networks has increased to the value of the fastest network.

To identify the mechanism by which uncorrelated noise can synchronize interconnected networks of oscillators we reduce the complexity of the system in two steps. We first consider two coupled networks and then the even simpler case in which network 2 is exposed to strictly periodic inhibition. We present here the results for 2 networks with all-to-all coupling.

Consistent with our results for many interconnected networks (Fig.2.3), increasing the strength σ of the uncorrelated noise - at fixed coupling strength - can enhance the synchrony of the two rhythms of the two coupled networks (Fig.2.5). For vanishing and very weak noise the two rhythms exhibit 2:3 phase-locking, as is apparent from the attractor, here represented in terms of the LFPs $\bar{V}^{(\alpha)}$ of the two networks (Fig.2.5B6 for $\rho^{(2)} = 0.83$), and the corresponding LFP-spectra (Fig.2.5B3). In this regime the two networks behave like two individual oscillators. For somewhat larger noise the attractor becomes smeared out and the spectra suggest a transition to noisy 1:2 phase locking (Fig.2.5B2,5). Strikingly, a further increase in noise strength 'cleans up' the attractor (Fig.2.5B4). This is reflected in a strong reduction of the low-frequency components of the Fourier spectra, which for sufficiently strong noise reveal 1:1 phase locking, i.e. synchronization of the two rhythms (Fig.2.5B1). More

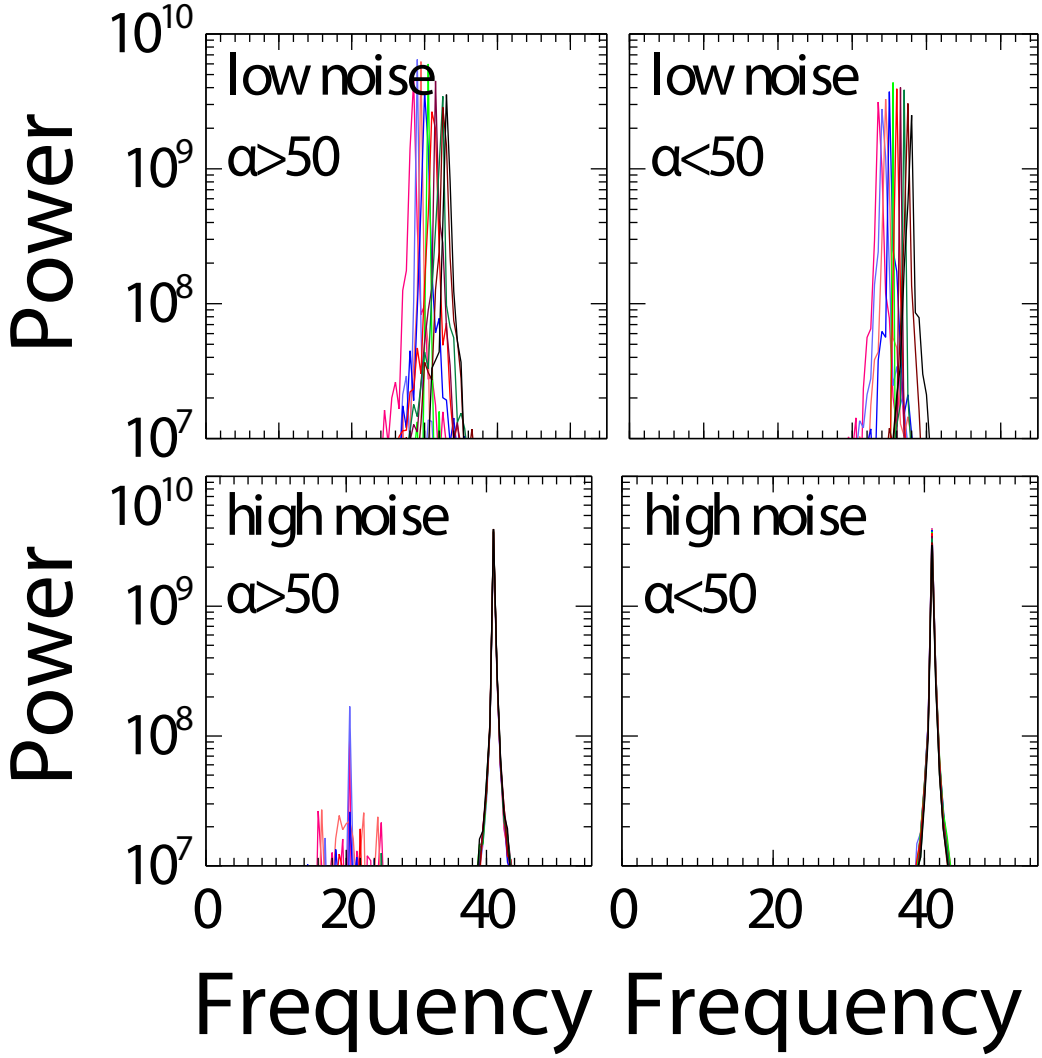

Figure 2.4. Uncorrelated noise synchronizes the networks at the frequency of the fastest network. Upper panels: for low noise, $\sigma^2 = 0.04\text{s}^{-1}$, the networks are not synchronized. Fourier spectra of the LFPs $\bar{V}^{(\alpha)}$ of 25 of the 100 interconnected IF-networks shown in Fig.2.3 vary significantly in frequency. Lower panels: For stronger noise, $\sigma^2 = 2\text{s}^{-1}$, all networks are essentially synchronized, showing only a weak subharmonic component (note the logarithmic scale). Left (right) panels show the spectra for the networks with weaker ($\alpha > \mathcal{N}/2$) and stronger ($\alpha \leq \mathcal{N}/2$) injected current. Parameters as in Fig.2.3.

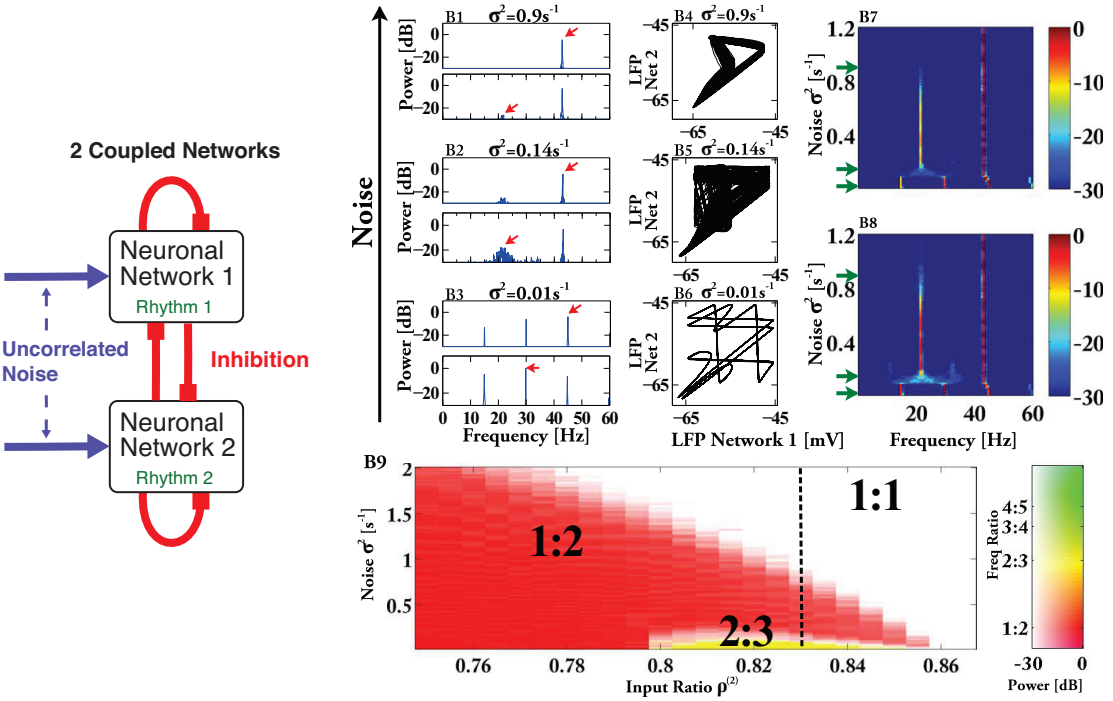

Figure 2.5. Uncorrelated noise synchronizes population rhythms of two coupled networks. A) Sketch of the two coupled networks. B) (B1-3) Fourier spectra of LFP $\bar{V}^{(1)}$ (upper panel) and LFP $\bar{V}^{(2)}$ (lower panel) of network 1 and 2, respectively, on a logarithmic scale for $\rho^{(2)} = 0.83$ and different noise strengths ($\sigma^2 = 0.9\text{s}^{-1}$, $\sigma^2 = 0.14\text{s}^{-1}$, $\sigma^2 = 0.01\text{s}^{-1}$). (B4-6) attractors for the corresponding values of σ^2. (B7) Spectral power for network 1 as a function of noise and frequency for $\rho^{(2)} = 0.83$. Green arrows indicate noise values in (B1-3). (B8) as (B7) for network 2. (B9) Phase diagram. Color hue and saturation indicate frequency ratio and logarithmic power ratio of the characteristic Fourier modes (marked with red arrows in panels B2,3), respectively. Synchronization is obtained in the white region labeled 1:1. Parameters: $N_\alpha = 500$, $\tau = 20\text{ms}$, $\tau_1 = 4ms$, $\tau_2 = 5\text{ms}$, $\tau_d = 2\text{ms}$, $V_{rest} = -55\text{mV}$, $V_\theta = -45\text{mV}$, $V_r = -65\text{mV}$, $V_{rev} = -85\text{mV}$, $g_{syn} = 0.0042$, $\gamma_0 = 0.64$, $\mu = 200s^{-1}$.

detailed simulations show that the spectral peak characterizing the 1:2 phase locking decreases to very small values smoothly (Fig.2.5B7,8; [1]), indicating that synchrony is reached by undergoing a continuous (super-critical) period-doubling bifurcation in reverse (cf. Fig.2.11 below).

The frequency ratio of the two rhythms in the absence of noise depends on the ratio $\rho^{(2)}$ of the mean inputs $\mu^{(\alpha)}$ of the two networks. Delineating the different phase-locked states as a function of $\rho^{(2)}$ and of the noise strength σ leads to domains akin to Arnold tongues in which, strikingly, the coupling strength is replaced by the noise strength as the second control parameter. In Fig.2.5B9 the color hue indicates the ratio $\omega_2 : \omega_1$, where ω_1 is the frequency of the dominant spectral peak of network 1 and ω_2 is the frequency of the dominant peak of network 2 that satisfies $\omega_2 < \omega_1$ (arrows in Figs.2.5B2,3). The saturation of the color gives the corresponding ratio $A^2(\omega_2)/A^2(\omega_1)$ of the amplitudes of the peaks on a logarithmic scale. Thus, over quite some range in the input ratio $\rho^{(2)}$ noise induces synchrony (white region labeled 1:1) via a continuous period-doubling bifurcation, as signified by the fading-away of $A^2(\omega_2)/A^2(\omega_1)$ with $\omega_2 : \omega_1 = 1 : 2$. Depending on $\rho^{(2)}$, the 1:2 phase-locked state can arise directly at vanishing noise or via a transition from the 2:3 tongue.

[1]For clarity the frequency resolution has been reduced in Fig.2.5B7,8; for each bin the maximal value of the power in that bin is shown.

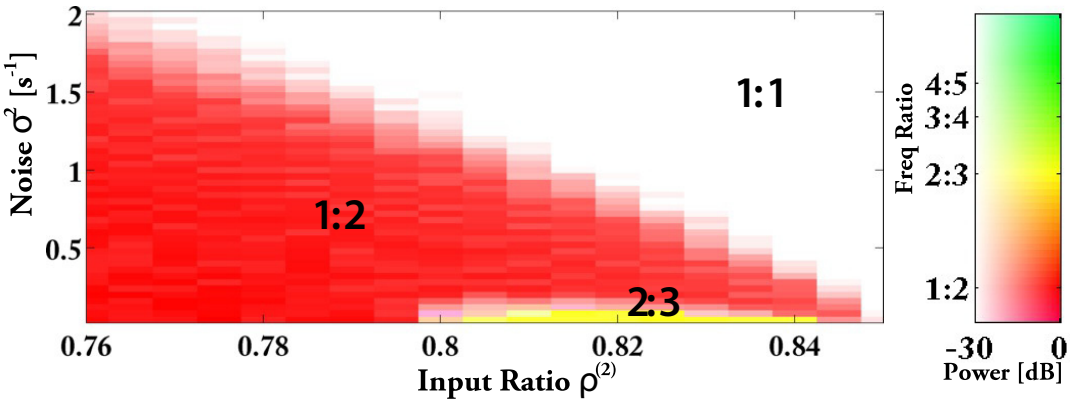

Figure 2.6. Uncorrelated noise synchronizes population rhythms of two coupled IF-networks with random connectivity. Phase diagram showing transitions between different phase-locked and synchronized states as a function of noise and input ratio. Color hue and saturation indicate frequency ratio and logarithmic power ratio of the dominant Fourier modes (cf. Fig.2.5). Parameters: $N_\alpha = 500$, $\epsilon_1 = 0.56$, $\epsilon_2 = 0.24$, $\tau = 20$ms, $\tau_1 = 4ms$, $\tau_2 = 5$ms, $\tau_d = 2$ms, $V_{rest} = -55$mV, $V_\theta = -45$mV, $V_r = -65$mV, $V_{rev} = -85$mV, $g_{syn} = 0.015$, $\gamma_0 = 1.5$, $\mu = 200s^{-1}$.

To demonstrate the robustness of the synchronization with respect to changes in the connectivity we also consider the impact of uncorrelated noise on two coupled IF-networks with random connectivity.

Each oscillator receives $\epsilon_1 N_\alpha$ random inhibitory connections from its own network and a smaller number $\epsilon_2 N_\alpha$ of random inhibitory connections from the other network. Thus, all oscillators have the same in-degree, but not the same out-degree. We have avoided the heterogeneity that would be associated with variable in-degree in order to focus on the synchronization by temporal noise. As shown in Fig.2.6, the overall

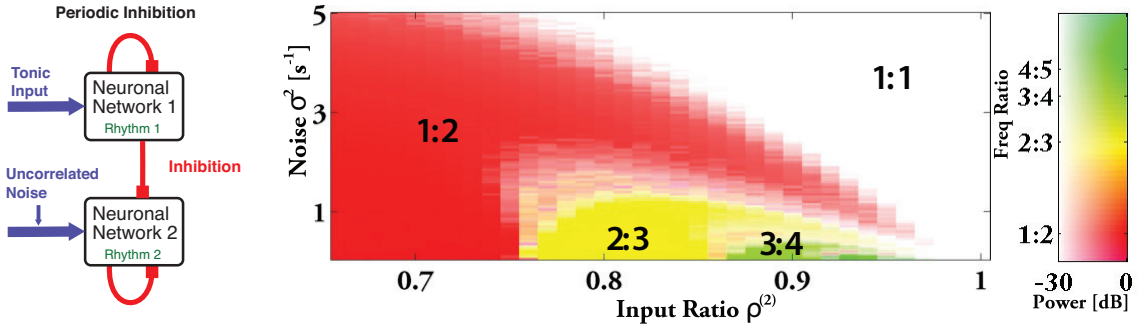

Figure 2.7. Noise increases the frequency range of entrainment of periodically inhibited rhythm. A) of the periodically forced single network 2. B) Phase diagram for a single network with periodic inhibition. Each neuron in the network receives uncorrelated noise, which synchronizes the rhythm with the forcing in the white region marked 1:1. Parameters and colors as in Fig.2.5B9.

behavior of these random networks is very similar to the networks with all-to-all coupling with the noise synchronizing the two networks (Fig.2.6).

Analogous to the case of the network of networks (Fig.2.3), where in the synchronized state the overall frequency of the system is close to that of the fastest network (Fig.2.4), the two networks synchronize at the frequency of the faster network. This suggests that the mechanism does not require the mutual interaction of the two networks, but can also operate in a single network that is exposed to strictly periodic inhibition. We implement periodic forcing by giving tonic input to network 1 and removing the inhibition it receives from network 2 (Fig.2.7A). Network 1 therefore acts as a pacemaker for network 2, a situation that is, for instance, relevant for circadian rhythms with the dark-light schedule functioning as pacemaker. Indeed,

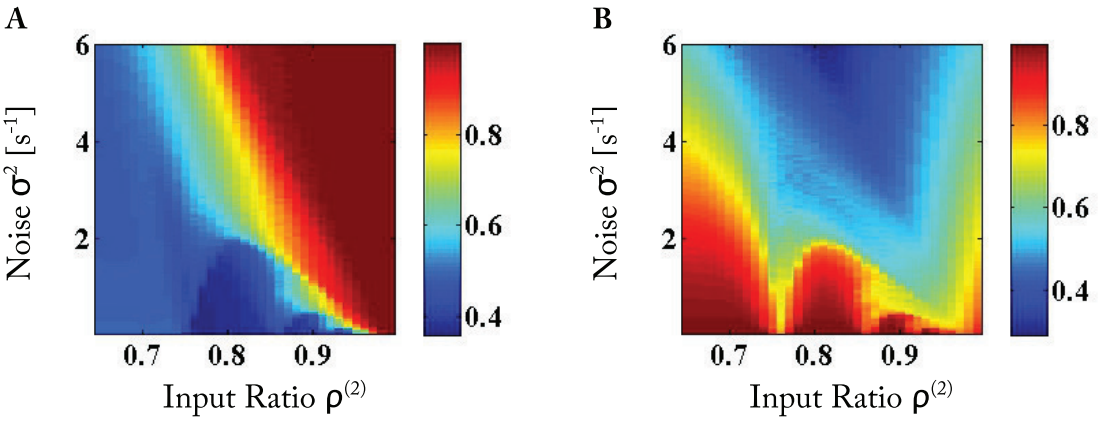

Figure 2.8. Correlations between rhythms and between individual oscillators respond oppositely to noise. A) The correlation $\langle \bar{V}^{(1)}, \bar{V}^{(2)} \rangle$ between the LFP of network 2 and the periodic inhibition increases with increasing noise (cf. Fig.2.7). B) The average of the equal-time correlations $\langle V_j^{(2)}, V_k^{(2)} \rangle$ between individual neurons j and k in network 2 decreases monotonically with increasing noise strength. Parameters as in Fig.2.7.

depending on $\rho^{(2)}$, as the noise is increased the periodically inhibited single network 2 undergoes transitions between different phase-locked states and eventually reaches the synchronized 1 : 1-state via a continuous period-doubling bifurcation (Fig.2.7B). In parallel, the correlation between the rhythm in network 2 and the periodic forcing increases (Fig.2.8A). Fig.2.7B shows also that the frequency range over which the rhythm can be entrained 1:1 by the external forcing increases substantially with noise. Thus, noise enhances the synchronizability of the rhythm.

The synchronization of the population rhythms does not imply the synchronization of individual oscillators. To demonstrate this we measure the equal-time correlation between the voltages of the individual neurons within network 2 ($\langle V_j^{(2)}, V_k^{(2)} \rangle$) and compare it with the correlation between the LFP of network 2 and the periodic forcing ($\langle \bar{V}^{(2)}, \bar{V}^{(1)} \rangle$). For the latter we determine the phase shift between the two signals from the difference in the phases of their dominant Fourier modes and plot in Fig.2.8A the correlation for that delay as a function of the noise and the input ratio $\rho^{(2)}$. Mirroring the phase diagram of the periodically forced network (Fig.2.7) the correlation between the LFP of network 2 and the periodic forcing increases with noise. However, the voltage correlations between the individual neurons within network 2 decrease monotonically with increasing noise strength (Fig.2.8B), reflecting the decrease in the local order parameters in Fig.2.3B.

2.3.2. Within-Network Desynchronization Enhances Synchronizability of Networks

Insight into the synchronization mechanism is gained from the temporal evolution of the voltage distribution function of the neurons in the periodically forced network 2 (Fig.2.9, cf. Fig.2.7). The tonically driven neurons in network 1, which provides the periodic forcing, reach the threshold $V_\theta = -45\text{mV}$ at the times marked by double-arrowed lines; they spike and their voltage is reset to $V_r = -65\text{mV}$. At the dashed

line the ensuing delayed inhibition reaches network 2. Even though all neurons within network 2 receive the same mean external input, the uncorrelated noise in that input reduces their correlation (Fig.2.8B) and induces a spread in their voltage. While that spread is not large in Fig.2.9, it is sufficient to split the neuron population into two groups: a faster group that has already spiked when the inhibition arrives and a slower, lagging group that is kept from spiking by the strong inhibition. In contrast to the instantaneous voltage reset to V_r associated with spiking (red arrow), the voltage of the slower group of neurons decreases smoothly (green arrow). Eventually, due to the strong inhibition originating from the spiking neurons in network 2 the two groups of neurons in network 2 merge again before the cycle resumes.

Importantly, the self-inhibition of network 2 delays the time to its next spiking volley. Consequently, when the inhibition from network 1 keeps the lagging neurons in network 2 from spiking, the total self-inhibition within network 2 is reduced, speeding up its rhythm in that cycle. If network 2 catches up, more of its neurons escape the inhibition by network 1 and spike (cf. cycle starting at θ_{n+1} in Fig.2.9), increasing self-inhibition of network 2 and slowing down its rhythm. Thus, even though the inhibition from network 1 briefly delays each neuron in network 2, overall it speeds up the rhythm of network 2 in a phase-dependent fashion. This provides a stabilizing feedback and allows the network to adjust its population frequency over a wide range.

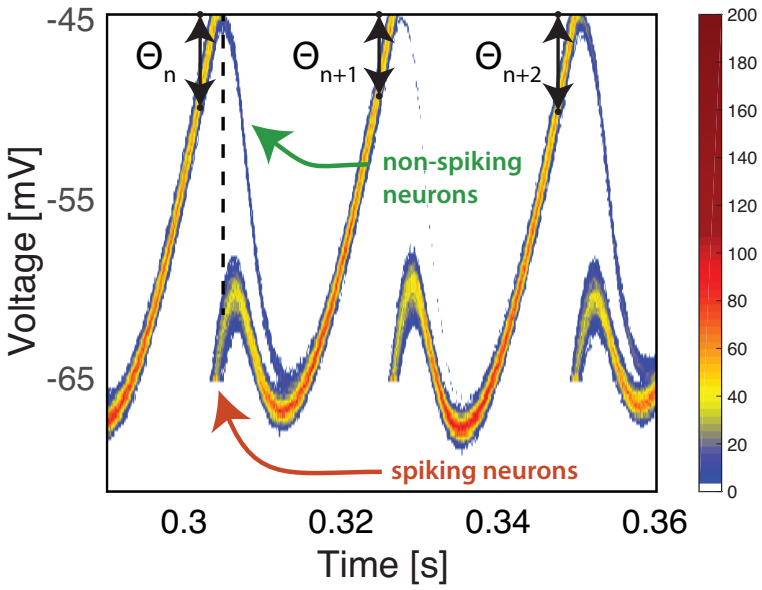

Figure 2.9. Noise increases the synchronizability of rhythms by allowing a variable number of neurons to spike. Time-dependence of the voltage distribution function of the oscillators in the periodically forced network 2 with color indicating the number of neurons in bins of size 0.2mV. Also shown is the lag θ_n in each cycle. The red (green) arrow marks spiking (non-spiking) neurons. Parameters as in Fig.2.7 except for $\rho^{(2)} = 1.02, \gamma_0 = 0.81$, $\sigma^2 = 0.3\text{s}^{-1}$.

To confirm this synchronization mechanism we remove the stabilizing feedback by adjusting in each cycle the strength g_{syn} of the self-inhibition in network 2 to compensate for the variable fraction $f_{spiking}(t)$ of spiking neurons,

$$g_{syn} \to g_{syn} \frac{\bar{f}_{spiking}}{f_{spiking}(t)}, \tag{2.15}$$

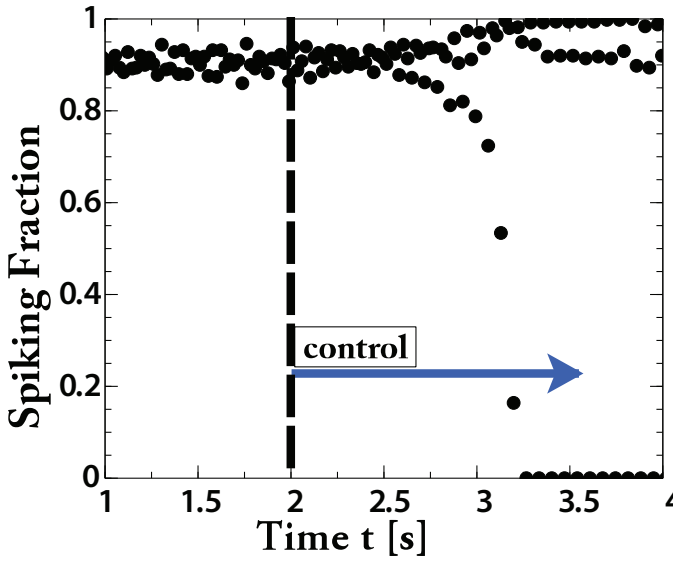

Figure 2.10. Synchrony is lost and replaced by a 3-cycle when the self-inhibition is rendered independent of the spiking fraction $f_{spiking}(t)$ via the control defined by equation (2.15) at $t = 2$s. Parameters as in Fig.2.7 except for $\rho^{(2)} = 0.975$, $\sigma^2 = 2\text{s}^{-1}$.

where $\bar{f}_{spiking}$ is the time average of $f_{spiking}(t)$ before the control is turned on. Indeed, synchronization is lost when this control is applied, as is apparent from the resulting strongly varying spiking fraction (Fig.2.10).

2.3.3. Period-Doubling

The phase diagrams shown in Figs.2.5,2.7 suggest that in this parameter regime synchronization is reached via a continuous period-doubling bifurcation. To confirm this explicitly for the single network with periodic forcing (Fig.2.7), we extract from

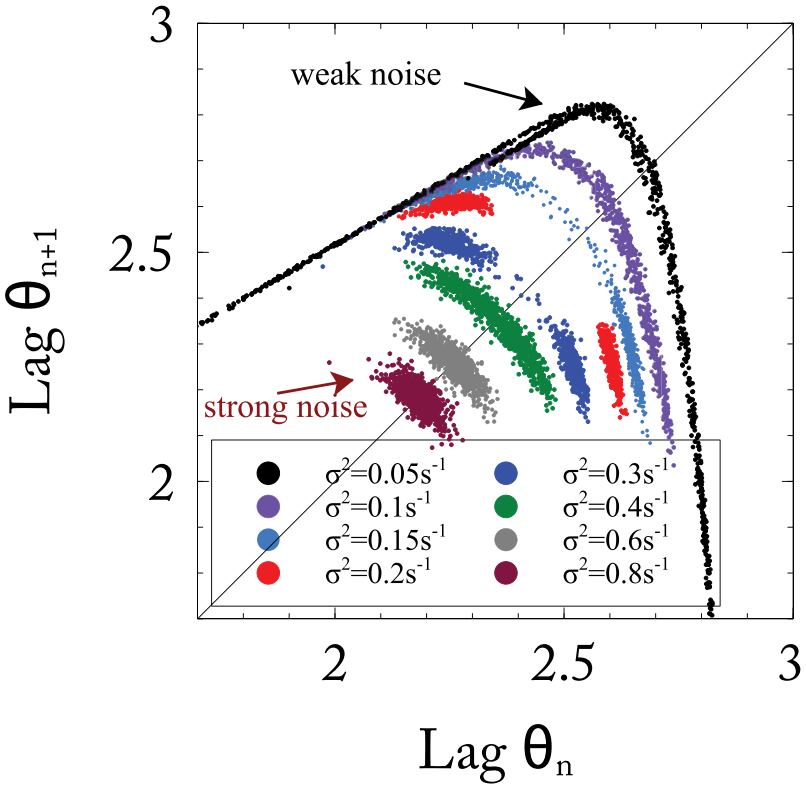

Figure 2.11. The iterated map for the lag θ_n of a periodically forced IF-network exhibits a period-doubling bifurcation (cf. Fig.2.9). Different colors show θ_n-sequence for one initial condition for different values of the noise σ^2. With increasing σ^2 the dynamics go from disordered to a noisy 2-cycle to a noisy fixed point. Parameters as in Fig.2.7 except for $N_\alpha = 5,000$, $\rho^{(2)} = 1.03, \gamma_0 = 0.81$, $g_{syn} = 4.2 \times 10^{-5}$.

the simulations an iterated map for the lag $\theta_n \equiv V_\theta - \bar{V}^{(2)}(t_n)$ where $\bar{V}^{(2)}$ is the LFP of network 2 and t_n is the time when neurons in network 1 spike in the n^{th} cycle; the θ_n are marked by double arrows in Fig.2.9. For small noise ($\sigma^2 = 0.05\text{s}^{-1}$) the iterates of θ_n trace out an almost continuous noisy attractor, corresponding to irregular

dynamics (Fig.2.11). When the noise is increased to $\sigma^2 = 0.2\text{s}^{-1}$, this attractor changes to two domains, corresponding to a noisy 2-cycle. With a further increase in the noise ($\sigma^2 = 0.6\text{s}^{-1}$) the two domains merge to a single, noisy fixed point that corresponds to the synchronized state. Conversely, when the noise is decreased, the synchronous state becomes unstable via a period-doubling bifurcation. In view of Fig.2.9 this instability can be understood intuitively by noting that for weak noise the voltage distribution of the neurons is narrow and even small changes in the timing of network 2 strongly affect its fraction $f_{spiking}$ of spiking neurons, resulting in a large gain in the feedback via self-inhibition. If that gain is too large, i.e. if the voltage distribution is too narrow, the feedback destabilizes the fixed point via a period-doubling bifurcation.

2.3.4. Networks of Morris-Lecar Neurons

The key elements of the synchronization are the heterogeneity of spike timing and the dependence of the frequency of the rhythm on the strength of the inhibition. This suggests that synchronization by uncorrelated noise should be found more generally in network rhythms that arise from inhibition. To test this we replace the IF-neurons with type-2 Morris-Lecar neurons (Fig.2.12). They have a very different phase-resetting curve than the IF-neurons, i.e. they respond very differently to weak δ-spike inputs. Consequently, for weak coupling individual Morris-Lecar neurons have

very different synchronization properties than individual IF-neurons [100]. As for the IF-neurons, the interaction between the Morris-Lecar neurons is taken to be via stereotpical inhibitory synaptic pulses that are triggered when V reaches a threshold of $V_\theta = 10mV$ and are described by equations (2.2,2.3). In these simulations we use a random, sparse connectivity in which each of the N_α oscillators in each network has a fixed number $\epsilon_1 N_\alpha$ of randomly chosen incoming connections from the oscillators within the same network and a lower, fixed number $\epsilon_2 N_\alpha$ of connections from the other network. Thus, the in-degree, but not the out-degree, of each oscillator is fixed.

Again, uncorrelated noise synchronizes the population rhythms (Fig.2.12A). For the parameters in Fig.2.12A rhythms other than 1:2 and 1:1 arise only for very small noise (inset of Fig.2.12A). As found for IF-neurons, turning on the feedback control (equation (2.15)), $g_{syn} \to g_{syn}\bar{f}_{spiking}/f_{spiking}(t)$, destroys the synchronization (Fig.2.12B), confirming the same synchronization mechanism.

2.3.5. Dependence of Synchronization on the Duration of Inhibition and the Reversal Potential

To assess the generality of the synchronization mechanism we vary key aspects of the inhibition: its temporal evolution and its reversal potential V_{rev}. To vary the effective delay and the duration of the inhibition we rescale the rise and decay times

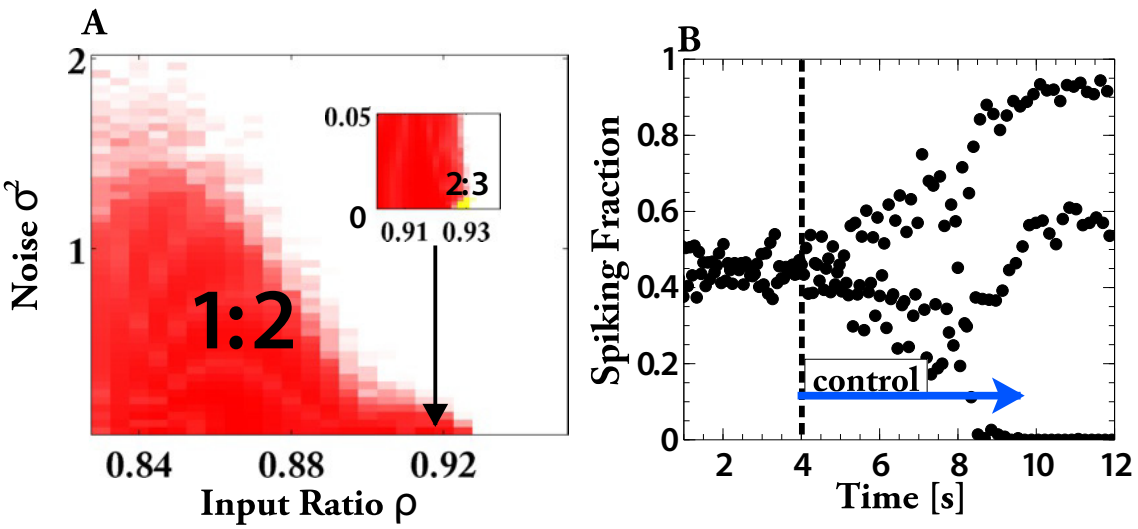

Figure 2.12. Noise synchronizes also coupled networks of type-2 Morris-Lecar neurons. (A) Phase diagram showing synchronization of two networks with increasing noise (inset shows blow-up). Colors as in Fig.2.7. (B) Loss of synchrony after turning on the control (equation (2.15)) for $\rho^{(2)} = 0.84$, $\sigma^2 = 2.5$.

$\tau_{1,2}$ by a common factor κ,

$$\dot{A}_i^{(1,2)} = -\frac{A_i^{(1,2)}}{\kappa\,\tau_{1,2}} + \sum_{j=1}^{N}\sum_{k} W_{ij}\,\delta\left(t - t_j^{(k)} - \tau_d\right). \tag{2.16}$$

For $\kappa > 1$ this shifts the decay and the peak of the inhibition to later times. The latter amounts to an increase in the effective delay. The reversal potential V_{rev} determines the dependence of the inhibition on the voltage of the cell receiving the inhibition,

$$I_i^{(syn)} = g_0\,\frac{g_{syn}}{R}\left(A_i^{(2)} - A_i^{(1)}\right)\left(V_{rev} - V_i\right). \tag{2.17}$$

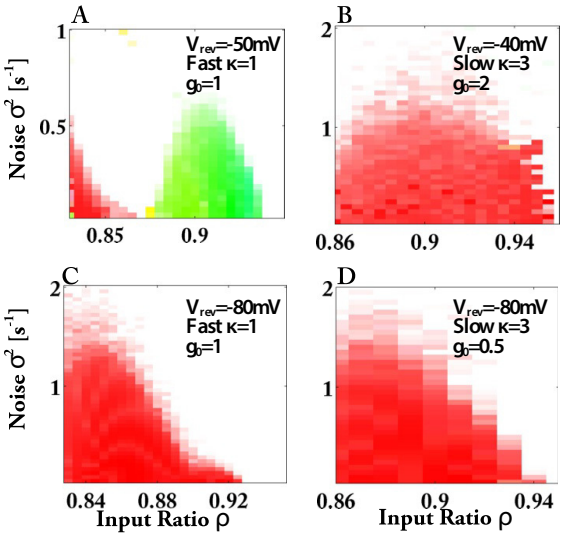

Figure 2.13. Phase diagrams for networks of type-2 Morris-Lecar neurons demonstrate that increasing noise synchronizes the rhythms for fast ($\kappa = 1$) and slow inhibition ($\kappa = 3$) and over a large range in reversal potential V_{rev}. Parameters as in Fig.2.12 with $V_{\theta_n} = 2$mV.

We have included a factor g_0 in Eq.(2.17), which indicates the change in the synaptic strength used in Figs.2.13,2.14 compared to the main part of the paper.

If the reversal potential is significantly below the resting potential of the cell, the conductance-based inhibition is very similar to inhibition by a fixed negative current. It shifts the voltage of the fixed point that corresponds to the non-spiking state to more negative (hyperpolarized) values. However, if the reversal potential is at the resting potential, inhibition vanishes for the non-spiking cell and the location of the fixed point is not affected. Nevertheless, synaptic input increases the conductance of the cell and functions as a shunt for any excitatory inputs, stabilizing the fixed

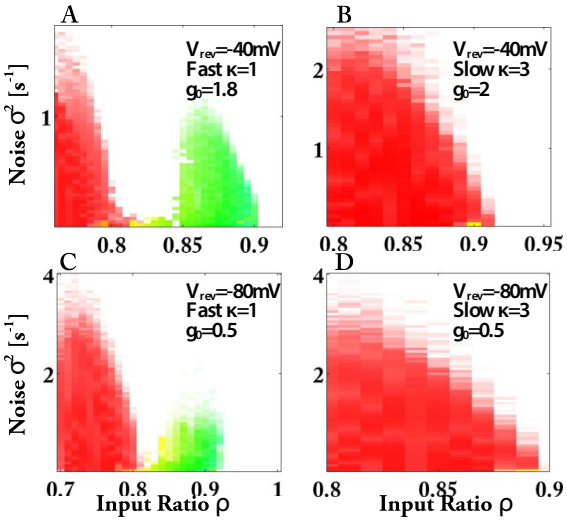

Figure 2.14. Phase diagrams for networks of type-1 Morris-Lecar neurons demonstrate that increasing noise synchronizes the rhythms for fast ($\kappa = 1$) and slow inhibition ($\kappa = 3$) and over a large range in reversal potential V_{rev}. Parameters as in Fig.2.12 with $V_{\theta_n} = 12$mV.

point. With respect to the formation of a γ-rhythm within an individual network it is known that with shunting inhibition type-2 neurons tend to synchronize only poorly and the γ-rhythms themselves tend to be ffragile [101].

We find that uncorrelated noise synchronizes the rhythms over a wide range of the time scale of the inhibition and of the reversal potential for networks of type-1 neurons (Fig.2.14) and of type-2 neurons (Fig.2.13). Here we use the Morris-Lecar model for both types of neurons. Interestingly, in some cases the synchronization does not involve a period-doubling bifurcation (Figs.2.13A, 2.14A,C). For values of the reversal potential close to the resting potential synchronization does not occur

for type-2 Morris-Lecar neurons, reflecting the fragility of the γ-rhythms themselves [101].

2.3.6. A Heuristic One-dimensional Map Model

The simplicity of the mechanism identified in our simulations (Fig.2.9) suggests that its essence may be captured in a simplified model. The temporal evolution of the voltage distribution of the neurons in network 2 shows that the voltage distribution is quite sharply peaked. Moreover, shortly before the times when the periodic inhibition arrives in network 2 the distribution is close to unimodal and can be characterized by the LFP of network 2 and its lag relative to network 1 or the periodic inhibition. This allows us to develop a phenomenological Poincare map for the lag θ.

Figs.2.13,2.14 indicate that the synchronization mechanism is not very sensitive to the voltage dependence of the inhibition. For simplicity we therefore assume that the inhibition resets the voltage of an oscillator by an amount proportional to its voltage and write the evolution of a normalized mean voltage (LFP) $\bar{V}$ as

$$\begin{aligned} \dot{\bar{V}} &= \rho_{map} - g_1\,\bar{V}(t) \sum_{n=-\infty}^{\infty} \delta\left(t-(n+\tau_d)\right) \\ &\quad -g_2\,P(\bar{V}(t-\tau_d))\,\bar{V}(t), \end{aligned} \tag{2.18}$$

with $\bar{V}$ being reset to $\bar{V}=0$ instantaneously when it reaches $\bar{V}=1$. The second term in equation (2.18) represents a periodic external forcing with strength g_1 and

period 1. The third term models the self-inhibition of the network. Its strength depends on the number $P(\bar{V}(t))$ of oscillators that are at the spike threshold when the LFP has the value $\bar{V}$. The evolution of $\bar{V}(t)$ is shown in Fig.2.15A.

$P(\bar{V}(t))$ reflects the voltage distribution of the oscillators, which results in a heterogeneity in the spike times of the oscillators in network 2. The simulations of the integrate-fire model indicate that this heterogeneity plays a central role (Fig.2.9). Instead of considering an evolution equation for the voltage distribution, for our minimal model we consider it time-independent and of the form

$$P(\bar{V}) = \begin{cases} \frac{1}{\sigma_{map}} & \bar{V} \in [0, \frac{1}{2}\sigma_{map}] \cup [1 - \frac{1}{2}\sigma_{map}, 1) \\ 0 & \text{otherwise.} \end{cases} \tag{2.19}$$

Thus, for $\bar{V} \in [0, \sigma_{map}/2]$ neurons in the trailing half of the distribution are firing, while for $\bar{V} \in [1 - \sigma_{map}/2, 1)$ neurons in the leading half are firing.

With $n + \tau_d$ the time at which the periodic inhibition arrives in the n^{th}-cycle and letting t_n be the time at which $\bar{V}$ reaches threshold, $\bar{V}(t_n) = 1$, we focus on the situation in which the external inhibition arrives before any of the self-inhibition sets in that is triggered by the oscillators in network 2,

$$n + \tau_d < t_n - \frac{\sigma_{map}}{2\rho_{map}} + \tau_d.$$

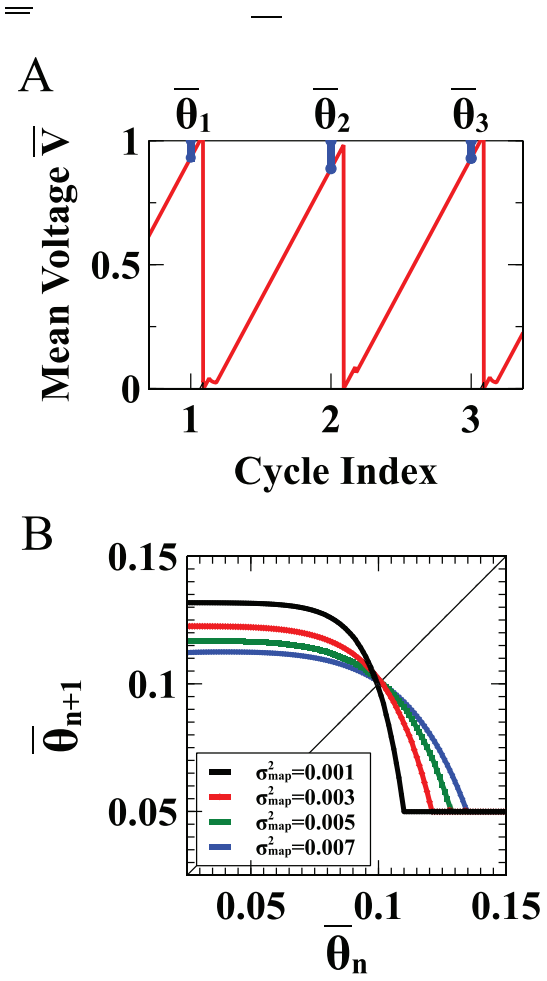

Figure 2.15. The synchronization via reverse period-doubling can be captured in a heuristic map model. A) Temporal evolution of the normalized mean voltage $\bar{V}$, with lag $\bar{\theta}_n$ indicated and plotted in terms of the cycles of the periodic inhibition. B) Map given by equation (2.21). The fixed point becomes stable with increasing noise level σ^2_{map}.

The external inhibition induces a reset

$$\bar{V}(n+\tau_d) \to e^{-g_1}\bar{V}(n+\tau_d).$$

For sufficiently strong coupling g_1 it keeps the trailing oscillators from spiking and from contributing to the self-inhibition. Thus, self-inhibition lasts from

$$t_n^< = t_n - \frac{\sigma_{map}}{2\rho_{map}} + \tau_d$$

to

$$t_n^> = \min\left(n + 2\tau_d, t_n + \frac{\sigma_{map}}{2\rho_{map}} + \tau_d\right).$$

During that time $\Delta t \equiv t_n^> - t_n^<$ it induces a voltage change that leads to

$$\bar{V}(t_n^>) = e^{-g_2\frac{\rho_{map}}{\sigma_{map}}\Delta t}\bar{V}(t_n^<) + \frac{\sigma_{map}}{g_2}(1 - e^{-g_2\frac{\rho_{map}}{\sigma_{map}}\Delta t}). \tag{2.20}$$

Combining equation (2.20) with the voltage evolution during the remaining time yields a Poincare map for the lag $\bar{\theta}_n \equiv 1 - \bar{V}(n)$ of network 2 relative to the periodic inhibitory input (Fig.2.15B),

$$\bar{\theta}_{n+1} = F(\bar{\theta}_n). \tag{2.21}$$

The fixed point $\bar{\theta}_{FP} = F(\bar{\theta}_{FP})$ corresponds to a 1:1 synchronized state. Its stability depends on the slope $F'(\bar{\theta}_{FP})$. It is only stable ($\left|F'(\bar{\theta}_{FP})\right| < 1$) for large widths σ_{map}

of the distribution P, i.e. for sufficiently strong noise, and becomes unstable via a period-doubling bifurcation at $F'(\bar{\theta}_{FP}) = -1$ as the noise is reduced.

Thus, this simple map model extracts the key role of the noise-induced heterogeneity of the spike times in network 2 in the synchronization of the population rhythms found in the full network simulations (Figs.2.5,2.7,2.12) and gives further support for the mechanism that we extracted from our simulations (Figs.2.9,2.12).

Thus, desynchronization of the neurons within a network can enhance the synchronizability of the collective oscillation of a network with externally applied periodic inhibition or with the inhibition provided by rhythms in other networks.

2.3.7. Minimal Network Size for Synchronization

The synchronization mechanism identified in Fig.2.9 is specific to population rhythms of networks rather than oscillations of individual neurons, since it requires the number of spiking neurons and the associated inhibition within the network to decrease with increasing lag of the network. The discreteness of the network size suggests that in small networks the inhibition will be too coarsely quantized to stabilize synchrony. This is indeed the case. While the total spectral power S_{tot} of the LFP of network 2, which characterizes the strength of the rhythm itself, depends only weakly on noise and network size (Figure 2.16B), the subharmonic spectral power S_{sub} of that LFP, which includes only the frequencies below the dominant frequency, decreases

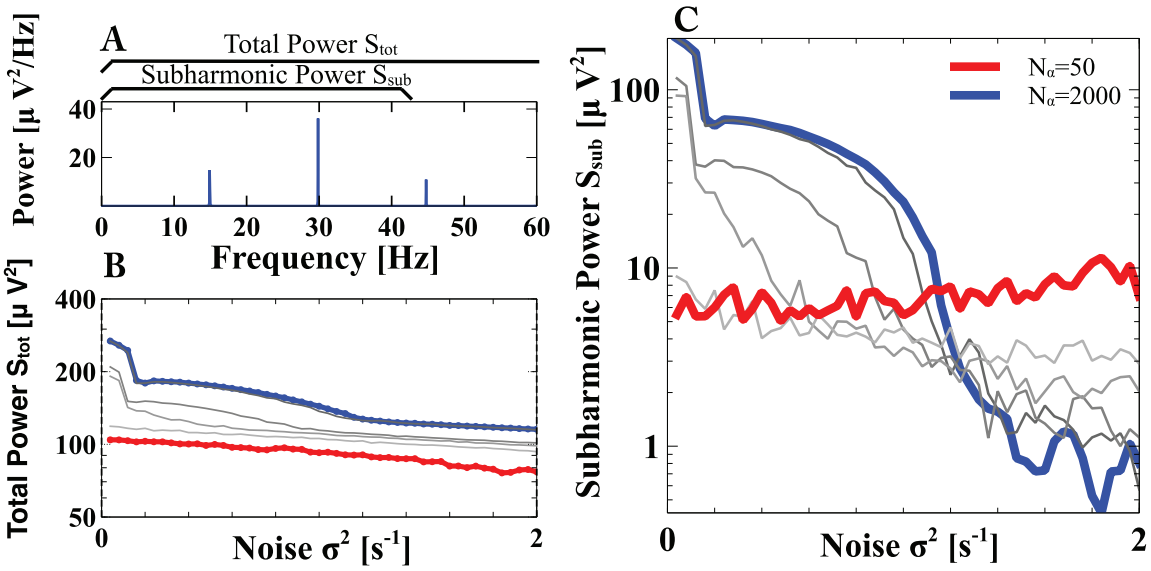

Figure 2.16. Synchronization by noise requires a minimal network size N_α. A) Spectrum of the LFP of network 2 indicating the frequency range included in the total power S_{tot} and the subharmonic power S_{sub}. B) S_{tot} depends only moderately on noise strength and network size (network sizes as given in the legends of panel C). C) Only for sufficiently large networks the subhamornic spectral power S_{sub} decreases strongly with increasing noise strength indicating synchronization (note the logarithmic scale). Network sizes N_α: 50 (red), 100, 200, 500, 1,000, 2,000 (blue). Other parameters as in Fig.2.7.

substantially with increasing noise in large networks, confirming the synchronization (note the logarithmic scale in Figure 2.16C). As the network size is reduced, however, this decrease in S_{sub} with noise becomes smaller and for networks of size $N_\alpha < 100$ the subharmonic power is quite independent of the noise, indicating that noise does not synchronize the rhythms in such small networks.

2.3.8. Diffusively Coupled Networks of Relaxation Oscillators

In the neuronal models the interaction between the oscillators is via synaptic inhibition that is triggered by the oscillator and that has a stereotypical, possibly delayed waveform, the amplitude and duration of which are independent of the waveform and frequency of the oscillator. In particular, an oscillation that barely reaches threshold provides full inhibition, whereas a slightly smaller oscillation generates no inhibition at all. To address the question whether uncorrelated noise can synchronize population rhythms beyond this neuronal context we investigate interconnected networks of relaxation oscillators that are coupled via an additional field that is driven directly by one of the oscillator variables in a graded fashion (equations (2.10)-(2.12)). The coupling therefore reflects the waveform, amplitude, and duration of the ongoing oscillation and is similar to that used in various models of quorum sensing [92, 93, 94].

To assess the synchronization among a large number of interconnected networks we use a weighted overall order parameter $r_{global}(t)$ that corrects for the non-uniform evolution of the phase, when it is based on the analytic signal of the relaxation oscillator. Fig.2.17 shows results for $\mathcal{N} = 200$ networks with $N_\alpha = 80$ oscillators each. In contrast to Fig.2.3 where the temporal evolution of the phase $\phi^{(\alpha)}(t)$ of the population rhythm is shown, Fig.2.17A shows the evolution of $x_i^{(\alpha)}(t)$ of individual oscillators. For clarity only the oscillators in every fourth network are displayed. To vary the natural frequency of the oscillators in different networks we

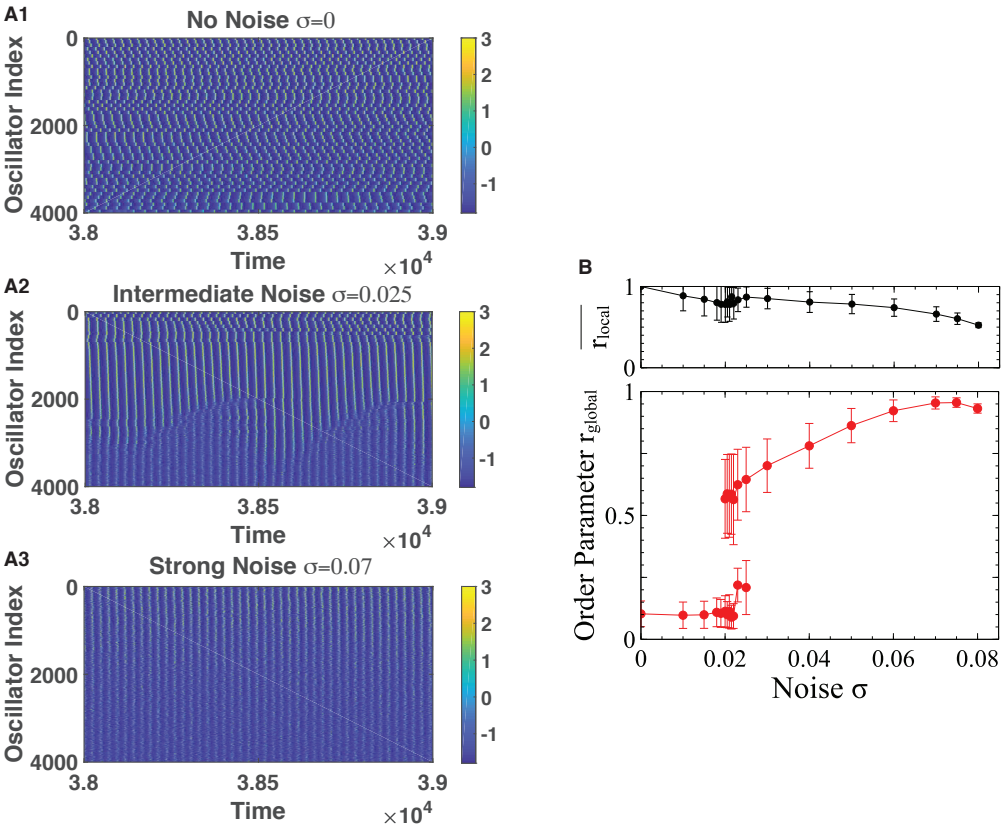

Figure 2.17. Noise synchronizes interconnected networks of relaxation oscillators . A) Space-time diagram of $x_i^{(\alpha)}(t)$ for 50 of the $\mathcal{N} = 200$ networks with $N_\alpha = 80$ oscillators each. Networks are not synchronized for vanishing noise, $\sigma = 0$ (A1). Partial, oscillatory synchronization for $\sigma = 0.025$ (A2). Almost complete synchronization for $\sigma = 0.07$ (A3). B) Lower panel: temporal mean and standard deviation of the global order parameter r_{global} showing a discontinuous transition to an ordered regime as the uncorrelated noise is increased. Upper panel: mean local order parameter $\bar{r}_{local}$ decreases with noise.

set $\gamma_i^{(\alpha)} = 1.9 + 1.2(\alpha - 1)/(\mathcal{N} - 1),\ \alpha = 1 \ldots \mathcal{N}$. The strong coupling within each of the interconnected networks synchronizes the oscillators within each network, but for vanishing noise these collective oscillations are not synchronized or phase-locked (Fig.2.17A1). Thus, the average $\bar{r}_{local}$ of the order parameters $r_{local}^{(\alpha)}$ of the individual networks is high, but the time-averaged global order parameter r_{global} is low (Fig.2.17B). However, similar to the case of the IF-networks (Fig.2.3), as the uncorrelated noise is increased - at fixed coupling strength - the system undergoes a discontinuous transition to a state in which the rhythms of most networks are synchronized, reflected in a jump in r_{global} (Fig.2.17A2,B).

Close to the transition point the system intermittently jumps between the ordered and the disordered branch; for this system size no true hysteresis is obtained. In this regime the individual order parameters $r_{local}^{(\alpha)}$ are much lower for the networks with low natural frequency than for the faster networks, with a sharp transition between them (Fig.2.17A2). As the noise is increased further, the global order parameter rises further, while the average $\bar{r}_{local}$ of the individual order parameters decreases (Fig.2.17A3,B). In the IF-networks the slower networks can keep up with the faster ones because their neurons spike only in fewer cycles, i.e. their spiking fraction is reduced. Similarly, the relaxation oscillators in the slower networks less often reach the right branch of the x-nullcline (cf. Fig.2.2) than those in the faster networks, resulting in a smaller production of the rapidly diffusing substance that provides

the coupling between the oscillators. This speeds up the slower networks. For yet stronger noise, not only the individual order parameteres $r_{local}^{(\alpha)}$ decrease, but also the global order parameter r_{global}.

Interestingly, for $0.019 \leq \sigma \leq 0.025$ the global order parameter r_{global} exhibits slow oscillations in the ordered state, which are reflected in its large standard deviation. They reflect an 'invasion' of the stronger disorder of the slower networks into the faster networks and a subsequent sudden retraction of this front (Fig.2.17A2). Since the coupling between the networks is all-to-all, this invasion indicates that the slower networks are more susceptible to perturbations than the faster ones. The oscillations become weaker as the noise is increased. A study of these interesting oscillations is beyond the scope of this paper.

2.4. Discussion

We have considered interconnected networks of oscillators for strong coupling of the oscillators within and across networks. This regime is beyond the weak-coupling limit and does not allow a reduction to a phase description within the framework of Kuramoto models. We have focussed on the collective oscillations (population rhythms) that emerge from the synchronization of the oscillators within each of the networks and have addressed the question to what extent these rhythms can synchronize with each other or to an external periodic pace-maker. Strikingly, we have found that uncorrelated noise can substantially enhance this synchronization.

As a key component of the underlying mechanism we have identified that the strong inter-network coupling - combined with the noise - can render the dynamics within each network highly heterogeneous with a variable subset of oscillators skipping cycles in an irregular fashion. More specifically, the synchronization of the rhythms arises from the following core aspects of the systems:

1. The synchronization of oscillators within each network is quite robust. To ensure this robustness in the neuronal models we included an explicit delay in the interaction to avoid that the neuronal populations of the uncoupled networks form clusters rather than being fully synchronized [102].

2. The frequency of the rhythm of each network decreases with increasing coupling between the oscillators within the network. This is a characteristic feature of the ubiquitous neuronal γ-rhythm generated by the ING- or PING mechanism [72].

3. The strength of the interaction between the oscillators depends on their oscillation amplitude. This allows the overall coupling within a network and with it the frequency of the rhythm to depend on the degree to which the oscillators participate in the collective oscillation. This is naturally the case in neuronal systems with chemical synapses where the output of a neuron depends on whether the neuron spikes or not. In cellular oscillators, e.g. genetic oscillators, such a coupling is likely to arise if the production of the substance that provides the communication between the cells depends on one of the oscillating variables [93, 94].

4. The inter-network coupling is sufficiently strong and acts on a time scale that allows to impact oscillators differently depending on whether they are leading or lagging the collective oscillation. In the models discussed here the inter-network coupling suppresses the oscillations of the lagging oscillators, which modifies the frequency of the rhythm they are participating in. This feedback enhances the stability of the synchronized state.

Noise is essential for the synchronization, since it spreads out the phases of the oscillators, which then allows the inter-network coupling to suppress the trailing but not the leading oscillations. In essence, the enhanced synchronizability of these collective oscillations emerges from the noise-induced desynchronization within each network. Importantly, the synchronization of different population rhythms does therefore not imply the synchronization of the oscillators within a network or across networks. In fact, with increasing noise the within-network correlations decrease.

Since the within-network desynchronization plays a key role in the synchronization mechanism, our analysis suggests that population rhythms could also be synchronized by heterogeneity in the natural frequencies of the oscillators within each network [103].

Since the external inhibition acting on each network modifies the self-inhibition of that network and with it its frequency, the synchronization mechanism has some similarity with that proposed in [104] for the flash synchronization in certain species

of fireflies. However, there the external flash leads to a slow and persistent adaptation of the intrinsic frequency of the rhythms of the fireflies, while in the systems discussed here the frequency change is quite fast and - at least for very strong self-inhibition - it does not persist very long. This may be different for weaker self-inhibition, for which the synchronization transition does not always involve a period-doubling bifurcation (cf. Fig.2.13A).

Most of the results presented here are formulated in terms of neuronal systems, motivated by the wide-spread appearance of γ-rhythms in the brain and by the widely investigated hypothesis that coherence of γ-rhythms in different brain areas is an important element of information transmission between these areas [62, 63, 64, 65, 66, 49, 50]. The synchronization of different γ-rhythms can also be relevant in intertwined subnetworks of a single, modularly structured brain area [82, 83, 84, 9, 85]. In this context, our results point to a possible new constructive role of noise in the communication between different brain areas and the information processing within a single area.

It should be noted that most, but not all [99], neuronal networks of the brain that exhibit γ-rhythms comprise inhibitory as well as excitatory neurons. Depending on the balance between excitatory and inhibitory coupling and on the associated time scales the rhythms generated by these networks can be closer to an ING-rhythm or a PING-rhythm (pyramidal interneuron network gamma) [69]. A general analysis

of the effect of noise on the interaction of rhythms in two excitatory-inhibitory (EI) networks is very complex, since it involves 4 different types of connections (II, EI, IE, EE) among the neurons of the two networks. In order to be able to isolate and elucidate the synchronization mechanism in detail, we have focused in this paper on the core property that is common to ING and PING γ-rhythms, which is the delay of spiking by inhibition.

The noise-induced synchronization in interconnected networks is not limited to neuronal rhythms. Our results for relaxation oscillators show that it can be relevant for rhythms more generally [105]. In fact, our model is similar to a model proposed for the interaction of genetic oscillators [93]. In such systems molecular noise can be an integral component due to the small copy number of some of the participating reactants. More specifically, the synchronization of the collective oscillation of a single network of oscillators by an external forcing (cf. Fig.2.7) is, for instance, relevant in the entrainment of the rhythm generated by the biomolecular circadian oscillators in the $\sim 20,000$ cells of the suprachiasmatic nucleus by the day-night cycle [106]. Interestingly, there it has been observed that transient desynchronization of the oscillations of the individual cells accelerates the entrainment of the overall rhythm after shifts in the light schedule [107]. Whether the phase-heterogeneity of the cells plays a role similar to that described here is not clear.

In cyanobacteria the coupling between the circadian rhythms of different bacteria is extremely weak [108]. However, within each bacterium the coupling between the proteins that constitute the individual oscillating units is strong [109, 110]. This raises the possibility that molecular noise may enhance the entrainment of this circadian rhythm by the day-night cycle.

The type of synchronization identified here could also be amenable to experimental investigations in chemical oscillations like the Belousov-Zhabotinsky reaction where the reaction can be localized on a large number of beads and the interaction can be supplied by feedback that exploits the light sensitivity of the reaction [111].

The global order parameter of interconnected networks can exhibit non-trivial dynamics [112]. For the networks of relaxation oscillators we find that on the upper, ordered branch, which is reached in a discontinuous transition as the noise is increased, the order parameter exhibits persistent oscillations that are associated with the invasion and retraction of front-like structures that separate more tightly synchronized networks from less synchronized ones. The origin of these dynamics is not yet understood.

References

[1] Brett A Johnson, Haleh Farahbod, Sepideh Saber, and Michael Leon. Effects of functional group position on spatial representations of aliphatic odorants in the rat olfactory bulb. *Journal of Comparative Neurology*, 483(2):192–204, 2005.

[2] Tonghui Xu, Xinzhu Yu, Andrew J Perlik, Willie F Tobin, Jonathan A Zweig, Kelly Tennant, Theresa Jones, and Yi Zuo. Rapid formation and selective stabilization of synapses for enduring motor memories. *Nature*, 462(7275):915, 2009.

[3] Guang Yang, Feng Pan, and Wen-Biao Gan. Stably maintained dendritic spines are associated with lifelong memories. *Nature*, 462(7275):920, 2009.

[4] Akiko Hayashi-Takagi, Sho Yagishita, Mayumi Nakamura, Fukutoshi Shirai, Yi I Wu, Amanda L Loshbaugh, Brian Kuhlman, Klaus M Hahn, and Haruo Kasai. Labelling and optical erasure of synaptic memory traces in the motor cortex. *Nature*, 525(7569):333, 2015.

[5] Yoav Livneh and Adi Mizrahi. Experience-dependent plasticity of mature adult-born neurons. *Nature neuroscience*, 15(1):26, 2012.

[6] Jaime Grutzendler, Narayanan Kasthuri, and Wen-Biao Gan. Long-term dendritic spine stability in the adult cortex. *Nature*, 420(6917):812, 2002.

[7] Yi Zuo, Guang Yang, Elaine Kwon, and Wen-Biao Gan. Long-term sensory deprivation prevents dendritic spine loss in primary somatosensory cortex. *Nature*, 436(7048):261, 2005.

[8] Yi Zuo, Aerie Lin, Paul Chang, and Wen-Biao Gan. Development of long-term dendritic spine stability in diverse regions of cerebral cortex. *Neuron*, 46(2):181–189, 2005.

[9] Kurt A. Sailor, Matthew T. Valley, Martin T. Wiechert, Hermann Riecke, Gerald J. Sun, Wayne Adams, James C. Dennis, Shirin Sharafi, Guo-Li Ming, Hongjun Song, and Pierre-Marie Lledo. Persistent structural plasticity optimizes sensory information processing in the olfactory bulb. *Neuron*, 91(2):384–396, Jul 2016.

[10] Santiago Cajal. Ramon y: Histologie du systeme nerveux de l'homme et des vertebres. *Paris: Maloine*, 1911.

[11] Monica W Chu, Wankun L Li, and Takaki Komiyama. Balancing the robustness and efficiency of odor representations during learning. *Neuron*, 92(1):174–186, 2016.

[12] Olivier Gschwend, Nixon M Abraham, Samuel Lagier, Frédéric Begnaud, Ivan Rodriguez, and Alan Carleton. Neuronal pattern separation in the olfactory bulb improves odor discrimination learning. *Nature neuroscience*, 18(10):1474, 2015.

[13] Wankun L Li, Monica W Chu, An Wu, Yusuke Suzuki, Itaru Imayoshi, and Takaki Komiyama. Adult-born neurons facilitate olfactory bulb pattern separation during task engagement. *Elife*, 7:e33006, 2018.

[14] Olaf Bergmann, Jakob Liebl, Samuel Bernard, Kanar Alkass, Maggie SY Yeung, Peter Steier, Walter Kutschera, Lars Johnson, Mikael Landén, Henrik Druid, et al. The age of olfactory bulb neurons in humans. *Neuron*, 74(4):634–639, 2012.

[15] Mahua Chatterjee, Fernando Perez de los Cobos Pallares, Alex Loebel, Michael Lukas, and Veronica Egger. Sniff-like patterned input results in long-term plasticity at the rat olfactory bulb mitral and tufted cell to granule cell synapse. *Neural plasticity*, 2016, 2016.

[16] Vincent Breton-Provencher, Daniel Coté, and Armen Saghatelyan. Activity of the principal cells of the olfactory bulb promotes a structural dynamic on the distal dendrites of immature adult-born granule cells via activation of nmda receptors. *Journal of Neuroscience*, 34(5):1748–1759, 2014.

[17] Vincent Breton-Provencher, Karen Bakhshetyan, Delphine Hardy, Rodrigo Roberto Bammann, Francesco Cavarretta, Marina Snapyan, Daniel Côté, Michele Migliore, and Armen Saghatelyan. Principal cell activity induces spine relocation of adult-born interneurons in the olfactory bulb. *Nature communications*, 7:12659, 2016.

[18] Jon W Johnson and Shawn E Kotermanski. Mechanism of action of memantine. *Current opinion in pharmacology*, 6(1):61–67, 2006.

[19] Graeme Lowe. Electrical signaling in the olfactory bulb. *Current opinion in neurobiology*, 13(4):476–481, 2003.

[20] Peter Dayan, Laurence F Abbott, and L Abbott. *Theoretical neuroscience: computational and mathematical modeling of neural systems*, chapter 7. Network Models, pages 229–278. MIT press Cambridge, MA, 2001.

[21] H Sebastian Seung, Tom J Richardson, Jeffrey C Lagarias, and John J Hopfield. Minimax and hamiltonian dynamics of excitatory-inhibitory networks. In *Advances in neural information processing systems*, pages 329–335, 1998.

[22] Hiroyuki K Kato, Monica W Chu, Jeffry S Isaacson, and Takaki Komiyama. Dynamic sensory representations in the olfactory bulb: modulation by wakefulness and experience. *Neuron*, 76(5):962–975, 2012.

[23] Adil G Khan, Mukund Thattai, and Upinder S Bhalla. Odor representations in the rat olfactory bulb change smoothly with morphing stimuli. *Neuron*, 57(4):571–585, 2008.

[24] Vijay Singh, Nicolle R Murphy, Vijay Balasubramanian, and Joel D Mainland. A competitive binding model predicts nonlinear responses of olfactory receptors to complex mixtures. *arXiv preprint arXiv:1805.00563*, 2018.

[25] Edward Orona, Elizabeth C Rainer, and John W Scott. Dendritic and axonal organization of mitral and tufted cells in the rat olfactory bulb. *Journal of Comparative Neurology*, 226(3):346–356, 1984.

[26] Nathaniel N Urban. Lateral inhibition in the olfactory bulb and in olfaction. *Physiology & behavior*, 77(4-5):607–612, 2002.

[27] Menahem Segal. Dendritic spines: morphological building blocks of memory. *Neurobiology of learning and memory*, 138:3–9, 2017.

[28] Ivar S Stein, John A Gray, and Karen Zito. Non-ionotropic nmda receptor signaling drives activity-induced dendritic spine shrinkage. *Journal of Neuroscience*, 35(35):12303–12308, 2015.

[29] Elie L Bienenstock, Leon N Cooper, and Paul W Munro. Theory for the development of neuron selectivity: orientation specificity and binocular interaction in visual cortex. *Journal of Neuroscience*, 2(1):32–48, 1982.

[30] Gabriel Lepousez, Antoine Nissant, Alex K Bryant, Gilles Gheusi, Charles A Greer, and Pierre-Marie Lledo. Olfactory learning promotes input-specific synaptic plasticity in adult-born neurons. *Proceedings of the National Academy of Sciences*, 111(38):13984–13989, 2014.

[31] Nathalie Mandairon, Nicola Kuczewski, Florence Kermen, Jérémy Forest, Maellie Midroit, Marion Richard, Marc Thevenet, Joelle Sacquet, Christiane Linster, and Anne Didier. Opposite regulation of inhibition by adult-born granule cells during implicit versus explicit olfactory learning. *Elife*, 7:e34976, 2018.

[32] Friedemann Zenke and Wulfram Gerstner. Hebbian plasticity requires compensatory processes on multiple timescales. *Philosophical Transactions of the Royal Society B: Biological Sciences*, 372(1715):20160259, 2017.

[33] Gina Turrigiano. Homeostatic synaptic plasticity: local and global mechanisms for stabilizing neuronal function. *Cold Spring Harbor perspectives in biology*, 4(1):a005736, 2012.

[34] Alain Artola and Wolf Singer. Long-term depression of excitatory synaptic transmission and its relationship to long-term potentiation. *Trends in neurosciences*, 16(11):480–487, 1993.

[35] Mélissa M Moreno, Christiane Linster, Olga Escanilla, Joëlle Sacquet, Anne Didier, and Nathalie Mandairon. Olfactory perceptual learning requires adult neurogenesis. *Proceedings of the National Academy of Sciences of the United States of America*, 106(42):17980, 2009.

[36] D. O. Hebb. *The organization of behavior; a neuropsychological theory.* Wiley, New York, 1949.

[37] Wayne Adams, James N Graham, Xuchen Han, and Hermann Riecke. Top-down inputs drive neuronal network rewiring and context-enhanced sensory processing in olfaction. *PLoS computational biology*, 15(1):e1006611, 2019.

[38] Won Chan Oh, Laxmi Kumar Parajuli, and Karen Zito. Heterosynaptic structural plasticity on local dendritic segments of hippocampal ca1 neurons. *Cell reports*, 10(2):162–169, 2015.

[39] Jochen Triesch, Anh Duong Vo, and Anne-Sophie Hafner. Competition for synaptic building blocks shapes synaptic plasticity. *Elife*, 7:e37836, 2018.

[40] Naoki Hiratani and Tomoki Fukai. Hebbian wiring plasticity generates efficient network structures for robust inference with synaptic weight plasticity. *Frontiers in neural circuits*, 10:41, 2016.

[41] Andreas Knoblauch, Edgar Körner, Ursula Körner, and Friedrich T Sommer. Structural synaptic plasticity has high memory capacity and can explain graded amnesia, catastrophic forgetting, and the spacing effect. *PloS one*, 9(5):e96485, 2014.

[42] Friedemann Zenke, Ben Poole, and Surya Ganguli. Continual learning through synaptic intelligence. In *Proceedings of the 34th International Conference on Machine Learning-Volume 70*, pages 3987–3995. JMLR. org, 2017.

[43] Jérémy Forest, Laura Chalençon, Maëllie Midroit, Claire Terrier, Isabelle Caillé, Joëlle Sacquet, Claire Benetollo, Killian Martin, Marion Richard, Anne Didier, et al. Role of adult-born versus preexisting neurons born at p0 in olfactory perception in a complex olfactory environment in mice. *Cerebral Cortex*, 2019.

[44] Antoine Nissant, Cedric Bardy, Hiroyuki Katagiri, Kerren Murray, and Pierre-Marie Lledo. Adult neurogenesis promotes synaptic plasticity in the olfactory bulb. *Nature neuroscience*, 12(6):728, 2009.

[45] C. Jehl, J. P. Royet, and A. Holley. Odor discrimination and recognition memory as a function of familiarization. *Perception & psychophysics*, 57(7):1002–1011, 1995.

[46] Gabriel Lepousez, Matthew T Valley, and Pierre-Marie Lledo. The impact of adult neurogenesis on olfactory bulb circuits and computations. *Annual review of physiology*, 75:339–363, 2013.

[47] Jean-Claude Platel, Alexandra Angelova, Stephane Bugeon, Thibault Ganay, Ilona Chudotvorova, Jean-Christophe Deloulme, Christophe Beclin, Marie-Catherine Tiveron, Nathalie Core, and Harold Cremer. Neuronal integration in the adult olfactory bulb is a non-selective addition process. *bioRxiv*, page 289009, 2018.

[48] Guangyu Robert Yang, Madhura R Joglekar, H Francis Song, William T Newsome, and Xiao-Jing Wang. Task representations in neural networks trained to perform many cognitive tasks. *Nature neuroscience*, 22(2):297, 2019.

[49] G. Buzsaki and E. W. Schomburg. What does gamma coherence tell us about inter-regional neural communication? *Nature Neuroscience*, 18(4):484–489, April 2015.

[50] Pascal Fries. Rhythms for cognition: Communication through coherence. *Neuron*, 88:220–235, Oct 2015.

[51] Nathalie Buonviso, Corine Amat, Philippe Litaudon, Stephane Roux, Jean-Pierre Royet, Vincent Farget, and Gilles Sicard. Rhythm sequence through the

olfactory bulb layers during the time window of a respiratory cycle. *European Journal of Neuroscience*, 17(9):1811–1819, 2003.

[52] Jennifer Beshel, Nancy Kopell, and Leslie M. Kay. Olfactory bulb gamma oscillations are enhanced with task demands. *Journal of Neuroscience*, 27(31):8358–8365, 2007.

[53] F. Dörfler and F. Bullo. Synchronization in complex networks of phase oscillators: A survey. *Automatica*, 50(6):1539–1564, June 2014.

[54] F. A. Rodrigues, T. K. D. M. Peron, P. Ji, and J. Kurths. The Kuramoto model in complex networks. *Physics Reports-Review Section of Physics Letters*, 610:1–98, January 2016.

[55] R. A. York and R. C. Compton. Quasi-optical power combining using mutually synchronized oscillator arrays. *IEEE Transactions on Microwave Theory and Techniques*, 39(6):1000–1009, June 1991.

[56] H. Bruesselbach, D. C. Jones, M. S. Mangir, M. Minden, and J. L. Rogers. Self-organized coherence in fiber laser arrays. *Optics Letters*, 30(11):1339–1341, June 2005.

[57] K. Wiesenfeld, P. Colet, and S. H. Strogatz. Synchronization transitions in a disordered Josephson series array. *Phys. Rev. Lett.*, 76(3):404–407, January 1996.

[58] M. A. Zhang, G. S. Wiederhecker, S. Manipatruni, A. Barnard, P. McEuen, and M. Lipson. Synchronization of micromechanical oscillators using light. *Physical Review Letters*, 109(23):233906, December 2012.

[59] D. C. Michaels, E. P. Matyas, and J. Jalife. Mechanisms of sinoatrial pacemaker synchronization - a new hypothesis. *Circulation Research*, 61(5):704–714, November 1987.

[60] C. Liu, D. R. Weaver, S. H. Strogatz, and S. M. Reppert. Cellular construction of a circadian clock: Period determination in the suprachiasmatic nuclei. *Cell*, 91(6):855–860, December 1997.

[61] X.-J. Wang. Neurophysiological and computational principles of cortical rhythms in cognition. *Physiol. Rev.*, 90(3):1195–1268, July 2010.

[62] T. Womelsdorf, P. Fries, P.P. Mitra, and R. Desimone. Gamma-band synchronization in visual cortex predicts speed of change detection. *Nature*, 439:733, Dec 2006.

[63] C. Börgers and N.J. Kopell. Gamma oscillations and stimulus selection. *Neural Comput*, 20(2):383–414, Feb 2008.

[64] G. G. Gregoriou, S. J. Gotts, H. H. Zhou, and R. Desimone. High-frequency, long-range coupling between prefrontal and visual cortex during attention. *Science*, 324(5931):1207–1210, May 2009.

[65] Conrado A Bosman, Jan-Mathijs Schoffelen, Nicolas Brunet, Robert Oostenveld, Andre M Bastos, Thilo Womelsdorf, Birthe Rubehn, Thomas Stieglitz, Peter De Weerd, and Pascal Fries. Attentional stimulus selection through selective synchronization between monkey visual areas. *Neuron*, 75:875–888, Sep 2012.

[66] M. J. Roberts, E. Lowet, N. M. Brunet, M. Ter Wal, P. Tiesinga, P. Fries, and P. De Weerd. Robust gamma coherence between macaque V1 and V2 by dynamic frequency matching. *Neuron*, 78(3):523–536, May 2013.

[67] N. Brunel and V. Hakim. Fast global oscillations in networks of integrate-and-fire neurons with low firing rates. *Neural Comput.*, 11(7):1621–1671, October 1999.

[68] M. A. Whittington, R. D. Traub, N. Kopell, B. Ermentrout, and E. H. Buhl. Inhibition-based rhythms: experimental and mathematical observations on network dynamics. *Int. J. Psychophysiol.*, 38:315, 2000.

[69] N. Brunel and X. J. Wang. What determines the frequency of fast network oscillations with irregular neural discharges? I. Synaptic dynamics and excitation-inhibition balance. *J. Neurophysiol.*, 90(1):415–430, July 2003.

[70] C. Börgers and N. Kopell. Synchronization in networks of excitatory and inhibitory neurons with sparse, random connectivity. *Neural Comput.*, 15(3):509–538, March 2003.

[71] Paul Tiesinga and Terrence J. Sejnowski. Cortical enlightenment: Are attentional gamma oscillations driven by ING or PING? *Neuron*, 63(6):727–732, September 2009.

[72] György Buzsaki and Xiao-Jing Wang. Mechanisms of gamma oscillations. *Annual Review of Neuroscience, Vol 35*, 35:203–225, 2012.

[73] B Blasius, A Huppert, and L Stone. Complex dynamics and phase synchronization in spatially extended ecological systems. *Nature*, 399:354–359, May 1999.

[74] E. Ravasz, A. L. Somera, D. A. Mongru, Z. N. Oltvai, and A. L. Barabasi. Hierarchical organization of modularity in metabolic networks. *Science*, 297(5586):1551–1555, August 2002.

[75] E. T. Bullmore and O. Sporns. Complex brain networks: graph theoretical analysis of structural and functional systems. *Nature Reviews Neuroscience*, 10(3):186–198, March 2009.

[76] K. Park, Y.C. Lai, S. Gupte, and J.W. Kim. Synchronization in complex networks with a modular structure. *Chaos*, 16(1):015105, Mar 2006.

[77] F. Sorrentino and E. Ott. Network synchronization of groups. *Physical Review E*, 76(5):056114, November 2007.

[78] E. Oh, K. Rho, H. Hong, and B. Kahng. Modular synchronization in complex networks. *Physical Review E*, 72(4):047101, October 2005.

[79] A. Arenas, A. Diaz-Guilera, J. Kurths, Y. Moreno, and C. S. Zhou. Synchronization in complex networks. *Physics Reports-review Section of Physics Letters*, 469(3):93–153, December 2008.

[80] S. G. Guan, X. G. Wang, Y. C. Lai, and C. H. Lai. Transition to global synchronization in clustered networks. *Physical Review E*, 77(4):046211, April

2008.

[81] Y. Kawamura, H. Nakao, K. Arai, H. Kori, and Y. Kuramoto. Phase synchronization between collective rhythms of globally coupled oscillator groups: Noisy identical case. *Chaos*, 20(4):043109, December 2010.

[82] K. R. Neville and L. B. Haberly. Beta and gamma oscillations in the olfactory system of the urethane-anesthetized rat. *J. Neurophysiol.*, 90(6):3921–3930, December 2003.

[83] Leslie M. Kay and Philip Lazzara. How global are olfactory bulb oscillations? *Journal of Neurophysiology*, 104(3):1768–1773, Sep 2010.

[84] S.-F. Chow, S. D. Wick, and H. Riecke. Neurogenesis drives stimulus decorrelation in a model of the olfactory bulb. *PLoS Comp. Biol.*, 8:e1002398, 2012.

[85] W. Adams, J. N. Graham, X. Han, and H. Riecke. Top-down inputs drive neuronal network rewiring and context-enhanced sensory processing in olfaction. *PLoS Computational Biology*, 15:e1006611, January 2019.

[86] A.S. Pikovsky. Synchronization and stochastization of nonlinear oscillators by external noise. In R.Z. Sagdeev, editor, *Nonlinear and Turbulent Processes in Physics*, page 1601. Harwood Academic, Singapore, 1984.

[87] C. S. Zhou and J. Kurths. Noise-induced phase synchronization and synchronization transitions in chaotic oscillators. *Physical Review Letters*, 88(23):230602, June 2002.

[88] J. Teramae and D. Tanaka. Robustness of the noise-induced phase synchronization in a general class of limit cycle oscillators. *Physical Review Letters*, 93(20):204103, November 2004.

[89] A. F. Mainen and T. J. Sejnoswki. Reliability of spike timing in neocortical neurons. *Science*, 268:1503, 1995.

[90] E. Shea-Brown, K. Josic, De La Rocha J., and B. Doiron. Correlation and synchrony transfer in integrate-and-fire neurons: Basic properties and consequences for coding. *Phys. Rev. Lett.*, 100(10):108102, March 2008.

[91] Aushra Abouzeid and Bard Ermentrout. Correlation transfer in stochastically driven neural oscillators over long and short time scales. *Phys Rev E Stat Nonlin Soft Matter Phys*, 84(6 Pt 1):061914, Dec 2011.

[92] M B Miller and B L Bassler. Quorum sensing in bacteria. *Annual Review of Microbiology*, 55:165–199, 2001.

[93] David McMillen, Nancy Kopell, Jeff Hasty, and J J Collins. Synchronizing genetic relaxation oscillators by intercell signaling. *Proceedings of the National Academy of Sciences of the United States of America*, 99:679–684, January 2002.

[94] J. Garcia-Ojalvo, M. B. Elowitz, and S. H. Strogatz. Modeling a synthetic multicellular clock: Repressilators coupled by quorum sensing. *Proceedings of the National Academy of Sciences of the United States of America*, 101(30):10955–10960, July 2004.

[95] S.H. Strogatz. *Nonlinear Dynamics and Chaos*. Westview Press, 2015.

[96] K. Tsumoto, H. Kitajima, T. Yoshinaga, K. Aihara, and H. Kawakami. Bifurcations in Morris-Lecar neuron model. *Neurocomputing*, 69(4-6):293–316, January 2006.

[97] P. H. Tiesinga and J. V. Jose. Robust gamma oscillations in networks of inhibitory hippocampal interneurons. *Network-Computation in Neural Systems*, 11(1):1–23, 2000.

[98] I. Vida, M. Bartos, and P. Jonas. Shunting inhibition improves robustness of gamma oscillations in hippocampal interneuron networks by homogenizing firing rates. *Neuron*, 49(1):107–117, January 2006.

[99] M. A. Whittington, M. O. Cunningham, F. E. N. LeBeau, C. Racca, and R. D. Traub. Multiple origins of the cortical gamma rhythm. *Developmental Neurobiology*, 71(1):92–106, January 2011.

[100] B. Ermentrout. Type I membranes, phase resetting curves, and synchrony. *Neural Comput.*, 8(5):979, July 1996.

[101] Christoph Börgers, Martin Krupa, and Stan Gielen. The response of a classical Hodgkin-Huxley neuron to an inhibitory input pulse. *J. Comput. Neurosci.*, 28(3):509–526, June 2010.

[102] B. Ermentrout. Complex dynamics in winner-take-all neural nets with slow inhibition. *Neural Netw.*, 5(3):415–431, August 1992.

[103] Xize Xu, John Hongyu Meng, and Hermann Riecke. Enhancing the synchronization of coupled gamma rhythms through intrinsic network heterogeneity. In *Society for Neuroscience Conference 2019*, 465.21, 2019.

[104] B. Ermentrout. An adaptive model for synchrony in the firefly pteroptyx-malaccae. *Journal of Mathematical Biology*, 29(6):571–585, 1991.

[105] A. Goldbeter, C. Gérard, D. Gonze, J-C. Leloup, and G. Dupont. Systems biology of cellular rhythms. *FEBS Lett*, 586(18):2955–2965, Aug 2012.

[106] J J Tyson, C I Hong, C D Thron, and B Novak. A simple model of circadian rhythms based on dimerization and proteolysis of per and tim. *Biophysical journal*, 77:2411–2417, November 1999.

[107] S. An, R. Harang, K. Meeker, D. Granados-Fuentes, C. A. Tsai, C. Mazuski, J. Kim, F. J. Doyle, L. R. Petzold, and E. D. Herzog. A neuropeptide speeds circadian entrainment by reducing intercellular synchrony. *Proceedings of the National Academy of Sciences of the United States of America*, 110(46):E4355–E4361, November 2013.

[108] M Amdaoud, M Vallade, C Weiss-Schaber, and I Mihalcescu. Cyanobacterial clock, a stable phase oscillator with negligible intercellular coupling. *Proceedings of the National Academy of Sciences of the United States of America*, 104:7051–7056, April 2007.

[109] Gopal Pattanayak and Michael J Rust. The cyanobacterial clock and metabolism. *Current Opinion in Microbiology*, 18:90–95, April 2014.

[110] Hiroshi Ito, Hakuto Kageyama, Michinori Mutsuda, Masato Nakajima, Tokitaka Oyama, and Takao Kondo. Autonomous synchronization of the circadian KaiC phosphorylation rhythm. *Nature Structural & Molecular Biology*, 14:1084–1088, November 2007.

[111] Simbarashe Nkomo, Mark R Tinsley, and Kenneth Showalter. Chimera and chimera-like states in populations of nonlocally coupled homogeneous and heterogeneous chemical oscillators. *Chaos (Woodbury, N.Y.)*, 26:094826, September 2016.

[112] Daniel M. Abrams, Rennie Mirollo, Steven H. Strogatz, and Daniel A. Wiley. Solvable model for chimera states of coupled oscillators. *Physical Review Letters*, 101(8):084103–084103, August 2008.